UNIVERSITY OF CALIFORNIA SAN DIEGO

Transport Phenomena in Lipid Bilayers

A dissertation submitted in partial satisfaction of the
requirements for the degree
Doctor of Philosophy

in

Engineering Sciences (Mechanical Engineering)

by

Arijit Mahapatra

Committee in charge:

Professor Padmini Rangamani, Co-Chair
Professor David Saintillan, Co-Chair
Professor James Friend
Professor Michael Holst
Professor Stefan Llewellyn Smith

2022

The dissertation of Arijit Mahapatra is approved, and it is acceptable in quality and form for publication on microfilm and electronically.

University of California San Diego

2022

DEDICATION

To my wife Shrabana

EPIGRAPH

The true laboratory is the mind, where

behind illusions we uncover the laws of truth.

— Jagadish Chandra Bose

TABLE OF CONTENTS

LIST OF FIGURES

LIST OF TABLES

ACKNOWLEDGEMENTS

First, I would like to thank my co-advisors, Prof. Padmini Rangamani and Prof. David Saintillan, for the entire journey over the last five years to reshape myself from an impatient engineer to a patient scientist. They have continuously motivated me throughout my Ph.D. term with their scientific brilliance and diligence. They have taught me how to ask critical questions in biophysics and seek the answer, not getting caught up in the details of mathematics and numerics. Further, they also made sure I had enough challenges in the learning path of my career by providing opportunities for projects beyond my comfort zone. It has been an incredible journey in my scientific and research path; I owe my biophysics and biological fluid mechanics knowledge to them. I am thankful for my current and past labmates in both Rangamani Lab and Saintillan Research group: Morgan, Haleh, Miriam, Justin, Achal, Akhil, Jennifer, Ritvik, Michael, Allen, Aravind, Hossein, Tanumoy, Dheeraj, Yuzhu, and Sage from whom I have been learning many fundamental aspects of biophysics, have always been the first go-to person for exercising the critical thinking. I want to convey my special thanks to Miriam, Cuncheng, and Jennifer for their help proofreading my writing for the dissertation and all the published papers and for providing critical feedback.

I want to thank my committee members: Prof James Friend for the help, support, and comments regarding the experimental perspective, Prof. Stefan Llewellyn Smith for his critical comments on my research and proofreads of every chapter of my dissertation, Prof. Michael Holst for his suggestions, and comments on the numerical methods. I am also thankful to Prof. Llewellyn Smith and Prof. William Young for the fascinating lectures on Applied mathematics, which made the founding base of the dissertation.

I would like to thank all my teachers who inspired me in my scientific thinking starting from high school. I sincerely thank Saibal babu and Matriprashad babu for their immense belief in me and continuous encouragement through their teaching of Mathematics and Physics. I thank all my professors in IIEST Shibpur and IIT Kanpur, especially prof. Debashis Pal and Prof. Malay

K. Das, for whom I developed an enormous interest in fluid mechanics. I owe my knowledge of the mechanics of materials and dynamics to Prof. Debasis Datta and my undergrad thesis advisor Prof. Sisir Kumar Guha, who also helped me with the basic research strategies of formulating a problem scientifically. Also, I acknowledge the significant role of my master's thesis advisor Prof. Parthasarathi Ghoshdastidar for teaching me fundamental methodologies to perform scientific research.

I am also thankful for the opportunity to work on real-life engineering problems during two years of my industrial tenure. The term shaped my engineering thought process of problem-solving, and I learned many fundamental aspects of applied science and engineering, which complemented my engineering studies. For example, I came across the multiscale fluid mechanics and heat transfer which assisted me in unraveling many problems in my Ph.D. projects. Most importantly, I met a fabulous group of colleagues who became my most substantial support during my Ph.D., specifically, Tanul, Anupriya, Juile, Supriya, Rucha, Arindam, Aniket, Siddhant, Nikhil, Priyajeet, and Sahil. I am grateful to them for their unconditional support.

I cherish the beautiful friendship I had since my college days in Shibpur and Kanpur, which gave me much-needed energy and motivation to go through 5 years of intense training. Saurabh da and Avishek da have been my role models in choosing my research career; I am also thankful for their continuous inspiration and monthly dozes of encouragement. I am honored to have my undergrad friends: Anubrata, Gourab, Pradipta, Arnab, Avik, Ritwik, Avijit, and Monsur; they have been integral to my thesis and the journey. In addition, the discussion on the broader topics beyond Science and Engineering had played a pivotal role in the critical thinking that helped me find clarity in my work and analytical mindset. My San Diego friends, especially Sheel, Akhil, Soumya, and Avik, deserve a lot of credit for making this journey happen. It would have been absolutely impossible without their support, especially during the last half of my Ph.D. time throughout the Pandemic. I also acknowledge the Friday Dinner at 9226 Regents road and the fantastic people: Brato, Ahanjit, Sumit, Sridip, Shouvik, and Abhik da, who warmly welcomed

me to San Diego.

I am grateful for the love and support of my family throughout my academic life. Moreover, I want to thank my girlfriend Shrabana (now my wife), to whom I want to dedicate my dissertation, for her tremendous support and encouragement to join the Ph.D. program and to continue every day through ups and downs. My Ph.D. is her journey, too, as much as mine. I am also immensely thankful to my parents, sister, and thakuma (grandma). Their patience and affection helped me stay grounded and sane during the elevated anxious time.

Chapter 1 is primarily based on and inspired by the section from the published papers appeared in the Journal of Fluid Mechanics (2020) authored by Arijit Mahapatra, David Saintillan, and Padmini Rangamani and a published paper in Soft matter (2021) authored by Arijit Mahapatra, David Saintillan, and Padmini Rangamani. The dissertation author was the primary author of both papers.

Chapter 2 is primarily based on the sections from the published papers appeared in the Journal of Membrane Biology (2021) authored by Arijit Mahapatra, Can Uysalel, and Padmini Rangamani, a published paper in The Journal of Fluid Mechanics (2020) authored by Arijit Mahapatra, David Saintillan, and Padmini Rangamani, and a published paper in Soft matter (2021) authored by Arijit Mahapatra, David Saintillan, and Padmini Rangamani. The dissertation author was one of the primary researchers in the paper published in the Journal of Membrane Biology and the primary author of the papers published in the Journal of Fluid Mechanics and Soft Matter.

Chapter 4 is primarily based on the published material appeared in the Journal of Fluid Mechanics (2020) authored by Arijit Mahapatra, David Saintillan, and Padmini Rangamani. The dissertation author was the primary author of the work.

Chapter 5 is primarily based the published material appeared in Soft Matter (2021) authored by Arijit Mahapatra, David Saintillan, and Padmini Rangamani. The dissertation author was the primary author of the work.

Chapter 6 is primarily based on the manuscript in preparation authored by Arijit Mahapatra and Padmini Rangamani. The dissertation author was the primary author of the work.

Chapter 7 is primarily based on the manuscript in preparation authored by Arijit Mahapatra and Padmini Rangamani. The dissertation author was the primary author of the work.

VITA

2013	B. E. in Mechanical Engineering, IIEST Shibpur (India)
2015	M. Tech. in Mechanical Engineering (Fluid and Thermal Sciences), IIT Kanpur (India)
2022	Ph. D. in Engineering Sciences (Mechanical Engineering), University of California San Diego

PUBLICATIONS

A. Mahapatra, D. Saintillan, and P. Rangamani, "Transport phenomena in fluid films with curvature elasticity", *J. Fluid. Mech.*, 905 (A8), 2020.

A. Mahapatra, C. Uysalel, and P. Rangamani, "Mechanics and thermodynamics of tubule formation in biological membranes", *J. Mem. Biol.*, 254(3), 2021.

A. Mahapatra, D. Saintillan, and P. Rangamani, "Curvature-driven feedback on aggregation-diffusion of proteins in lipid bilayers", *Soft Matter*, Aug, 2021.

A. Mahapatra and P. Rangamani, "Mechanics of protein-induced tubulation in lipid membranes is governed by a snap-through transition", *In Preparation*.

ABSTRACT OF THE DISSERTATION

Transport Phenomena in Lipid Bilayers

by

Arijit Mahapatra

Doctor of Philosophy in Engineering Sciences (Mechanical Engineering)

University of California San Diego, 2022

Professor Padmini Rangamani, Co-Chair
Professor David Saintillan, Co-Chair

Lipid bilayers are formed from the self-assembly of two layers of amphiphilic lipid molecules. They are excellent model systems for studying the behavior of cellular membranes. The mechanics of lipid bilayers fascinates physicists and engineers because of their in-plane flow and out-of-plane bending. In cellular membranes, lipid bilayers contain a heterogeneous composition of integral and peripheral proteins that perform specific biophysical processes. These proteins are known to generate curvature on the membrane, and they also sense the curvature. Additionally, proteins undergo diffusion and aggregation in the membrane. Experiments have shown that the in-plane viscous flow of lipid influences the dynamics of protein distribution

through advection. Therefore, the ability of the protein to deform the membrane, combined with the ability of the membrane curvature and flow to influence protein distribution, leads to a closed coupled problem. In the first part of the thesis, I present a comprehensive theory of the coupled problem of elastic bending of lipid bilayers, diffusion and aggregation of proteins, and in-plane viscous flow of lipids. The curvature generation of the proteins on the membranes is modeled with the help of a spontaneous curvature that emulates the asymmetry in the lipid leaflets. We formulate a Helfrich-like free energy of the membrane, which is modified to include the entropic contribution that leads to diffusion of the protein and the aggregation potential that mimics the forces of protein-protein interaction. The free energy is minimized to get the conservation equation of proteins and the equation of motion for the membrane shape. The mass conservation relation is further extended to account for the binding of proteins from the bulk volume. We perform a stability analysis to find the necessary condition to form an aggregate and compare our system with the Cahn-Hilliard-like formalism. We demonstrate the utility of the model by presenting numerical simulations in the limit of small deformation of the membrane and large deformation axisymmetric geometry. We rigorously investigate the effect of bending and curvature-induced feedback in protein distribution and related energy landscape.

In the second part of the thesis, we model the formation and the shape transition in the membrane tubes generated by aggregated domains BAR-proteins that induce anisotropic curvatures. BAR-proteins are 1-dimensional rod-like proteins that bend the membrane because of their intrinsic shape and binding orientation. We first formulate a continuum bending energy due to anisotropic spontaneous curvatures. Then we include the effect of orientation by the values of spontaneous curvatures. The resultant shape equations that minimize the free energy are solved numerically in an axisymmetric geometry. We observe that the membrane undergoes a snap-through transition of its shape from a tent to a tube, and the transition is observed for all parameters. We further analyze the nature of the transition and report a hysteresis-like behavior that is commonly observed across snap-through transitions in elastic structures.

Chapter 1

Introduction

This thesis presents problems of transport phenomena in deforming lipid bilayers in the presence of a myriad of proteins. Lipid bilayers are the fundamental components of biological membranes in cells, and intracellular organelles [2]. These membranes are extremely heterogeneous [3] in composition, consisting of many different types of lipids and transmembrane and peripheral proteins, and ion channels [4]. While the membrane-bound proteins carry out specific cellular functions [5], the lipid-protein interaction that attracted significant focus because of their emerging mechanics [6]. In many cases, the lipid-protein interaction results in out-of-plane deformation in the membrane, and this has been studied both theoretically and experimentally over the past five decades [7, 8, 9, 10, 11]. These curvature-generating phenomena [12] governs various shapes of membranes, including cylindrical tubulation [13], tubular unduloid [14], spherical vesicle [15], and membrane trafficking channel [16, 17]. Apart from curvature generation [12], this interaction leads to curvature-sensing behavior [18] of proteins in the membrane plane. Over the last five decades, curvature generation in the membrane has been theoretically modeled with internal parameters such as protein density, lipid tilt angle, the local composition of lipids and proteins [19], and interleaflet asymmetry [20]. In-plane transport of proteins due to diffusion [21] and advection caused by viscous flow of the lipids regulates the temporal dynamics of protein

distribution [22, 23]. Moreover, particle interactions among proteins [24] or interaction through membrane curvature [25] influences the protein distribution. Interactions between proteins can also lead to the formation of protein aggregates depending on the strength of interaction forces [26, 25]. Experimental observations in reconstituted or synthetic lipid vesicles show that the coupling of lipid flow, protein diffusion, and membrane bending can give rise to emergent phenomena [27, 28, 29]. These dynamics of cellular membranes are critical to cellular function, lipid rafts, and even in governing cell death [30]. Some theoretical models have explicitly studied the coupling between the density of curvature-inducing proteins and membrane bending [31, 32, 33] and the coupling between viscous flow and bending [34]. However, the coupling between flow, bending, diffusion, and aggregation has not been commonly considered, except in a few phase transition models [35].

Most of the protein-induced curvature generation model considers the spontaneous curvature in a Helfrich Hamiltonian [36], and demonstrate geometries with isotropic curvatures such as buds and dome. However, this study cannot explain geometries with non-equal principal curvatures, such as membrane tubes. Moreover, proteins like the BAR-domain that have intrinsic asymmetry due to their rod-like structure induce curvature deviators in the membrane plane. The formation of membrane tubes is crucial for biophysical processes such as the formation of t-tubules, mitochondria cristae, ER-Golgi complex, and drosophila cellularization. The shape transition in tubular structure in cell membranes govern physiological functions and have been the focus of theoretical and experimental studies. This transition is also observed in during the in-vitro experiments. For example, the di-differentiation of t-tubule in the cardiac myocyte is observed in a culture [37], and the changes in the shape of cristae in mitochondria [38] resembles such transitions. In both cases, the transition in shapes observed resembles the snap-through transition of elastic object [39, 40]. The modeling approaches taken lately with the extension of Helfrich Hamiltonian account for the anisotropic curvature [41]. Furthermore, the orientation of such anisotropic proteins played a crucial role in curvature generation and was studied in

detail through discrete protein models. The anisotropy in the induced-curvature by these proteins energetically favors a tubular structure [42]. However, there is a need for a comprehensive model for the demonstration of tubular protrusion and to understand the shape dynamics.

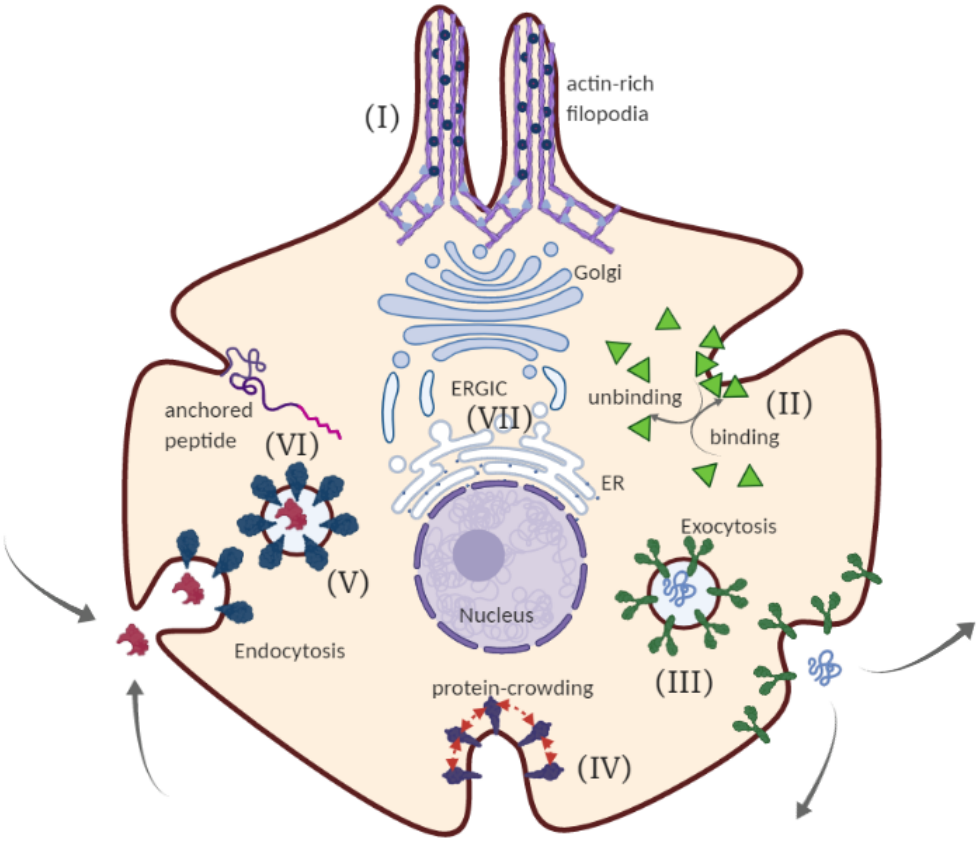

Figure 1.1: Selected mechanisms of membrane protein interactions. (I) Actin-driven filopodial protrusion, (II) binding and unbinding of curvature-inducing proteins to the membrane, (III) exocytosis of a vesicle to the membrane and followed by diffusion of proteins in the membrane, (IV) tubular shape transformation of the membrane due to steric effect of crowded proteins, (V) clustering of curvature inducing proteins at the endocytic pits and subsequent formation of endocytic vesicle, (VI) tubulation due to anchored motor protein or peptides, and (VII) tubular transport carrier (TC) during membrane trafficking in the ER-Golgi intermediate compartment (ERGIC).

1.1 Membrane-protein interaction and curvature generation

The integral and peripheral proteins in the plane of the membrane interact with lipids and the outcome leads to membrane bending that are crucial for many cellular functions (Figure 1.1). Membrane-protein interaction often generates curvature in the plane of the membrane through these three key mechanics, namely, hydrophobic helix insertion [43], membrane scaffolding [44], and curvature generation due to steric pressure of crowded domain of proteins [13]. Experiments on synthetic system provide insights into such mechanisms of curvature generation [4]. Curved membranes are broadly classified as spherical buds, cylindrical tubes, and pearled structured tubes [45, 46], and often the structure is associated with the localized density of proteins. Studies have reported the functional relationships between protein density, applied force, and the curvature generated [47, 48, 49, 50]. The curvature generation caused by localized proteins can be isotropic and anisotropic [45] in nature.

1.2 Elastic bending of the membrane

Lipid bilayers contain lipid molecules that organize orthogonal to the surface of the lipid membranes. The direction field and the cost of energy to tilt them emphasize the study of liquid crystal theory in this domain [51]. However, in the higher density of lipids and the lipid organizes fairly normal to the surface; and mechanics of lipid membranes can be understood from the surface deformation mechanics, considering the membrane as an elastic surface. The Canham-Helfrich [52, 53] type of model described such elastic behavior of the surface with the quadratic invariants of curvatures of the surface. This energy resembles the linear force-displacement relation, and the slope is depicted by the bending rigidity of the membrane, which is a material property of the lipid bilayers. Therefore, the elastic behavior of lipid membranes finds similarities with a thin elastic sheet [54, 55] except for its in-plane fluid property. The lipid membrane can deform due to external forces or due to intrinsic curvature generation by any membrane-bound proteins.

1.3 Protein dynamics in a deforming membrane

In the plane of the membrane, many of these proteins are known to diffuse [56], induce curvature in the bilayer [57], and aggregate either through protein-specific interactions [24] or due to membrane curvature [25]. Interactions between proteins can also lead to the formation of protein microdomains depending on the strength of interaction forces [26, 25]. The ability of these proteins to induce curvature, coupled with the ability of curvature to influence the lateral diffusion-aggregation dynamics, can result in a feedback loop between membrane curvature and protein density on the surface [58, 59, 60]. In addition to protein aggregation, in-plane viscous flow of the lipid molecules has been found to dominate some of the phase-transition kinetics of vesicle shapes [61].

1.4 Viscosity of the membrane

The elastic bending of the membrane has been studied predominantly with the help of the continuum model where the membrane is considered inviscid. In the past decade, many groups have proposed the addition of viscous effects in addition to membrane bending [62, 63, 64, 65] building on the ideas presented by [66]. More recently, it has been shown that the effect of intra-surface viscosity, in addition to membrane bending, allows for the calculation of local membrane tension in the presence of protein-induced spontaneous curvature [67] and for the analysis of flow fields on minimal surfaces [68]. Separately, the interaction between in-plane protein diffusion and membrane bending has been modeled [69, 70, 71, 72, 73, 15]. Specifically, [74] proposed a framework that included the chemical potential energy of membrane-protein interactions and membrane bending, and demonstrated the interaction between bending and diffusion. A series of studies by Arroyo and coworkers also developed a comprehensive framework for incorporating membrane-protein interactions using Onsager's variational principles [75, 65, 76]

1.5 Binding of proteins

Binding and unbinding of proteins from membranes are often associated with mechanical and chemical aspects of membrane biophysics. For example, scaffolding proteins like clathrin [77, 78] or BAR domain proteins [79, 80] bind to the membrane and induce curvature. However, the binding and unbinding of these proteins are often regulated by a chemical reaction controlled by several reaction kinetics [81]. The physical binding process is a complex phenomenon that depends on the shape of the particle, hydrophobic mismatch, local curvature, and excluded surface for binding [80]. However, a chemical potential-based approach can model the binding energy as a function of all the driving factors in a theoretical model [82, 83]. Binding or multiple species in a reaction-diffusion framework causes different instabilities, ranging from pattern formation, traveling and stationary waves to chemical turbulence [84, 85]. Additionally, the binding affinity is found to be curvature-dependent [86]. As a result, curvature-driven feedback can influence the energy landscape of binding and adhesion of proteins [83].

1.6 Transition of membrane shapes

The shape of the membrane due to curvature generation of proteins is governed by non-linear interaction of intrinsic curvature and elastic bending of the membrane. The nonlinearity leads to sudden transition of shapes in various cell biology applications such as cristae formation in mitochondria [38], t-tubule formation in myocytes [37], and transition from a hemispherical dome to a spherical bud during endocytosis [11] . Much of this transitions is regulated by a saddle-node bifurcation, and there are resemblances with the snap-through transition seen in the elastic structures. [39, 40] Snap-through instabilities mediated by forces are studied rigorously in elastic objects like beams, truss, and spherical caps [39].

1.7 Overview of the present work

Building on these efforts, we present a coupled theory for membrane mechanics that accounts for in-plane viscous flows and diffusion and aggregation of curvature-inducing transmembrane proteins in addition to membrane bending. We formulate a free energy functional that includes bending energy, the chemical potential energy of membrane-protein interactions, and protein binding. Chapter 2 presents the free energy and its individual components in detail. We obtain the governing equations of motion using a force balance, where the component of elastic stresses are obtained by minimizing the free energy and the viscous stress is estimated from the constitutive relation of flow on manifold. We derive the transport equation of proteins from the constitutive relation of protein flux with chemical potential. In Chapter 3, we described the methods of numerical simulation in detail for a few specific cases used in the subsequent chapters. In Chapter 4, we analyze the diffusion-driven system in the absence of protein aggregation for small deformations from the flat plane and large deformation of the membrane within the limit of axisymmetry. In Chapter 5, we include the effect of protein aggregation exclusively and analyze how the curvature-driven feedback can influence the dynamics of protein distribution for a small-deformation membrane. Chapter 6 analyze such a coupled system where curvature-inducing proteins undergo binding and unbinding from the cytoplasm in axisymmetric membranes under large deformation. All these chapters focus mainly on the dynamics of membrane deformation due to isotropic curvature-inducing proteins. However, in Chapter 7, we demonstrate the bending of the membrane to a tubular structure due to protein-induced anisotropic curvature and related transition in shape. We finish our thesis with concluding remarks and prospects suggestions for future work in Chapter 8.

1.8 Acknowledgement

This chapter is primarily based on and inspired by the section from the published papers appeared in the Journal of Fluid Mechanics (2020) authored by Arijit Mahapatra, David Saintillan, and Padmini Rangamani and a published paper in Soft matter (2021) authored by Arijit Mahapatra, David Saintillan, and Padmini Rangamani. The dissertation author was the primary author of both papers. I would like to thank my co-authors: Prof. Padmini Rangamani and Prof. David Saintillan.

Chapter 2

Mechanics and thermodynamics of biological membranes

2.1 Continuum modeling of mechanics and thermodynamics of membranes

Our system consists of the lipids that comprise the membrane and transmembrane proteins that are embedded in the plane of the membrane and are capable of inducing curvature. Our model includes the binding or unbinding of proteins from the bulk, but does not include the interactions of the bulk fluid with the membrane. The lipid bilayer is modeled as a thin elastic shell with negligible thickness that can bend out of the plane and is fluid in-plane. Importantly, we assume that the membrane is areally incompressible and this constraint is imposed on the membrane using a Lagrange multiplier. We describe the different energy contributions to the total energy of the system in detail below.

2.1.1 Bending of the membrane

Spontaneous curvature model

When a curvature-inducing protein binds to the membrane, the leaflets become non-symmetric. The seminal work of Helfrich [36], proposed the modeling of asymmetry in the membrane with the help of a spontaneous curvature. It is the preferred curvature of the membrane in a free condition, and the membrane offers minimum energy at that curvature. For an elastic membrane, the free energy will depend as a quadratic function of the curvature deviation from its spontaneous curvature. For protein-induced membrane curvature generation, there can be a functional relationship between the spontaneous curvature and density of the proteins [74]. Note that, the spontaneous curvature is generally predicted as a scalar, and generally refers to the isotropic curvature generation of the membrane.

Bending energy of the membrane

We model the curvature elastic free energy density of the membrane using the Helfrich Hamiltonian [36] given by

$$W_{bending} = \kappa[H - C(\sigma)]^2 + \bar{\kappa}K. \tag{2.1}$$

Here, H and K are mean and Gaussian curvatures of the membrane, κ and $\bar{\kappa}$ are the bending and Gaussian rigidities, and C is the spontaneous curvature induced by the proteins. The spontaneous curvature is assumed to depend linearly on protein density σ [87, 88] as

$$C(\sigma) = \ell\sigma, \tag{2.2}$$

where the proportionality constant, ℓ, has units of length.

Spontaneous deviatoric curvature and modified bending energy

When the curvature induction is anisotropic in nature, the spontaneous curvature models are unable to demonstrate the mechanics. BAR-domain proteins are one of those proteins that induces anisotropic curvature. These proteins are flexible rod-like curved proteins. When they bind to the membrane, they induce curvature in one direction. In such cases, the Helfrich free energy of elastic deformation are modified to include the effect of anisotropy [41] . The curvature difference between membrane and curvature-inducing proteins will govern the strain energy. Such curvature difference reads as

$$\boldsymbol{M} = \boldsymbol{R}C_{\mathrm{p}}\boldsymbol{R}^{-1} - \boldsymbol{b}, \tag{2.3}$$

where C_p is the curvature of the protein rod. b is the curvature tensor of the membrane, which is elaborate in detail in sec 2.2. $\boldsymbol{R}$ is the rotation tensor, which can be found as a function of the orientation angle θ, as shown in Figure 2.1, and reads as

$$\boldsymbol{R} = \begin{bmatrix} \cos\theta & -\sin\theta \\ \sin\theta & \cos\theta \end{bmatrix}. \tag{2.4}$$

The strain energy can be written as a summation of all the quadratic invarients of the curvature

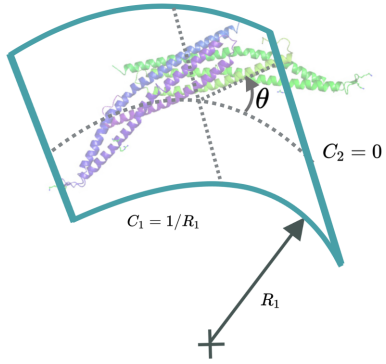

Figure 2.1: Orientation of BAR-domain proteins

difference tensor $\boldsymbol{M}$ as

$$W = \frac{K_1}{2}(\mathrm{Tr}\,\boldsymbol{M})^2 + K_2\,\mathrm{Det}\,\boldsymbol{M}. \tag{2.5}$$

This simplifies to

$$W = \kappa(H - C_0)^2 + \kappa_d\,(D - D_0)^2\,. \tag{2.6}$$

The first term describes the isotropic component of the strain energy, and the second term describes the anisotropic component. D_0 is the spontaneous anisotropic curvature, sometimes know as spontaneous deviatoric curvature. $D = \frac{C_1 - C_2}{2}$ is the curvature deviator of the membrane, where C_1 and C_2 are the principal curvatures of the membrane. κ and κ_d are the corresponding bending rigidities of the membrane.

2.1.2 Protein diffusion

The diffusion of proteins on the membrane surface is modeled using the principle of entropy maximization [89]. The entropy S of q proteins on n binding sites can be found from the number of combinations, $\Omega = {}^{n}C_q$, and is given by

$$S = k_B \log \Omega, \tag{2.7}$$

where k_B is the Boltzmann constant [90]. For sufficiently large values of q and n, the entropic component of the free energy per binding site can be represented as a function of area fraction $\phi = q/n$ as [89],

$$\frac{W_{entropy}}{n} = -\frac{TS}{n} = k_B T[\phi \log \phi + (1-\phi)\log(1-\phi)], \tag{2.8}$$

where T is the temperature of system. Note that the area fraction ϕ can also be represented as the ratio of the local protein density, σ, and the saturation density of proteins on the surface, σ_s. The free energy density per unit area of the membrane is obtained by multiplying the free energy

density per binding site ($W_{entropy}/n$) with the saturation density of the proteins (σ_s). Note that the entropic component of the free energy $W_{entropy}$ is minimized when the entropy S is maximum, which corresponds to a uniform distribution of proteins in the domain.

2.1.3 Viscous drag and effective diffusivity in the membrane

Diffusivity of a particle in is a highly viscous media can be found from the mobility of the particle motion. The diffusivity of a spherical particle in an unbounded fluid is given by Stokes-Einstein relation [91] as

$$D = \frac{k_B T}{f}, \tag{2.9}$$

where where D is the diffusivity, k_B is the Boltzmann constant, T is the temperature of the medium, and f is the hydrodynamic resistance, which is the inverse of mobility m of the particle and is given by

$$f = \frac{1}{m} = 6\pi\mu a. \tag{2.10}$$

Here μ is the viscosity of the fluid medium, and a is the radius of the sphere. For a particle suspending in an unbounded two-dimensional viscous media, the mobility tensor does not exist due to the Stokes paradox. However, in our case the membrane is surrounded by viscous cytoplasmic media. Saffman and Delbruk [92] shown that in such a case, the mobility exists and they provided a mathematical expression as

$$\frac{1}{f} = \frac{1}{4\pi\mu h}\left(\log\frac{\mu h}{\mu' a} - 0.5772\right). \tag{2.11}$$

Here h is the height of the membrane, μ and μ' are the viscosities of the membrane and surrounding fluid, and the 0.5772 is the Euler constant. The advantage of this approach is that the effect of bulk fluid drag is incorporated as a modified viscosity in 2-dimensional medium. Diffusion on the membrane can be studied without solving the hydrodynamics in bulk-fluid.

2.1.4 Protein aggregation

Aggregation of proteins can be modeled using the interaction enthalpy of particles in a binary system. With the help of mean-field theory, a continuum representation of the aggregation free energy per binding site can be derived as [89, 93, 94]

$$\frac{W_{aggregation}}{n} = \frac{\gamma}{2}\phi(1-\phi) + \frac{\gamma}{4\sigma_s}|\nabla\phi|^2, \tag{2.12}$$

where γ is the net effective interaction energy of the proteins. This term captures protein-protein attraction when $\gamma > 0$ and protein-protein repulsion when $\gamma < 0$.

2.1.5 Protein binding

The release of free energy associated with protein binding can be considered as a linear function of protein density. The free energy can be given by

$$E_{binding} = -\mu_b\sigma, \tag{2.13}$$

where μ_b represents the chemical potential for binding of the proteins from the cytoplasm. From a thermodynamics point of view, the binding of molecules from solvent without any chemical binding affinity can be estimated as [95]

$$\mu_b = \mu_0 + RT\log\frac{\sigma}{\sigma_{bulk}}. \tag{2.14}$$

For proteins with binding affinity Γ, the chemical potential of binding becomes as [96]

$$\mu_b = \mu^{mem} - \mu^{sol} = \mu_0^{surf} + RT\log\sigma + RT\log\Gamma - \mu_0^{sol} - RT\log c_{bulk}. \tag{2.15}$$

The binding affinity Γ can be estimated from the equilibrium reaction constant of binding K_{eq} as

$$\Gamma = \frac{\sigma_{bulk} K_{eq}}{\sigma}. \tag{2.16}$$

The chemical potential of binding can further be modified for the cases where proteins on the membrane oligomerize. In this study the chemical potential is estimated from the distribution of protein density that corresponds to energy minima for a spherical membrane. This method gives a binding energy as a function of membrane curvature.

2.1.6 Thermal fluctuation of membranes

The bending energy of lipid bilayers is not large compared to the Boltzmann energy ($k_B T$) at physiological temperatures. As a result, lipid bilayers undergo shape undulations due to the thermal movement of the fluid molecules in the surrounding domain. Experimental observations have reported membrane fluctuations in vesicles [97, 98, 99]; these undulations cause mechanical softening of the membrane [100] and can influence shape instabilities in the bilayer [101]. A series of theoretical studies [102, 103, 104] and Monte-Carlo simulations [105] have reported that thermal fluctuations soften the membrane a significant amount and also reduce local tension of the membrane. The effective bending rigidity in the presence of thermal fluctuations can be written as [103]

$$\kappa(T, \lambda, a) = \kappa_0 - \frac{3}{4\pi} k_B T \ln \frac{q_{\max}}{q_{\min}}, \tag{2.17}$$

and the effective tension is given by [103, 106]

$$\sigma(T, a) \simeq -\frac{3 k_B T}{8} (q_{\max}^2 - q_{\min}^2), \tag{2.18}$$

where κ_0 is the bending rigidity of the membrane in the absence of fluctuation, q_{min} and q_{max} are the magnitude of maximum and minimum wave numbers of the undulations respectively, λ

is the wavelength of the undulation, and a is the diameter of lipid molecules. The equipartition of energy limits the energy of each undulation mode. Thus, the magnitude of the deflection correlates inversely with the square of the wavenumber of that particular mode of undulation. Further, the ratio of these wavenumbers correlates with the maximum and minimum size of the wavelengths (λ) of the undulations as

$$\frac{q_{\max}}{q_{\min}} = \frac{\lambda_{\min}}{\lambda_{\max}}. \tag{2.19}$$

The highest value of the wavelength ($\lambda_{\max}$) is of the order of the length of the membrane (L), whereas the least value of it scales with the diameter of the lipid molecules (a).

Considering Equation 2.17 and the fact that thermal softening is directly correlated with the size of the domain, the role of fluctuations can become prominent on a larger length scale. In contrast, for a smaller length scale, the effect of thermal fluctuation will be negligible. The persistent length ξ below which the membrane behaves as a rigid surface depends on [104, 107]

$$\xi \propto \left(\frac{4\pi\kappa_0}{3T}\right). \tag{2.20}$$

2.1.7 Equilibrium description of the free energy

We obtain the total free energy density of the membrane, in terms of protein area fraction ϕ, by combining Equations (2.1), (2.8) and (2.12) as

$$W = \underbrace{k_B T \sigma_s \left[\phi \log \phi + (1-\phi)\log(1-\phi)\right]}_{\text{entropic}} + \underbrace{\frac{\gamma\sigma_s}{2}\phi(1-\phi) + \frac{\gamma}{4}|\nabla\phi|^2}_{\text{aggregation}} + \underbrace{\kappa(H-\ell\sigma)^2 + \bar{\kappa}K}_{\text{bending}}. \tag{2.21}$$

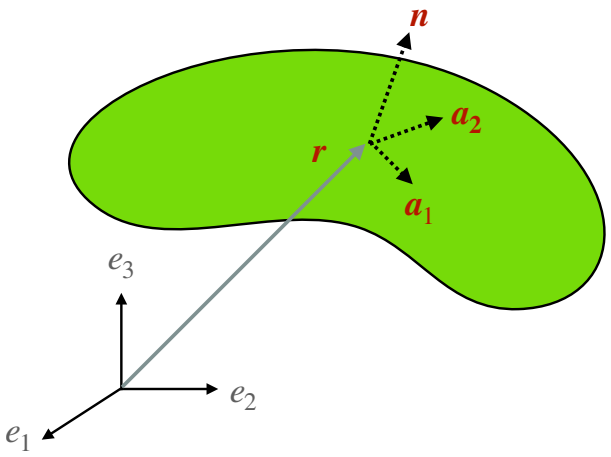

Figure 2.2: Membrane parameterization

2.2 Membrane geometry, kinematics and incompressibility

The lipid membrane is idealized as a two-dimensional manifold Ω in three-dimensional space. Material points on Ω are parametrized by a position field $\boldsymbol{r}(\theta^\alpha, t)$, where θ^α are surface coordinates and play a role analogous to that of a fixed coordinate system used to parametrize a control volume in the Eulerian description of classical fluid mechanics. Here and henceforth, Greek indices range over $\{1,2\}$ and, if repeated, are summed over that range. The local tangent basis on the surface is naturally obtained as $\boldsymbol{a}_\alpha = \boldsymbol{r}_{,\alpha}$ where commas identify partial derivatives with respect to θ^α. The unit normal field is then given by $\boldsymbol{n} = \boldsymbol{a}_1 \times \boldsymbol{a}_2 / |\boldsymbol{a}_1 \times \boldsymbol{a}_2|$. The tangent basis also defines the surface metric $a_{\alpha\beta} = \boldsymbol{a}_\alpha \cdot \boldsymbol{a}_\beta$ (or coefficients of the first fundamental form), a positive definite matrix, which is one of the two basic variables in surface theory. The other is the curvature $b_{\alpha\beta}$ (or coefficients of the second fundamental form) defined as $b_{\alpha\beta} = \boldsymbol{n} \cdot \boldsymbol{r}_{,\alpha\beta}$. Of special interest are the mean and Gaussian curvatures, which will enter the Helfrich energy of the membrane and are defined, respectively, as

$$H = \frac{1}{2} a^{\alpha\beta} b_{\alpha\beta}, \quad K = \frac{1}{2} \varepsilon^{\alpha\beta} \varepsilon^{\mu\eta} b_{\alpha\mu} b_{\beta\eta}\,. \tag{2.22}$$

Here, $a^{\alpha\beta} = (a_{\alpha\beta})^{-1}$ is the dual metric, and $\varepsilon^{\alpha\beta}$ is the permutation tensor defined as $\varepsilon^{12} = -\varepsilon^{21} = 1/\sqrt{a}$, $\varepsilon^{11} = \varepsilon^{22} = 0$.

We assume that the surface Ω is moving with time, and the velocity of a material point in the membrane is given by $\boldsymbol{u}(\theta^{\alpha}, t) = \dot{\boldsymbol{r}} = \partial r/\partial t$. It can be expressed in components on the natural basis introduced above:

$$\boldsymbol{u} = v^{\alpha}\boldsymbol{a}_{\alpha} + w\boldsymbol{n}, \tag{2.23}$$

where the components v^{α} capture the tangential lipid flow and w is the normal surface velocity. The membrane is assumed to be incompressible, which prescribes a relationship between the in-plane velocity field and the curvature as [62, 64]

$$v^{\alpha}_{;\alpha} = 2Hw, \tag{2.24}$$

where the semi-colon refers to covariant differentiation with respect to the metric $a_{\alpha\beta}$.

2.3 Governing differential equation

2.3.1 Force balance and equations of motion

The lipid bilayer is modeled as a two-dimensional surface, ω, in a three-dimensional space (Figure 7.1b). We refer the reader to [108, 109, 88] for details of the derivation and briefly summarize the key steps here. The surface is parametrized by a position vector $\boldsymbol{r}(\theta^{\alpha}, t)$, where θ^{α} are the surface coordinates, $\alpha \in \{1, 2\}$. In what follows, $(\cdot)_{,\alpha}$ refers to the partial derivative of the quantity in parenthesis with respect to θ^{α} and $(\cdot)_{;\alpha}$ refers to the covariant derivative [110]. The tangent basis vectors are given by $\boldsymbol{a}_{\alpha} = \boldsymbol{r}_{,\alpha}$. The unit surface normal $\boldsymbol{n}$ is given by $\boldsymbol{n} = (\boldsymbol{a}_1 \times \boldsymbol{a}_2)/|\boldsymbol{a}_1 \times \boldsymbol{a}_2|$. The metric tensor is given by $a_{\alpha\beta} = \boldsymbol{a}_{\alpha} \cdot \boldsymbol{a}_{\beta}$ and the curvature tensor is defined as $b_{\alpha\beta} = \boldsymbol{n} \cdot \boldsymbol{a}_{\alpha,\beta}$. $a^{\alpha\beta}$ is the dual metric and the inverse of $a_{\alpha\beta}$. $b^{\alpha\beta}$ is defined as $a^{\alpha\delta}a^{\mu\beta}b_{\delta\mu}$.

The equations of motions are obtained from a local stress balance on the interface, which

can be compactly stated as

$$\boldsymbol{\Sigma}^{\alpha}_{;\alpha} + p\boldsymbol{n} = \boldsymbol{0}, \tag{2.25}$$

where $\boldsymbol{\Sigma}$ is the stress tensor and $\boldsymbol{\Sigma}^{\alpha}_{;\alpha}$ is the divergence of stress. The stress vectors $\boldsymbol{\Sigma}^{\alpha}$ can be written in terms of their tangential and normal components as

$$\boldsymbol{\Sigma}^{\alpha} = N^{\beta\alpha}\boldsymbol{a}_{\beta} + S^{\alpha}\boldsymbol{n}. \tag{2.26}$$

As a result, the local equilibrium of forces, in the tangential and normal directions, is given by [108]

$$N^{\beta\alpha}_{;\alpha} - S^{\alpha}b^{\beta}_{\alpha} = 0, \tag{2.27}$$

$$S^{\alpha}_{;\alpha} + N^{\beta a}b_{\beta\alpha} + p = 0, \tag{2.28}$$

with

$$N^{\beta\alpha} = \zeta^{\beta\alpha} + \pi^{\beta\alpha} + b^{\beta}_{\mu}M^{\mu\alpha} \quad \text{and} \quad S^{\alpha} = -M^{\alpha\beta}_{;\beta}. \tag{2.29}$$

Here, p is the normal pressure acting on the surface, $\zeta^{\beta\alpha}$ and $M^{\alpha\beta}$ are the elastic stress and moment tensors, and $\pi^{\beta\alpha}$ is the viscous stress tensor. The elastic contribution of the surface stress and the moment tensor are derived from a free energy and are expressed as [55]

$$\zeta^{\beta\alpha} = \rho\left(\frac{\partial F}{\partial a_{\alpha\beta}} + \frac{\partial F}{\partial a_{\beta\alpha}}\right), \qquad M^{\alpha\beta} = \frac{\rho}{2}\left(\frac{\partial F}{\partial b_{\alpha\beta}} + \frac{\partial F}{\partial b_{\beta\alpha}}\right). \tag{2.30}$$

Here, F is the energy Lagrangian per unit mass defined as [55]

$$F(H,K,\rho) = \bar{F}(H,K) - \xi/\rho, \tag{2.31}$$

where ξ is a Lagrange multiplier imposing the constraint of incompressibility, and ρ is the

membrane density which is assumed to be constant. It is customary to formulate the mechanics in terms of the free energy per unit area [111]

$$W = \rho \bar{F}. \tag{2.32}$$

The incompressibility constraint on the surface results the continuity equation [108] as given by Section 3.4.2. %endequation The viscous stresses obey the constitutive relation [109]

$$\pi^{\alpha\beta} = 2\nu \left[a^{\alpha\mu} a^{\beta\eta} d_{\mu\eta} - w b^{\alpha\beta} \right]. \tag{2.33}$$

Here, $d_{\mu\eta} = \left(v_{\mu;\eta} + v_{\eta;\mu} \right)/2$ is the rate-of-strain tensor expressed in terms of the covariant velocity field $v_\mu = a_{\alpha\mu} v^\alpha$, and w is the normal surface velocity (see [109, 112, 88] for details).

2.3.2 Conservation principle and transport equations

Conservation of mass for the protein density σ is given by

$$\frac{\partial \sigma}{\partial t} + m^{\alpha}_{;\alpha} = q, \tag{2.34}$$

where the flux is

$$m^\alpha = \left(v^\alpha \sigma - \frac{1}{f} \phi a^{\alpha\beta} \mu_{,\beta} \right). \tag{2.35}$$

This flux has contributions from advection due to the in-plane velocity field $\boldsymbol{v}$ and from gradients in the protein chemical potential μ. The constant f denotes the thermodynamic drag coefficient of a protein and is related to its diffusivity D by the Stokes-Einstein relation: $D = k_B T/f$. q denotes the net rate of protein addition to the membrane from the bulk, which might occur from binding-unbinding or exo-endosytosis of proteins. The chemical potential, μ, is obtained as the

variational derivative

$$\mu = \frac{\delta F}{\delta \phi}, \tag{2.36}$$

where F is the total energy of the system of area A:

$$F = \int_{\omega} W(\phi, \phi_{,\alpha})\, dA. \tag{2.37}$$

Note that the energy density is a function of both the protein area fraction ϕ and its gradient $\phi_{,\alpha}$. Using the definition of the variational derivative, we get the expression of the chemical potential as:

$$\mu = \frac{\delta F}{\delta \phi} = \frac{\partial W}{\partial \phi} - \frac{\partial}{\partial \theta^{\alpha}} \cdot \frac{\partial W}{\partial \phi_{,\alpha}}. \tag{2.38}$$

Using Equation (2.21) for W, this yields

$$\mu = k_B T \sigma_s [\log \phi - \log(1-\phi)] - 2\kappa \ell \sigma_s (H - \ell \sigma_s \phi) - \frac{\gamma \sigma_s}{2}(2\phi - 1) - \frac{\gamma}{2} a^{\alpha\beta} \phi_{,\alpha} \phi_{,\beta}. \tag{2.39}$$

q in Equation (2.34) denotes the net rate of protein addition to the membrane from the bulk, which might occur from binding-unbinding or exo-endosytosis of proteins. Using Equation (2.39) in Equation (2.34) will result in the evolution equation for σ.

2.4 Instabilities in shape and protein transport

The shape of the membrane and the distribution of the protein in the membrane plane undergo instability, which is associated with the localization of proteins in membranes and local deformation. Such instabilities in the protein transport arise depending on the interaction forces among the proteins, where curvature-induced feedback plays a crucial role. We analyze such instabilities with the help of linear stability analysis, where we consider a linearized set of governing equations of the perturbation quantities from their homogeneous steady-state

condition. We consider normal mode for the perturbation variable ζ with the growth rate of α and wavenumber k as given by

$$\zeta = \hat{\zeta} e^{\alpha t + i 2\pi \boldsymbol{k}\cdot\boldsymbol{x}}. \tag{2.40}$$

This gives a dispersion relation for marginal stability of the system, which dictates the specific mode that can become unstable in the parameter regime. Note that the coupled systems of the linearized equations include the effect of shape on the instability of protein distribution and vice versa. The instability differs from diffusion-driven instability, which happens during a multi-component reaction-diffusion system that governs Turing patterns. Instead, the competition between aggregation and diffusion governs the dynamics of protein aggregation. Additionally, the binding and unbinding of proteins to the membrane from the cytoplasm may lead to an unstable spatial distribution of proteins leading to the formation of localized patches. On the other hand, the nonlinearity involved in the shape of the membrane causes numerous instabilities in the dynamics of the shape, such as neck formation in a spherical bud during endocytosis and the transition from a tent-like shape to a long tube. Such instabilities and resultant bifurcation resemble to the dynamics of the elastic bodies. Mathematical stability analysis becomes very complex due to its nonlinear base state; therefore, numerical approaches are considered to investigate such instabilities.

2.5 Numerical simulation

We solved the dimensionless governing equations of the equation of motion and the mass conservation of proteins in the linear Monge regime numerically inside a square domain and for axisymmetric geometry for large deformation. We have considered the no-flux boundary for proteins and clamped boundary for the membrane deformation in Chapter 4 and Chapter 6. However, we adopted periodic boundary conditions for both proteins and membrane deformation for Chapter 5 to study protein aggregation. Chapter 7 solved an equilibrium problem in

axisymmetric geometry, and we used clamped boundary conditions for deformation. Numerical simulations were performed on a spatially uniform grid in the Monge regime, and nonuniform grids are considered for axisymmetric geometry with a denser grid towards the center. We used a finite difference scheme to solve the transport equation for the protein density, membrane shape, and velocity for Chapter 4, Chapter 6 for the no-flux boundary for proteins, and clamped boundary for membrane shape. The velocity and the shape equation subjected to the periodic boundary in Chapter 5 were solved using a Fourier spectral method [113, 114]. In all cases, a semi-implicit scheme was used for the time marching for the protein density ϕ with a time step Δt, where the nonlinear terms involving velocity and curvature were treated explicitly. In contrast, the nonlinear aggregation-diffusion terms were treated with linear implicit terms. The iterations were performed within a time step until convergence was achieved. For the convergence within a time step, we used a tolerance limit to check the convergence. The equilibrium shape equation in Chapter 7 of membrane is solved with the help of the finite difference based solver bvp4c in MATLAB. The methods of numerical simulations are described in Chapter 3 in detail.

2.6 Acknowledgements

I would like to acknowledge my co-authors: Prof. David Saintillan, Prof. Padmini Rangamani, and Mr. Can Uysalel. This chapter is primarily based on the sections from the published papers appeared in the Journal of Membrane Biology (2021) authored by Arijit Mahapatra, Can Uysalel, and Padmini Rangamani, a published paper in The Journal of Fluid Mechanics (2020) authored by Arijit Mahapatra, David Saintillan, and Padmini Rangamani, and a published paper in Soft matter (2021) authored by Arijit Mahapatra, David Saintillan, and Padmini Rangamani. The dissertation author was one of the primary researchers in the paper published in the Journal of Membrane Biology and the primary author of the papers published in the Journal of Fluid Mechanics and Soft Matter.

Chapter 3

Numerical simulation

3.1 Introduction

In this section, we will discuss the numerical schemes adopted to solve the governing equations. The system of equations is solved for two idealized geometries: a square Monge patch with small deformation of the membrane from its projected plane and axisymmetric geometries with large deformations. For the Monge patch, the governing equations are parameterized with respect to their cartesian coordinates (x, y) in the projected plane. However, in axisymmetric geometries governing equations are parameterized with the arclength (s). Note that the assumption of the axisymmetry diminishes the variation in the azimuthal (θ) direction. The equation of motion coupled with the continuity gives the shape equation and the velocity field. Mass conservation equations of proteins are solved to get the local protein distribution.

3.2 Flat membranes

3.2.1 Cahn-Hilliard equation

The mass conservation of proteins in the absence of flow and membrane bending depicts the aggregation-diffusion dynamics of the proteins and is known as the Cahn-Hilliard equation.

$$\phi_t = \nabla^2\phi\left[\frac{1}{1-\phi} - \hat{A}\phi\right] + |\nabla\phi|^2\left[\frac{1}{(1-\phi)^2} - \hat{A}\right] - \phi\left[\frac{\hat{A}}{2\hat{S}}\nabla^4\phi\right], \tag{3.1}$$

where $\nabla = \left(\frac{\partial}{\partial x}, \frac{\partial}{\partial y}\right)$ are the surface derivative, and $\hat{A}$ and $\hat{S}$ are two dimensionless numbers which are described in Table 5.1.

3.2.2 Solution algorithm

Equation (3.1) is solved for a periodic boundary with the help of finite difference technique with implicit time marching with time step Δt. The domain is discretized with spacially uniform grid points with the internal of Δx and Δy in x and y direction. The time derivative is discretized as first order backward differentiation as

$$\phi_t = \frac{\phi^n - \phi^{n-1}}{\Delta t}, \tag{3.2}$$

where $\Delta t = t^n - t^{n-1}$, is the time step. A central difference second order scheme is used to discretize derivatives in space as given by:

$$\nabla\phi = (\nabla_x\phi, \nabla_y\phi) = \left(\frac{\phi(x+\Delta x, y) - \phi(x-\Delta x, y)}{2\Delta x}, \frac{\phi(x, y+\Delta y) - \phi(x, y-\Delta y)}{2\Delta y}\right), \tag{3.3}$$

and

$$\nabla^2\phi = \frac{\phi(x+\Delta x,y)-2\phi(x,y)+\phi(x-\Delta x,y)}{\Delta x^2}+\frac{\phi(x,y+\Delta y)-2\phi(x,y)+\phi(x,y-\delta y)}{\Delta y^2}. \quad (3.4)$$

Note that the biharmonic term is splitted in two Laplacians as

$$\nabla^4\phi = \nabla^2\eta, \quad \text{where} \quad \eta = \nabla^2\phi. \quad (3.5)$$

Equation (3.1) is then represented in the linear system as

$$\begin{aligned} &a_E^n\ \phi(x+\Delta x,y)^n + a_W^n\phi(x-\Delta x,y)^n + a_N^n\phi(x,y+\Delta y)^n \\ &+ a_E^n\phi(x,y+\Delta y)^n + a_P\phi(x,y)^n = -\frac{\phi^{n-1}}{\Delta t}, \end{aligned} \quad (3.6)$$

where,

$$a_E = \frac{1}{\Delta x^2}\left[\frac{1}{1-\phi}-\hat{A}\phi\right]+\frac{\nabla_x\phi}{2\Delta x}\left[\frac{1}{(1-\phi)^2}-\hat{A}\right], \quad (3.7)$$

$$a_W = \frac{1}{\Delta x^2}\left[\frac{1}{1-\phi}-\hat{A}\phi\right]-\frac{\nabla_x\phi}{2\Delta x}\left[\frac{1}{(1-\phi)^2}-\hat{A}\right], \quad (3.8)$$

$$a_N = \frac{1}{\Delta y^2}\left[\frac{1}{1-\phi}-\hat{A}\phi\right]+\frac{\nabla_y\phi}{2\Delta y}\left[\frac{1}{(1-\phi)^2}-\hat{A}\right], \quad (3.9)$$

$$a_S = \frac{1}{\Delta y^2}\left[\frac{1}{1-\phi}-\hat{A}\phi\right]-\frac{\nabla_y\phi}{2\Delta y}\left[\frac{1}{(1-\phi)^2}-\hat{A}\right], \quad (3.10)$$

and

$$a_P = -\left(\frac{2}{\Delta y^2}+\frac{2}{\Delta y^2}\right)\left[\frac{1}{1-\phi}-\hat{A}\phi\right]-\left[\frac{\hat{A}}{2\hat{S}}\nabla^4\phi\right]-\frac{1}{\Delta t}. \quad (3.11)$$

To solve numerically Equation (3.1) in the solution domain we performed the following steps.

1. Initial condition is taken as the solution for the time step $n = 1$ $(t = 0)$.

2. For next time step $(n = 2)$, the values of ϕ is updated from Equation (3.6) by inverting the matrix with the help of Gauss-Seidel method

$$\phi(x,y)^n = \frac{1}{a_p}\Bigg[-\frac{\phi^{n-1}}{\Delta t} - \Bigg(a_E^n\ \phi(x+\Delta x,y)^n + a_W^n\phi(x-\Delta x,y)^n + a_N^n\phi(x,y+\Delta y)^n + a_E^n\phi(x,y+\Delta y)^n\Bigg)\Bigg]. \tag{3.12}$$

Note that the all the coefficient of the linear system a_E, a_W, a_N, a_S and a_P uses values of ϕ at current time step $n = 2$. To calculate them available values of ϕ are used.

3. Boundary conditions are updated using the periodic condition

$$\phi(x,1+\Delta y) = \phi(x,0) \quad \text{and} \quad \phi(1+\Delta x,y) = \phi(0,y). \tag{3.13}$$

4. With the update values of ϕ we updated the coefficients a_E, a_W, a_N, a_S and a_P and step 2 and 3 and repeat until convergence with in the time step $n = 2$.

5. Finally we move to next time step and follow the steps from step 2 to 4.

3.3 Small deformatons from the flat plane: Linear Monge

In this section we will discuss the solution schemes for the Monge patch. Note that both the shape (z), velocities $(\boldsymbol{u})$, and the density of proteins (σ) are function of space (x,y) and time (t),

$$z = z(x,y,t), \boldsymbol{u} = \boldsymbol{u}(x,y,t), \text{and,} \sigma = \sigma(x,y,t). \tag{3.14}$$

3.3.1 Coupled system of equations

The coupled system of equations for protein diffusion is presented in Chapter 4 and for aggregation are presented in Chapter 5 in detail. Here we present a system of equation for

aggregation-diffusion of proteins as an example for demonstrating the numerical methods. The tangential Equation (2.27) and normal stress balance Equation (2.28) relation expands to the following equations after using the free energy Equation (2.21) and the constitutive relation of stresses, as given in Equation (2.30).

$$\begin{aligned}\nabla\lambda+\nabla^2\boldsymbol{v}+\nabla(\nabla\cdot\boldsymbol{v})-4w\nabla H-2\nabla w:\nabla\nabla z=\\ -\nabla\phi\left[\frac{2\hat{B}\hat{S}}{\hat{T}}\log\frac{\phi}{1-\phi}-\frac{4\hat{L}\hat{S}}{\hat{T}}(H-\hat{L}\hat{S}\phi)-\frac{\hat{A}\hat{B}\hat{S}}{\hat{T}}(2\phi-1)-\frac{\hat{A}\hat{B}}{\hat{T}}\nabla^2\phi\right],\end{aligned} \tag{3.15}$$

and

$$\begin{aligned}&\nabla^4 z-2\hat{L}\hat{S}\nabla^2\phi-2\hat{B}\hat{S}\nabla^2 z\left[\{\phi\log\phi+(1-\phi)\log(1-\phi)\}+\frac{\hat{A}}{2}\phi(1-\phi)+\frac{\hat{A}}{4\hat{S}}|\nabla\phi|^2+\frac{\hat{L}^2\hat{S}}{\hat{B}}\phi^2\right]\\ &-\hat{T}(\nabla\boldsymbol{v}+\nabla\boldsymbol{v}^T):\nabla\nabla z=p+\hat{T}\lambda\nabla^2 z.\end{aligned} \tag{3.16}$$

Here $\hat{L}$, $\hat{B}$, and $\hat{T}$ are the dimensionless numbers described in Table 5.1. $\nabla=\left(\frac{\partial}{\partial x},\frac{\partial}{\partial y}\right)$ are the surface derivative with respect to the projected plane (x,y), λ is the membrane tension that was introduced as the Lagrange multiplier for incompressibility of the membrane. The incompressibility relation is described by the continuity equation as

$$\nabla\cdot\boldsymbol{v}=2wH,. \tag{3.17}$$

Finally, the mass conservation of the protein (Equation (2.34)) is given by the equation density field as:

$$\begin{aligned}\phi_t+Pe\,\nabla\cdot(\boldsymbol{v}\phi)=\nabla^2\phi\left[\frac{1}{1-\phi}+\frac{2\hat{L}^2\hat{S}}{\hat{B}}\phi-\hat{A}\phi\right]-\phi\left[\frac{2\hat{L}}{\hat{B}}\nabla^2 H+\frac{\hat{A}}{2\hat{S}}\nabla^4\phi\right]\\ +\nabla\phi\cdot\left[\nabla\phi\left(\frac{1}{(1-\phi)^2}+\frac{2\hat{L}^2\hat{S}}{\hat{B}}-\hat{A}\right)-\frac{2\hat{L}}{\hat{B}}\nabla H-\frac{\hat{A}}{2\hat{S}}\nabla(\nabla^2\phi)\right].\end{aligned} \tag{3.18}$$

3.3.2 Solution algorithm

Note that our governing equation has time dependence only in the transport equation for proteins. All other equations equilibrium equation depends on the value of ϕ as current time. Our solution algorithm is second order in space and first order in time. We first discretized the governing equation with the help of finite difference technique as presented in Section 3.2.2. The biharmoic term in the shape equation is spilled into two Poisson's equation as given by

$$\nabla^4 z = \nabla^2 \zeta \tag{3.19}$$

where

$$\zeta = \nabla^2 z. \tag{3.20}$$

The transport equation for protein is discretized in the same manner as described in Equation (3.6). The shape equation (Equation (3.16)) and tangential force balance equation (Equation (3.15)) are solved in two different ways depending on boundary conditions.

Clamped and no-flux boundary conditions

For clamped boundary condition, $z = 0$ and $\boldsymbol{\tau} \cdot \boldsymbol{\nabla} z = 0$, where $\boldsymbol{\tau}$ is the outward normal at the boundary. No-flux bounday is considered for proteins that satisfies $\boldsymbol{\tau} \cdot \boldsymbol{m} = 0$. A open boundary for velocity and the tension is considered, which is described in detail in the tension boundary condition paragraph. The equation for protein density in Equation (3.18) is discretized by

$$\begin{aligned} &a_E^n \ \phi(x+\Delta x, y)^n + a_W^n \phi(x-\Delta x, y)^n + a_N^n \phi(x, y+\Delta y)^n \\ &+ a_E^n \phi(x, y+\Delta y)^n + a_P \phi(x, y)^n = -\frac{\phi^{n-1}}{\Delta t}. \end{aligned} \tag{3.21}$$

The shape equation (Equation (3.16)) is discretized as a Poisson's equation of ζ

$$\begin{aligned} &h_E^n\ \zeta(x+\Delta x,y)^n + h_W^n\ \zeta(x-\Delta x,y)^n + h_N^n\ \zeta(x,y+\Delta y)^n \\ &+ h_S^n\ \zeta(x,y+\Delta y)^n + h_P\zeta(x,y)^n = H^n(x,y), \end{aligned} \tag{3.22}$$

where H is the non-homogeneous part of the Poisson's equation and the coefficients are given by

$$h_E = \frac{1}{\Delta x^2}, \quad h_W = \frac{1}{\Delta x^2}, \quad h_N = \frac{1}{\Delta y^2}, \quad h_S = \frac{1}{\Delta x^2}, \quad \text{and} \quad h_P = -\frac{2}{\Delta x^2} - \frac{2}{\Delta y^2}. \tag{3.23}$$

The Poisson's equation of z in the discretized form is given by

$$\begin{aligned} &h_E^n\ z(x+\Delta x,y)^n + h_W^n\ z(x-\Delta x,y)^n + h_N^n\ z(x,y+\Delta y)^n \\ &+ h_S^n\ z(x,y+\Delta y)^n + h_P z(x,y)^n = \zeta^n(x,y), \end{aligned} \tag{3.24}$$

A Poisson's equation for pressure is derived from Equation (3.15), is shown in Equation (4.25) in detail, and is dicretized as

$$\begin{aligned} &h_E^n\ \lambda(x+\Delta x,y)^n + h_W^n\ \lambda(x-\Delta x,y)^n + h_N^n\ \lambda(x,y+\Delta y)^n \\ &+ h_S^n\ \lambda(x,y+\Delta y)^n + h_P\lambda(x,y)^n = Q^n(x,y), \end{aligned} \tag{3.25}$$

The algebric equation for the velocity field is given by

$$\begin{aligned} &h_E^n\ \boldsymbol{v}(x+\Delta x,y)^n + h_W^n\ \boldsymbol{v}(x-\Delta x,y)^n + h_N^n\ \boldsymbol{v}(x,y+\Delta y)^n \\ &+ h_S^n\ \boldsymbol{v}(x,y+\Delta y)^n + h_P\boldsymbol{v}(x,y)^n = -\boldsymbol{\nabla}\lambda + B^n(x,y), \end{aligned} \tag{3.26}$$

Tension at boundary An open boundary for velocity and tension is considered. The tension at the boundary is calculated with the help of 2-D Stokeslet as shown in Equation (4.27) in detail. The solution steps in the clamped and no-flux boundary condition is given here:

1. Initial condition is taken as the solution for the time step $n = 1(t = 0)$, solve for shape

corresponds to the initial protein density.

2. For next time step $(n = 2)$, the values of ϕ is updated from Equation (3.21) by inverting the matrix with the help of Gauss-Seidel method

$$\phi(x,y)^n = \frac{1}{a_p}\left[-\frac{\phi^{n-1}}{\Delta t} - \left(a_E^n\ \phi(x+\Delta x,y)^n + a_W^n\phi(x-\Delta x,y)^n + a_N^n\phi(x,y+\Delta y)^n + a_E^n\phi(x,y+\Delta y)^n\right)\right]. \tag{3.27}$$

Note that the all the coefficient of the linear system a_E, a_W, a_N, a_S and a_P uses values of ϕ at current time step $n = 2$. To calculate them use the current available values of ϕ.

3. Shape of the membrane is updated (Equation (3.16)) is updated using the the discretized shape equation (Equation (3.22) and Equation (3.24))with the current values of ϕ.

4. Normal velocity is calculated as the backward derivative of shape

$$w^n = \frac{1}{Pe}\frac{z^n - z^{n-1}}{\Delta t}. \tag{3.28}$$

5. Assign boundary conditions for λ from the technique given in Equation (4.27) in detail.

6. Membrane tension λ is updated using the the discretized Poisson's equation (Equation (3.25)) with the current values of ϕ.

7. With the calculated value of λ velocity field $\boldsymbol{v}$ is calculated from discretized Poisson's equation for velocity in Equation (3.26).

8. With the updated values of ϕ all the coefficients of discretized equations are updated and the process is repeated from step 2 until convergence with in the time step $n = 2$.

9. Next we move to next time step and follow the steps from step 2.

Periodic boundary condition

In chapter 5, the governing equation is solved for a periodic boundary conditions for velocity tension and

Fourier Spectral Technique The tangential force balance relation in Equation (3.15) along with continuity Equation (3.17) can be simplified in the following form of a 2D Stokes equation with a dilation component s as given by

$$\begin{aligned} -\nabla^2 v + \nabla p &= f, \\ \nabla \cdot v &= s. \end{aligned} \tag{3.29}$$

The velocity and the surface pressure can be represented in terms of the Fourier series as [113]

$$\begin{aligned} \boldsymbol{V} &= \sum_k \boldsymbol{V}_k e^{-2\pi i(\boldsymbol{k}\cdot\boldsymbol{r})} \\ -\boldsymbol{\nabla} p &= \sum_k \boldsymbol{P}_{\boldsymbol{k}} e^{-2\pi i(\boldsymbol{k}\cdot\boldsymbol{r})} \end{aligned} \tag{3.30}$$

We get the expression of velocity and pressure from Equation (3.29) at Fourier space given by

$$\begin{aligned} \boldsymbol{V}_k &= \frac{1}{4\pi^2 k^2}\left(\boldsymbol{F}_k - \frac{(\boldsymbol{k}\cdot\boldsymbol{F}_k)\,\boldsymbol{k}}{k^2} + 2\pi S_k \boldsymbol{k} i\right) \\ P_k &= S_k + \frac{\boldsymbol{k}\cdot\boldsymbol{F}_k}{2\pi k^2} i. \end{aligned} \tag{3.31}$$

Here S_k and $\boldsymbol{F}_k$ Fourier coefficients of s and $\boldsymbol{f}$. In the similar way the shape equation (Equation (3.16)) can be solved with the help of spectral technique by splitting the biharmonic term into two Laplacian as shown in Equation (3.19) and Equation (3.20), and we obtain two Poisson's equation in the form of

$$\nabla^2 \varphi = \beta. \tag{3.32}$$

and further φ can be written with the help of Fourier series as

$$\varphi = \sum_k \Phi_k e^{-2\pi i(\boldsymbol{k}\cdot\boldsymbol{r})}. \tag{3.33}$$

and we obtain the Fourier coefficient as

$$\Phi_k = -\frac{B_k}{4\pi^2 k^2}, \tag{3.34}$$

where B_k is the Fourier transform of inhomogeneous part of the Poisson's equation β.

1. Initial condition is taken as the solution for the time step $n = 1(t = 0)$.

2. For next time step $(n = 2)$, the values of ϕ is updated from Equation (3.21) by inverting the matrix with the help of Gauss-Seidel method

$$\begin{aligned}\phi(x,y)^n = \frac{1}{a_p}\Bigg[-\frac{\phi^{n-1}}{\Delta t} - \Bigg(a_E^n\ \phi(x+\Delta x,y)^n + a_W^n \phi(x-\Delta x,y)^n + a_N^n \phi(x,y+\Delta y)^n \\ + a_E^n \phi(x,y+\Delta y)^n \Bigg)\Bigg].\end{aligned} \tag{3.35}$$

   a_E, a_W, a_N, a_S and a_P uses available values of ϕ at current time step $n = 2$.

3. Shape equation is updated using the spectral solution of the two consecutive Poisson's equation as given in Equation (3.34).

4. Normal velocity is calculated as the backward derivative of shape

$$w^n = \frac{1}{Pe}\frac{z^n - z^{n-1}}{\Delta t}. \tag{3.36}$$

5. Velocity and tension is updated using spectral technique given in Equation (3.31) with the current values of ϕ.

6. With the updated values of ϕ we updated the coefficients a_E, a_W, a_N, a_S and a_P for ϕ equation and the process is repeated from step 2 until convergence with in the time step $n = 2$.

7. Next we move to next time step and follow the steps from step 2.

3.4 Axisymmetric membranes

3.4.1 Parameterization

In the case of axisymmetry we used the arc-length (s) patameterization in Chapter 4 and Chapter 6 where the domain area is kept constant. The value of arclength varied to maintain the total area. The strategy is presented in Section 4.4.3. However, in Chapter 7 we used area parameterization to solve the equilibrium shape of the membrane for a prescribed protein distribution.

3.4.2 Coupled system of equations

The tangential force balance relation (Equation (2.27)) reduces to

$$\begin{aligned}\frac{\partial \lambda}{\partial s} - 4w\frac{\partial H}{\partial s} + 2(2\frac{\partial wH}{\partial s} + Kv_s - \frac{\partial w}{\partial s}\frac{\partial \psi}{\partial s}) = -\frac{\partial \phi}{\partial s}\Bigg[\frac{2\hat{B}\hat{S}}{\hat{T}}\log\frac{\phi}{1-\phi} \\ - \frac{4\hat{L}\hat{S}}{\hat{T}}(\tilde{H} - \hat{L}\hat{S}\phi) - \frac{\hat{A}\hat{B}\hat{S}}{\hat{T}}(2\phi - 1) - \frac{\hat{A}\hat{B}}{\hat{T}}\Delta\phi - \frac{2\hat{M}\hat{B}\hat{S}}{\hat{T}}\Bigg]\end{aligned} \tag{3.37}$$

where $\Delta(\cdot) = \frac{1}{r}\frac{\partial}{\partial s}\left(r\frac{\partial(\cdot)}{\partial s}\right)$, is the Laplacian operator of a scalar field. The continuity ( ) is denoted here as

$$\frac{1}{r}\frac{\partial(rv^s)}{\partial s} = 2wH. \tag{3.38}$$

The shape equation (Equation (2.28)) is presented here in a series of two first order ODEs as given by

$$\begin{aligned}
&\frac{1}{r}\frac{\partial L}{\partial s} + 2(H - \ell\sigma_0 L\sigma)(2H^2 - K) - 2\hat{B}\hat{S}\tilde{H}\left[\phi\log\phi + (1-\phi)\log(1-\phi) + \frac{\hat{A}}{2}\phi(1-\phi)\right. \\
&\left. + \frac{\hat{A}}{4\hat{S}}\left|\frac{\partial\phi}{\partial s}\right|^2 - \hat{M}\phi\right] + \frac{\gamma}{2k_BT}\phi(1-\phi) + \frac{\gamma}{4K_BT\sigma_s L^2}\left|\frac{\partial\phi}{\partial s}\right|^2 - \frac{\mu_b}{k_BT}\phi\Big] \\
&- \hat{T}\left[\psi_s\frac{\partial(rv^s)}{\partial s} + \frac{\sin\psi\cos\psi v^s}{r^2} - w(4H^2 - 2K)\right] = p + \hat{T}\lambda H
\end{aligned} \tag{3.39}$$

with,

$$\frac{L}{r} = \left[\frac{\partial H}{\partial s} - \hat{L}\hat{S}\frac{\partial\sigma}{\partial s}\right] \tag{3.40}$$

The aggregation diffusion equation of protein (Equation (2.21)) with a source of protein density Q takes the following form

$$\begin{aligned}
\phi_{,t} + Pe\,\frac{\partial(\tilde{v^s}\phi)}{\partial s} &= \Delta\phi\left[\frac{1}{1-\phi} + \frac{2\hat{L}^2\hat{S}}{\hat{B}}\phi - \hat{A}\phi\right] - \phi\left[\frac{2\hat{L}}{\hat{B}}\Delta H + \frac{\hat{A}}{2\hat{S}}\Delta^2\phi\right] \\
&+ \frac{\partial\phi}{\partial s}\left[\frac{\partial\phi}{\partial s}\left(\frac{1}{(1-\phi)^2} + \frac{2\hat{L}^2\hat{S}}{\hat{B}} - \hat{A}\right) - \frac{2\hat{L}}{\hat{B}}\frac{\partial\tilde{H}}{\partial s} - \frac{\hat{A}}{2\hat{S}}\frac{\partial(\Delta\phi)}{\partial s}\right] + Q(\phi,\Phi).
\end{aligned} \tag{3.41}$$

The above system of equations involves several dimensionless groups as given in Table 6.1.

3.4.3 Solution algorithm

The solution arclength domain is discretized in finite grid points. The distance between the grid points are varied. The space $\Delta s_{i-1} = s_i - s_{i-1}$ changes and the ratio $\alpha = \Delta s_i/\Delta s_{i-1}$ is kept constant throughout the domain. We used a numerical scheme which is first order in time and second order in space. The discrete time derivative remains same as before. However, the space derivatives are modified as

$$\left(\frac{\partial \varphi}{\partial s}\right)_i = \frac{\varphi_{i+1} - (1-\alpha^2)\varphi_i - \alpha^2 \varphi_{i-1}}{\Delta s_{i-1}\alpha(1+\alpha)}, \tag{3.42}$$

and

$$\left(\frac{\partial^2 \varphi}{\partial s^2}\right)_i = \frac{2\left(\varphi_{i+1} - (1+\alpha)\varphi_i + \alpha\varphi_{i-1}\right)}{\Delta s_{i-1}^2 \alpha(1+\alpha)}. \tag{3.43}$$

The transport equation for proteins (Equation (3.41)) is discretized as

$$a_E^n\ \phi_{i+1}^n + a_W^n \phi_{i-1}^n + a_P^n \phi_i^n = \left[-Q - \frac{\phi^{n-1}}{\Delta t} \right]. \tag{3.44}$$

1. Initial condition is taken as the solution for the time step $n = 1 (t = 0)$, solve for shape corresponds to the initial protein density.

2. For next time step $(n = 2)$, the values of ϕ is updated from Equation (3.21) by inverting the matrix with the help of Gauss-Seidel method

$$\phi_i^n = \frac{1}{a_p}\left[-Q - \frac{\phi^{n-1}}{\Delta t} - \left(a_E^n\ \phi_{i+1}^n + a_W^n \phi_{i-1}^n \right) \right]. \tag{3.45}$$

   Note that the all the coefficient of the linear system a_E, a_W and a_P uses values of ϕ at current time step $n = 2$. To calculate them use the current available values of ϕ.

3. Shape of the membrane is updated from the updated values of L that is obtained by integrating Equation (3.37) with the boundary condition of L at the center. The strategy of fining shape (r, z) for each grid points is discussed in Section 4.4.3.

4. Normal velocity is calculated as the backward derivative of shape

$$w^n = \frac{1}{Pe}\boldsymbol{n} \cdot \left[\frac{\boldsymbol{r}^n - \boldsymbol{r}^{n-1}}{\Delta t} \right]. \tag{3.46}$$

5. Tangential velocity is calculated by integrating continuity in Equation (3.38).

6. Membrane tension λ is updated by integrating tangential force balance relation (Equation (3.37)) backward in the arclength from the boundary condition of λ_0.

7. With the updated values of ϕ all the coefficients of discretized equations are updated and the process is repeated from step 2 until convergence with in the time step $n = 2$.

8. Next we move to next time step and follow the steps from step 2.

3.4.4 Equilibrium solution

The equilibrium solution for membrane shape and tension for prescribed protein density (and therefore spontaneous curvature) is presented in Chapter 7. We use a local area a for parameterizing the membrane, that relates to the local arclength as $da = 2\pi r ds$. The derivatives with respect to arclength is changed as

$$\frac{\partial(\cdot)}{\partial s} = 2\pi r \frac{\partial(\cdot)}{\partial a}. \tag{3.47}$$

The solution method is exactly same with the arclength parameterization. Steps 3-6 is performed to obtain an equilibrium shape.

Chapter 4

Diffusion of curvature-inducing proteins coupled with membrane bending and in-plane lipid flow

4.1 Introduction

In this chapter we focus on the interplay of protein-diffusion, lipid flow, and membrane bending with the help a comprehensive theoretical model and subsequent numerical simulation. The seminal work of Helfrich [36], Canham[52], and Jenkins [54] established the framework for using variational principles and thin shell mechanics for modeling membrane bending. Later, [55] established the correspondence between Koiter's shell theory and developed a complete theoretical framework of membrane mechanics. These early models assumed the membrane to be inviscid and focused primarily on elastic effects. In the past decade, many groups have proposed the addition of viscous effects in addition to membrane bending [62, 63, 64, 65] building on the ideas proposed by [66]. We also showed recently that including intrasurface viscosity in addition to membrane bending allows for the calculation of local membrane tension in the presence of

protein-induced spontaneous curvature [67] and for the calculation of flow fields on minimal surfaces [68]. Separately, the interaction between in-plane protein diffusion and membrane bending has been modeled [69, 70, 71, 72, 73, 15]. Specifically, [74] proposed a framework that included the chemical potential energy of membrane-protein interactions and membrane bending and demonstrated the interaction between bending and diffusion. A series of studies by Arroyo and coworkers also developed a comprehensive framework for incorporating membrane-protein interactions using Onsager's variational principles [75, 65, 76].

We present here a coupled theory for membrane mechanics that accounts for in-plane viscous flows and diffusion of curvature-inducing transmembrane proteins in addition to membrane bending. We note that a version of this model was presented by [115]. Using a free energy functional that includes bending energy, chemical potential energy of membrane-protein interactions, and by including the viscous stresses in the force balance, we derive the governing equations of motion in § 4.2. In § 4.3.1, we analyze this system of equations assuming small deformations from the flat plane and identify the role of different dimensionless groups in governing the regimes of operation. We then perform numerical simulations in a one-dimensional model in § 4.3.2 and in a two-dimensional Monge parametrization in § 4.3.3. The case of large deformations is addressed in § 4.4 where we investigate the flattening of a membrane bud in axisymmetric coordinates.

4.2 Membranes with intra-surface viscosity and protein diffusion

We formulate the governing equations for the dynamics of an elastic lipid membrane with surface flow, coupled to the transport of membrane-embedded proteins that induce spontaneous mean curvature. The notations used in the model are summarized in Table 4.1. We assume familiarity with tensor analysis and curvilinear coordinate systems [116, 117, 118].

4.2.1 Free energy of an elastic membrane with curvature-inducing proteins

For an elastic membrane with a dilute density σ of curvature-inducing proteins, the free energy presented in Equation (2.34) as the sum of elastic and chemical energies reduces to [71, 74, 119]

$$W(H,K,\sigma) = \kappa[H - C(\sigma)]^2 + \bar{\kappa}K + k_B T\,\sigma\left[\log\left(\frac{\sigma}{\sigma_s}\right) - 1\right]. \tag{4.1}$$

The first two terms correspond to the classical Helfrich free energy and involve the two bending moduli k and $\bar{k}$. While these could in general depend on σ, we take them to be constant as is appropriate in the dilute limit. $C(\sigma)$ is the protein-induced spontaneous curvature and is assumed to depend linearly on protein density [71, 74, 120]:

$$C = \ell\sigma, \tag{4.2}$$

where the constant ℓ is a characteristic length scale associated with the embedded protein. The last term in Equation (4.1) is the entropic contribution due to thermal diffusion of proteins [120], where $k_B T$ is the thermal energy and σ_s denotes the saturation density of proteins on the membrane.

Inserting Equation (4.1) for the free energy into Equation (2.30) provides expressions for the elastic stress and moment tensors as

$$\zeta^{\alpha\beta} = -2\kappa(H - \ell\sigma)b^{\alpha\beta} - 2\bar{\kappa}Ka^{\alpha\beta} - \xi a^{\alpha\beta}, \tag{4.3}$$

$$M^{\alpha\beta} = \kappa(H - \ell\sigma)a^{\alpha\beta} + \bar{\kappa}(2Ha^{\alpha\beta} - b^{\alpha\beta}). \tag{4.4}$$

4.2.2 Summary of the governing equations

We summarize the governing equations for the membrane and protein dynamics. The tangential momentum balance, obtained by inserting equations (4.3), (4.4) and (2.33) for the stresses into the equation (2.27), is expressed as

$$\lambda_{,\alpha} - 4\nu w H_{,\alpha} + 2\nu(a^{\beta\mu} d_{\alpha\mu;\beta} - w_{,\beta} b^{\beta}_{\alpha}) = -\sigma_{,\alpha}\Big[k_B T \log\Big(\frac{\sigma}{\sigma_s}\Big) - 2\kappa\ell(H-\ell\sigma)\Big], \tag{4.5}$$

where we have introduced the membrane tension $\lambda = -(W+\gamma)$. Along with the surface incompressibility condition

$$v^{\alpha}_{;\alpha} - 2wH = 0, \tag{4.6}$$

Equation (4.5) constitutes the governing equation for the intra-membrane flow. We note the similarity with the Stokes equations, where the tension λ plays a role analogous to the pressure in classical incompressible flow [68]. The right-hand side captures the forcing by the protein distribution on the flow. Similarly, the normal force balance in Equation (2.28) provides the so-called *shape equation*, written after simplifications as

$$\begin{aligned} k\Delta(H-\ell\sigma) + 2k(H-\ell\sigma)(2H^2-K) - 2H\Big[k_B T\sigma\Big(\log\Big(\frac{\sigma}{\sigma_s}\Big) - 1\Big) + \kappa(H-\ell\sigma)^2\Big] \\ - 2\nu\big[b^{\alpha\beta} d_{\alpha\beta} - w(4H^2 - 2K)\big] = p + 2\lambda H, \end{aligned} \tag{4.7}$$

where $\Delta(\cdot) = (\cdot)_{;\alpha\beta} a^{\alpha\beta}$ is the surface Laplacian. Equation (4.7) can be interpreted as the governing equation for the position field $\boldsymbol{r}$. Finally, the model is completed by the advection-diffusion equation for the protein density, which is written

$$\frac{\partial\sigma}{\partial t} + (v^{\alpha}\sigma)_{;\alpha} = D a^{\alpha\beta}\sigma_{,\alpha\beta} - \frac{2k\ell}{f}\big[a^{\alpha\beta}(H-\ell\sigma)_{,\alpha}\sigma_{,\beta} + \sigma a^{\alpha\beta}(H-\ell\sigma)_{,\alpha\beta}\big]. \tag{4.8}$$

Table 4.1: Summary of the notations used in the model of protein diffusion

Notation	Description	Units
γ	Lagrange multiplier for incompressibility	$\mathrm{pN}\cdot\mathrm{nm}^{-1}$
p	Pressure difference across the membrane	$\mathrm{pN}\cdot\mathrm{nm}^{-2}$
C	Protein-induced spontaneous curvature	nm^{-1}
θ^{α}	Surface coordinates	
W	Local free energy per unit area	$\mathrm{pN}\cdot\mathrm{nm}^{-1}$
λ	Membrane tension, $\lambda = -(W+\gamma)$	$\mathrm{pN}\cdot\mathrm{nm}^{-1}$
λ_0	Membrane tension at infinity	$\mathrm{pN}\cdot\mathrm{nm}^{-1}$
$\zeta^{\alpha\beta}$	Elastic stress tensor	$\mathrm{pN}\cdot\mathrm{nm}^{-1}$
$\pi^{\alpha\beta}$	Viscous deviatoric stress	$\mathrm{pN}\cdot\mathrm{nm}^{-1}$
H	Mean curvature of the membrane	nm^{-1}
K	Gaussian curvature of the membrane	nm^{-2}
κ	Bending modulus (rigidity)	$\mathrm{pN}\cdot\mathrm{nm}$
$\bar{\kappa}$	Gaussian modulus	$\mathrm{pN}\cdot\mathrm{nm}$
σ	Protein density per unit area	nm^{-2}
σ_s	Saturation protein density per unit area	nm^{-2}
ℓ	Proportionality constant of $C-\sigma$ relation	nm
D	Protein diffusion coefficient, $D = k_B T/f$	$\mathrm{nm}^2\cdot\mathrm{s}^{-1}$
f	Hydrodynamic drag coefficient of a protein	$\mathrm{pN}\cdot\mathrm{s}\cdot\mathrm{nm}^{-1}$
L	Size of the domain	nm
k_B	Boltzmann constant	$\mathrm{pN}\cdot\mathrm{nm}\cdot\mathrm{K}^{-1}$
T	Temperature	K

The first term on the right-hand side captures Fickian diffusion of proteins, with diffusivity D given by the Stokes-Einstein relation: $D = k_B T/f$. The second term captures the interaction of the curvature and protein gradients. The third term captures the effect of membrane shape on protein transport: mismatch between the mean curvature and the protein-induced spontaneous curvature serves as a source term for the transport of protein on the membrane surface.

4.3 Small deformations from the flat plane

4.3.1 Linearization and dimensional analysis

In this section, we specialize the governing equations presented in § 4.2.2 in a Monge parametrization assuming small deflections from the flat plane.

Governing equations in the linear deformation regime

The surface parametrization for a Monge patch is given by

$$\boldsymbol{r}(x,y,t) = x\boldsymbol{i} + y\boldsymbol{j} + z(x,y,t)\boldsymbol{k}, \tag{4.9}$$

where unit vectors $(\boldsymbol{i},\boldsymbol{j},\boldsymbol{k})$ form a fixed Cartesian orthonormal basis, and $z(x,y,t)$ is the deflection from the (x,y) plane. The tangent and normal vectors are given by

$$\boldsymbol{a}_1 = \boldsymbol{i} + z_{,x}\boldsymbol{k}, \quad \boldsymbol{a}_2 = \boldsymbol{j} + z_{,y}\boldsymbol{k}, \quad \boldsymbol{n} = \frac{1}{(1+z_{,x}^2+z_{,y}^2)^{1/2}}(-z_{,x}\boldsymbol{i} - z_{,y}\boldsymbol{j} + \boldsymbol{k}). \tag{4.10}$$

The surface metric $(a_{\alpha\beta})$ and curvature metric $(b_{\alpha\beta})$ take the following forms

$$a_{\alpha\beta} = \begin{bmatrix} 1+z_{,x}^2 & z_{,x}z_{,y} \\ z_{,y}z_{,x} & 1+z_{,y}^2 \end{bmatrix}, \quad b_{\alpha\beta} = \frac{1}{(1+z_{,x}^2+z_{,y}^2)^{1/2}} \begin{bmatrix} z_{,xx} & z_{,xy} \\ z_{,yx} & z_{,yy} \end{bmatrix}. \tag{4.11}$$

We further assume that deflections of the membrane from the flat configuration are small and simplify the governing equations in the limit of weak surface gradients $|\boldsymbol{\nabla} z| \ll 1$ by neglecting quadratic terms in $|\boldsymbol{\nabla} z|$ [121]. In this limit, differential operators in the space of the membrane reduce to the Cartesian gradient, divergence and Laplacian in the (x,y) plane. The linearized

governing equations for the intra-membrane flow become:

$$\boldsymbol{\nabla}\cdot\boldsymbol{v} = 2wH, \tag{4.12}$$

$$\begin{aligned}\boldsymbol{\nabla}\lambda + \nu\nabla^2\boldsymbol{v} + \nu\boldsymbol{\nabla}(\boldsymbol{\nabla}\cdot\boldsymbol{v}) - 4\nu w\boldsymbol{\nabla}H - 2\nu\boldsymbol{\nabla}w : \boldsymbol{\nabla}\boldsymbol{\nabla}z \\ = \kappa\left(\nabla^2 z - 2\ell\sigma\right)\ell\,\boldsymbol{\nabla}\sigma - k_B T\log\left(\frac{\sigma}{\sigma_s}\right)\boldsymbol{\nabla}\sigma,\end{aligned} \tag{4.13}$$

whereas the shape equation expressing the normal momentum balance is

$$\begin{aligned}\kappa\left(\tfrac{1}{2}\nabla^4 z - \ell\nabla^2\sigma\right) - \nabla^2 z\left[k_B T\sigma\left(\log\left(\frac{\sigma}{\sigma_s}\right) - 1\right) + \kappa\ell^2\sigma^2\right] \\ -\nu\left(\boldsymbol{\nabla}\boldsymbol{v} + \boldsymbol{\nabla}\boldsymbol{v}^T\right) : \boldsymbol{\nabla}\boldsymbol{\nabla}z = p + \lambda\nabla^2 z.\end{aligned} \tag{4.14}$$

The transport equation for the protein density simplifies to

$$\frac{\partial\sigma}{\partial t} + \boldsymbol{\nabla}\cdot(\sigma\boldsymbol{v}) = D\nabla^2\sigma - \frac{\kappa\ell}{f}\boldsymbol{\nabla}\left(\nabla^2 z - 2\ell\sigma\right)\cdot\boldsymbol{\nabla}\sigma - \frac{\kappa\ell\sigma}{f}\left(\nabla^4 z - 2\ell\nabla^2\sigma\right). \tag{4.15}$$

We also note the linearized kinematic relation for the normal velocity:

$$w = \frac{\partial z}{\partial t}. \tag{4.16}$$

Non-dimensionalization

We scale this system of equations using the following reference values. Length is non-dimensionalized by the size L of the domain, protein density by its reference value σ_0, and membrane tension by its far-field value λ_0. We also use the characteristic velocity scale $v_c = \lambda_0 L/\nu$ and time scale $t_c = L^2/D$. Denoting dimensionless variables with a tilde, the scaled governing

equations are:

$$\tilde{\boldsymbol{\nabla}} \cdot \tilde{\boldsymbol{v}} = 2\tilde{w}\tilde{H}, \tag{4.17}$$

$$\begin{aligned} \tilde{\boldsymbol{\nabla}}\tilde{\lambda} + \tilde{\nabla}^2\tilde{\boldsymbol{v}} + \tilde{\boldsymbol{\nabla}}(\tilde{\boldsymbol{\nabla}} \cdot \tilde{\boldsymbol{v}}) - 4\tilde{w}\tilde{\boldsymbol{\nabla}}\tilde{H} - 2\tilde{\boldsymbol{\nabla}}\tilde{w} : \tilde{\boldsymbol{\nabla}}\tilde{\boldsymbol{\nabla}}\tilde{z} = \\ \tilde{\boldsymbol{\nabla}}\tilde{\sigma}\left[\frac{2\hat{C}\hat{B}}{\hat{T}}\tilde{\nabla}^2\tilde{z} - \frac{4\hat{C}^2\hat{B}^2}{\hat{T}}\tilde{\sigma} - \frac{2\hat{C}}{\hat{T}}\log\left(\frac{\tilde{\sigma}}{\tilde{\sigma}_s}\right)\right], \end{aligned} \tag{4.18}$$

$$\begin{aligned} \tilde{\nabla}^4\tilde{z} - 2\hat{C}\hat{B}\,\tilde{\nabla}^2\tilde{\sigma} - \hat{C}\tilde{\nabla}^2\tilde{z}\left[2\tilde{\sigma}\left(\log\left(\frac{\tilde{\sigma}}{\tilde{\sigma}_s}\right) - 1\right) + 2\hat{C}\hat{B}^2\tilde{\sigma}^2\right] \\ - \hat{T}(\tilde{\boldsymbol{\nabla}}\tilde{\boldsymbol{v}} + \tilde{\boldsymbol{\nabla}}\tilde{\boldsymbol{v}}^T) : \tilde{\boldsymbol{\nabla}}\tilde{\boldsymbol{\nabla}}\tilde{z} = \hat{P} + \hat{T}\,\tilde{\lambda}\,\tilde{\nabla}^2\tilde{z}, \end{aligned} \tag{4.19}$$

$$\begin{aligned} \frac{\partial\tilde{\sigma}}{\partial\tilde{t}} + Pe\big(\tilde{\boldsymbol{v}} \cdot \tilde{\boldsymbol{\nabla}}\tilde{\sigma} + \tilde{\sigma}\tilde{\boldsymbol{\nabla}} \cdot \tilde{\boldsymbol{v}}\big) = \big(1 + 2\hat{C}\hat{B}^2\tilde{\sigma}\big)\tilde{\nabla}^2\tilde{\sigma} \\ + 2\hat{C}\hat{B}^2|\tilde{\boldsymbol{\nabla}}\tilde{\sigma}|^2 - \hat{B}\big(\tilde{\sigma}\tilde{\nabla}^4\tilde{z} + \tilde{\boldsymbol{\nabla}}\tilde{\nabla}^2\tilde{z} \cdot \tilde{\boldsymbol{\nabla}}\tilde{\sigma}\big). \end{aligned} \tag{4.20}$$

The expression for the normal velocity also becomes:

$$\tilde{w} = \frac{1}{Pe}\frac{\partial\tilde{z}}{\partial\tilde{t}}. \tag{4.21}$$

The dynamics are governed by five dimensionless parameters defined as follows. The ratio of the chemical potential to the bending rigidity of the membrane is denoted by $\hat{C} = L^2 k_B T \sigma_0/\kappa$. The ratio of the length scale induced by the proteins and the membrane domain is given by $\hat{L} = \ell L \sigma_0$. The ratio of the intrinsic length scale of the membrane to the domain size is given by $\hat{T} = 2L^2\lambda_0/\kappa$. The ratio between the bulk pressure and bending rigidity is denoted by $\hat{P} = 2L^3 p/\kappa$. Finally, the Péclet number $Pe = \lambda_0 L^2/\nu D$ compares the advective transport rate to the diffusive transport rate. We define $\hat{B} = \hat{L}/\hat{C}$ for convenience of simulations and cast the equations in terms of $\hat{L}$, $\hat{B}$, $\hat{T}$, and Pe. Further, we assume that there is no pressure difference across the membrane ($\hat{P} = 0$).

4.3.2 One-dimensional simulations

We first explore the interplay between membrane bending and protein diffusion in the special case of a membrane that deforms as a string in one dimension, with a shape parameterized as $\tilde{z}(\tilde{x},\tilde{t})$. The flow of lipids does not play a role in this scenario, and as a result in-plane velocity-dependent terms vanish in equations (4.17)–(4.20). The system of governing equations reduces to

$$\frac{\partial\tilde{\lambda}}{\partial\tilde{x}} = \frac{\partial\tilde{\sigma}}{\partial\tilde{x}}\left[\frac{2\hat{C}\hat{B}}{\hat{T}}\frac{\partial^2\tilde{z}}{\partial\tilde{x}^2} - \frac{4\hat{C}^2\hat{B}^2}{\hat{T}}\tilde{\sigma} - \frac{2\hat{C}}{\hat{T}}\log\left(\frac{\tilde{\sigma}}{\tilde{\sigma}_s}\right)\right], \tag{4.22}$$

$$\frac{\partial\tilde{\sigma}}{\partial\tilde{t}} = (1+2\hat{C}\hat{B}^2\tilde{\sigma})\frac{\partial^2\tilde{\sigma}}{\partial\tilde{x}^2} + 2\hat{C}\hat{B}^2\left(\frac{\partial\tilde{\sigma}}{\partial\tilde{x}}\right)^2 - \hat{B}\left[\tilde{\sigma}\frac{\partial^4\tilde{z}}{\partial\tilde{x}^4} + \frac{\partial\tilde{\sigma}}{\partial\tilde{x}}\frac{\partial}{\partial\tilde{x}}\left(\frac{\partial^2\tilde{z}}{\partial\tilde{x}^2}\right)\right], \tag{4.23}$$

$$\frac{\partial^4\tilde{z}}{\partial\tilde{x}^4} - 2\hat{C}\hat{B}\frac{\partial^2\tilde{\sigma}}{\partial\tilde{x}^2} - \hat{C}\frac{\partial^2\tilde{z}}{\partial\tilde{x}^2}\left[2\tilde{\sigma}\left(\log\left(\frac{\tilde{\sigma}}{\tilde{\sigma}_s}\right)-1\right) + 2\hat{C}\hat{B}^2\tilde{\sigma}^2\right] = \hat{P} + \hat{T}\tilde{\lambda}\frac{\partial^2\tilde{z}}{\partial\tilde{x}^2}. \tag{4.24}$$

Equations (4.22)–(4.24) are solved numerically using a finite-difference scheme coded in Fortran 90. The tangential momentum balance (4.22), which can be viewed as an equation for the tension $\tilde{\lambda}$, is solved subject to the condition $\tilde{\lambda}(\tilde{x}=1)=1$, whereas the shape equation (4.24) is solved subject to clamped boundary conditions $\tilde{z}=0$ and $\partial\tilde{z}/\partial\tilde{x}=0$ at both ends of the domain $\tilde{x}=-0.5,0.5$.

We first analyzed the evolution of a symmetric patch of protein defined as $\tilde{\sigma}(\tilde{x},\tilde{t}=0) = 1/2[\tanh(20(\tilde{x}+0.1)) - \tanh(20(\tilde{x}-0.1))]$, subject to no-flux boundary conditions on $\tilde{\sigma}$ at the ends of the domain. Results from these simulations are shown in figure 4.1. In response to this protein distribution, the initial configuration of the membrane is bent (see figure 4.1(a) at $t=0$). Over time, $\tilde{\sigma}$ homogenizes as a result of diffusion, and therefore the deflection $\tilde{z}$ decreases. At steady state, the distribution of protein is uniform on the membrane and $\tilde{z}$ is everywhere zero. The time evolution of $\tilde{z}$ at the center of the string, corresponding to the maximum deflection, is shown in figure 4.1(b).

As a second example, we discuss the case where the protein density is initially zero and

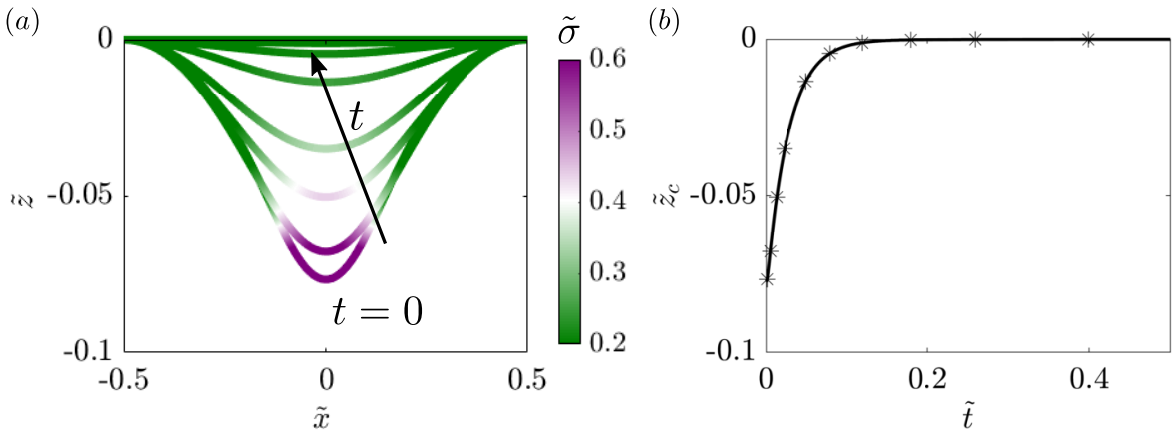

Figure 4.1: Protein density and membrane deformation in one dimension as functions of time, when an initial protein distribution and no-flux boundary conditions are prescribed. (a) Distribution of protein density plotted on the deformed one-dimensional membrane. (b) Time evolution of the maximum membrane deflection $\tilde{z}_c(\tilde{t}) = \tilde{z}(1/2,\tilde{t})$.

a time-dependent protein flux is prescribed at both boundaries as shown in figure 4.2(a). In response to the influx at the boundaries, the membrane deforms out of plane as the protein density increases; see figure 4.2(b). Once the flux returns to zero, diffusion homogenizes the protein, and the membrane height begins to decrease again. This effect is observed clearly by looking at the deformation at the center of the string as a function of time in figure 4.2(c), which closely follows the dynamics of the boundary flux show in figure 4.2(a).

In both examples of figures 4.1 and 4.2, we note that the protein distribution becomes uniform at long times (in the absence of any boundary flux), and as a result the membrane returns to its flat reference shape. At first glance, this result seems counter-intuitive since there is a non-zero density of curvature-inducing proteins on the membrane. But as Chabanon and Rangamani showed previously, for a uniform distribution of proteins with no-flux boundary conditions on the membranes, minimal surfaces are admissible solutions for the membrane geometry [122, 123]. In the case of closed geometries on vesicle, constant mean curvature surfaces are admissible solutions [20, 124, 125, 126]. In the case of interest here, a flat membrane is the admissible solution for the boundary conditions associated with $\tilde{z}$, and a proof of this result is given in Appendix A.1.

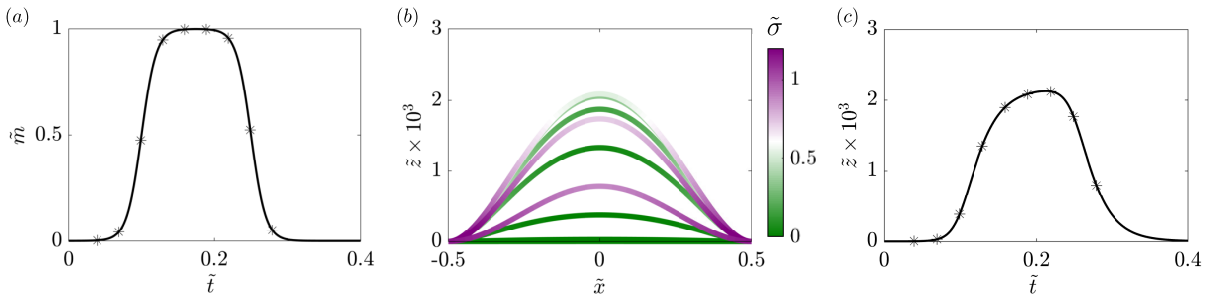

Figure 4.2: Evolution of membrane deformation and protein distribution when an influx of protein is prescribed at both boundaries. (a) Dimensionless boundary protein flux as a function of time. (b) Distribution of protein density plotted on the deformed membrane for $\hat{C} = 2.48 \times 10^{-1}$. ($c$) Time evolution of the maximum membrane deflection $\tilde{z}_c$ for $\hat{C} = 2.48 \times 10^{-1}$. Symbols in panels ($a$) and ($c$) correspond to the times shown in (b).

4.3.3 Two-dimensional simulations

Numerical implementation

We solved the set of governing equations (4.17)–(4.20) in two dimensions inside a square domain using a finite-difference technique that we outline here. Our numerical scheme is second order in space and first order in time. We note that time only appears explicitly in the advection-diffusion equation (4.20) for the protein density: we solve it using a semi-implicit scheme wherein the linear diffusion term is treated implicitly while the nonlinear advective terms and curvature-induced transport terms are treated explicitly. The remaining governing equations are all elliptic in nature and can be recast as a series of Poisson problems as we explain. First, we note that the shape equation (4.19) is biharmonic and can thus be recast into two nested Poisson problems providing the shape $\tilde{z}$ at a particular time step. To solve for the surface tension $\tilde{\lambda}$, we take the divergence of the tangential momentum balance (4.18) and combine it with the continuity equation (4.17) to obtain the Poisson equation

$$\tilde{\nabla}^2 \tilde{\lambda} + f = 0, \tag{4.25}$$

where

$$
\begin{aligned}
f = {} & 4\tilde{H}\tilde{\nabla}^2\tilde{w} - 2\tilde{\boldsymbol{\nabla}}\tilde{\boldsymbol{\nabla}}\tilde{z} : \tilde{\boldsymbol{\nabla}}\tilde{\boldsymbol{\nabla}}\tilde{w} - 8\tilde{\boldsymbol{\nabla}}\tilde{H}\cdot\tilde{\boldsymbol{\nabla}}\tilde{w} \\
& - \frac{2\hat{C}\hat{B}}{\hat{T}}\tilde{\boldsymbol{\nabla}}\tilde{\nabla}^2\tilde{z}\cdot\tilde{\boldsymbol{\nabla}}\tilde{\sigma} - \left[\frac{2\hat{C}\hat{B}}{\hat{T}}\tilde{\nabla}^2\tilde{z} - \frac{2\hat{C}}{\hat{T}}\log\left(\frac{\tilde{\sigma}}{\tilde{\sigma}_s}\right)\right]\tilde{\nabla}^2\tilde{\sigma} \\
& + \frac{2\hat{C}}{\hat{T}}\tilde{\boldsymbol{\nabla}}(\log\tilde{\sigma})\cdot\tilde{\boldsymbol{\nabla}}\tilde{\sigma} + \hat{C}\hat{B}\tilde{\nabla}^2\tilde{\sigma}^2.
\end{aligned}
\tag{4.26}
$$

Note that there is no natural boundary condition on $\tilde{\lambda}$ at the edges of the domain. To approximate an infinite membrane, we first estimate the tension along the four edges using the integral representation

$$
\tilde{\lambda}(\tilde{\boldsymbol{r}}) = 1 + \int_{\Omega} G(\tilde{\boldsymbol{r}} - \tilde{\boldsymbol{r}}_0) f(\tilde{\boldsymbol{r}}_0)\,\mathrm{d}A(\tilde{\boldsymbol{r}}_0), \tag{4.27}
$$

where $G(\boldsymbol{r}) = -\log r/2\pi$ is the 2D Green's function for Poisson's equation in an infinite domain. The calculated tension along the edges is then used as the boundary condition for equation (4.25), where the normal velocity component at the current time step k is calculated as

$$
\tilde{w}^k = \frac{1}{Pe}\frac{\tilde{z}^k - \tilde{z}^{k-1}}{\Delta\tilde{t}}. \tag{4.28}
$$

With knowledge of the membrane tension, the tangential momentum balance (4.18) then provides two modified Poisson problems for the in-plane velocity components. Note that the equations for $\tilde{z}$, $\tilde{\lambda}$ and $\tilde{\boldsymbol{v}}$ are nonlinearly coupled through the various forcing terms in their respective Poisson problems. To remedy this problem, we iterate their solution until every variable converges with a tolerance limit of 5×10^{-7} before proceeding to the next time step. All the results presented below were obtained on a spatial uniform grid of size 201×201 and with a dimensionless time step of $\Delta\tilde{t} = 10^{-4}$. We used Fortran 90 for compiling and running the algorithm. As we show in Appendix A.2, the numerical method was successfully validated by comparison with a Stokes-Neumann formulation [1].

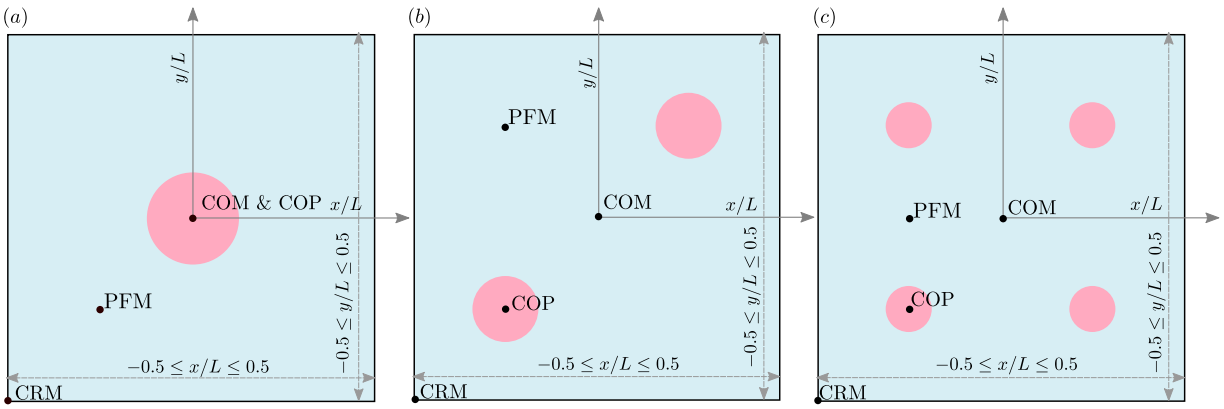

Figure 4.3: System set up and initial condition used in 2D simulations. All 2D simulations are performed for a linearized Monge patch. We simulate the dynamics for three different initial distributions of proteins as shown. The total area fraction of protein is same for the three cases, with proteins covering 10% of the total area. (a) Single patch of protein placed at the center $(0,0)$. (b) Two patches of protein placed at diametrically opposite positions with center locations $(-0.25,-0.25)$ and $(0.25,0.25)$. (c) Four patches of proteins placed at four diagonal positions: $(-0.25,-0.25)$, $(-0.25,0.25)$,$(0.25,-0.25)$ and $(0.25,0.25)$. The following abbreviations are used in subsequent figures to track the system behavior: COM: center of the membrane, COP: center of the patch, CRM: corner of the membrane, and PFM: protein-free membrane.

.

2D simulation results

Using the numerical scheme described above, we solved the linearized two-dimensional governing equations (4.17)–(4.20) for different initial conditions. In all cases, the boundary conditions for the membrane shape were set to $\tilde{z} = 0$ and $\boldsymbol{\nu} \cdot \boldsymbol{\nabla}\tilde{z} = 0$ where $\boldsymbol{\nu}$ is the in-plane normal to the edge of the domain, and no-flux boundary conditions were enforced on the protein distribution. We considered three different initial conditions for the protein density as depicted in figure 4.3, namely: a single circular patch at the center of the domain (figure 4.3(a)), two indentical patches placed at diametrically opposite ends of the domain (figure 4.3(b)), and four patches centered in each quadrant of the domain (figure 4.3(c)). The total mass of protein is the same in all three cases, only the initial spatial distribution is different. For the velocity and tension, we maintain open boundary conditions as noted in § 4.3.3.

We tracked the dynamics of the membrane shape, protein distribution, membrane tension, and velocity for a single patch of proteins corresponding to figure 4.3(a) in figure 4.4. The initial

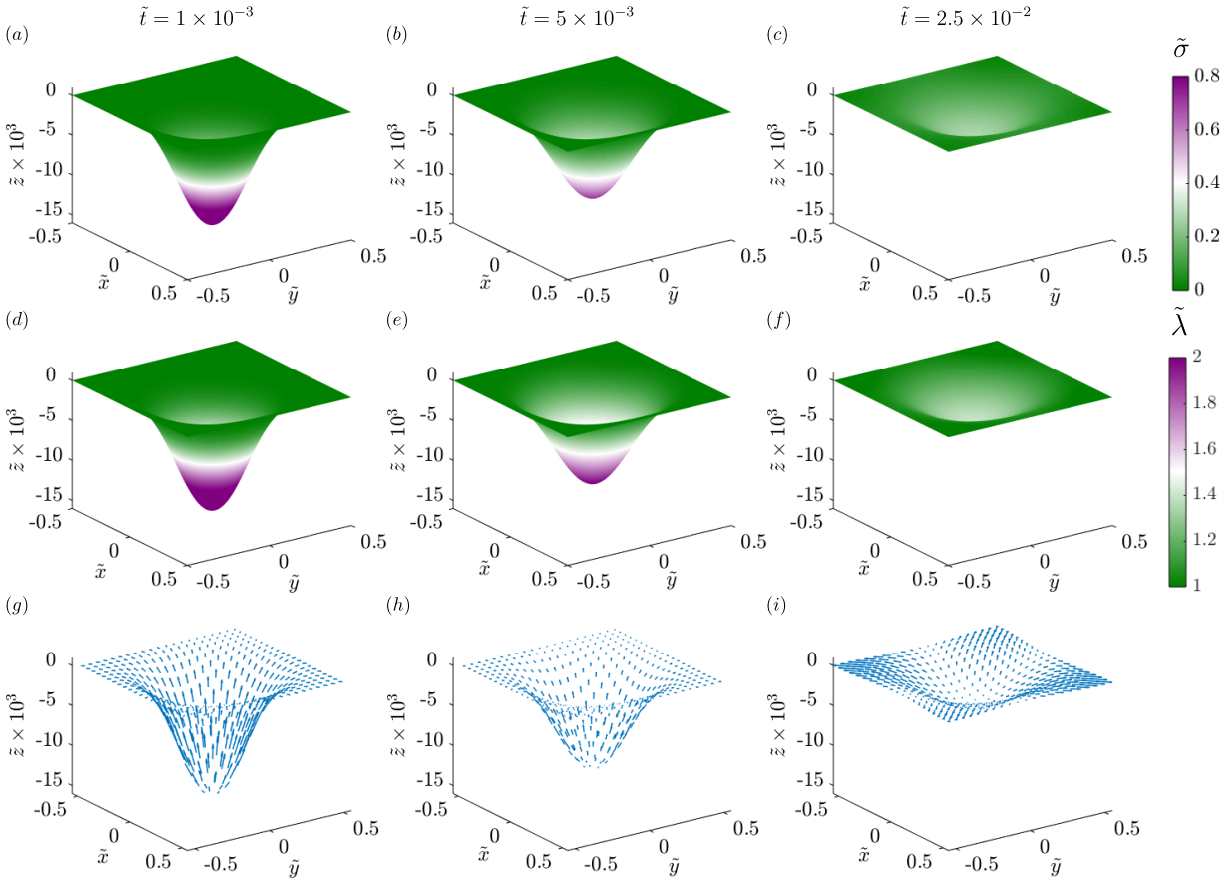

Figure 4.4: Dynamics of the evolution of membrane shape, protein distribution, membrane tension, and tangential velocity field for a single patch of protein at three different times. (*a-c*) Distributions of membrane protein density are shown at dimensionless times 1×10^{-3}, 5×10^{-3}, and 2.5×10^{-2}. (*d-e*) Distributions of membrane tension at the same non-dimensional times. (*g-i*) Tangential velocity fields shown at the same non-dimensional times. Arrows are scaled according to tangential velocity magnitude, with a maximum dimensionless velocity of 4.3×10^{-3}.

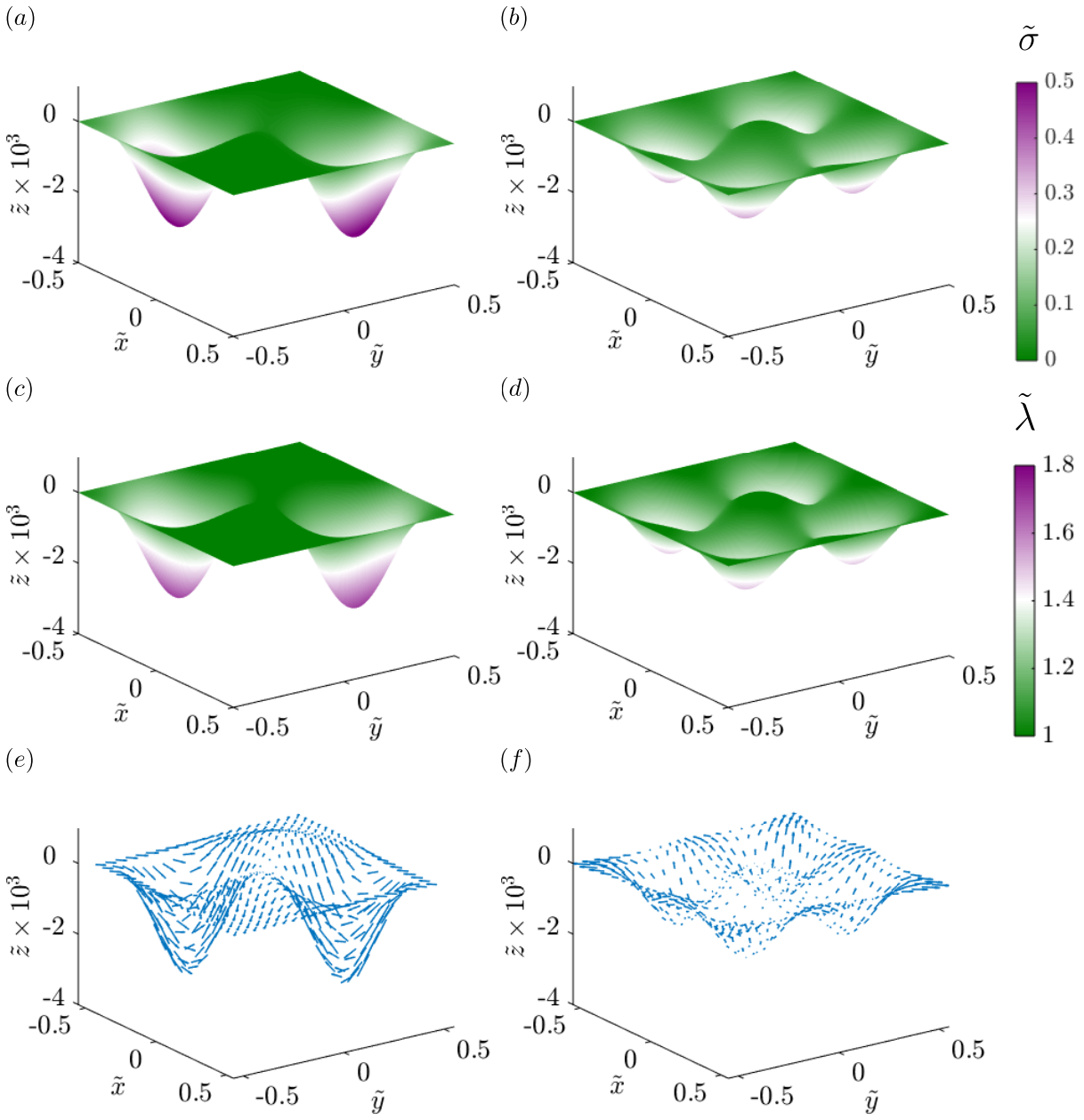

Figure 4.5: Dynamics of the evolution of membrane shape, protein distribution, membrane tension, and tangential velocity field for two and four patches of protein at dimensionless time $\tilde{t} = 5 \times 10^{-3}$. The left column shows the distribution of protein density (a), membrane tension (c), and tangential velocity (e) for two patches of protein. The right column shows the distribution of protein density (b), membrane tension (d), and tangential velocity (f) for four patches of protein. The magnitude of maximum dimensionless tangential velocity is 1.6×10^{-2} in the case of two patches, and 4.1×10^{-3} in the case of four patches.

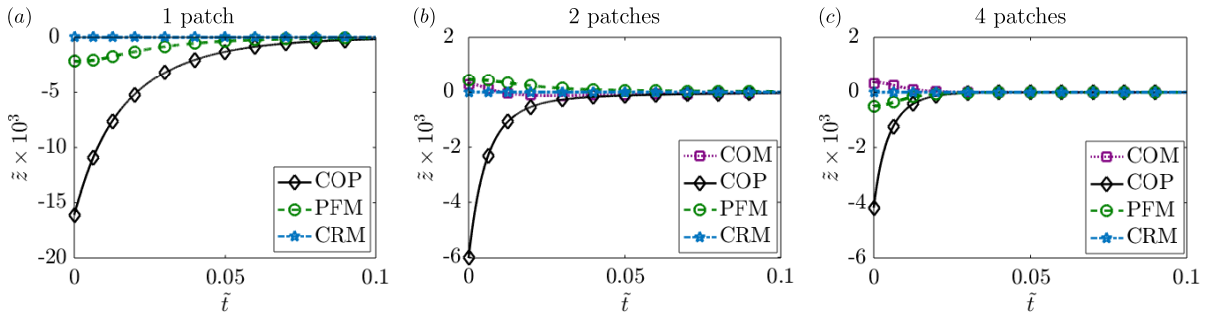

Figure 4.6: Temporal evolution of the membrane deflection at the various locations defined in figure 4.3 for a single patch of protein (*a*), two patches (*b*), and four patches (*c*).

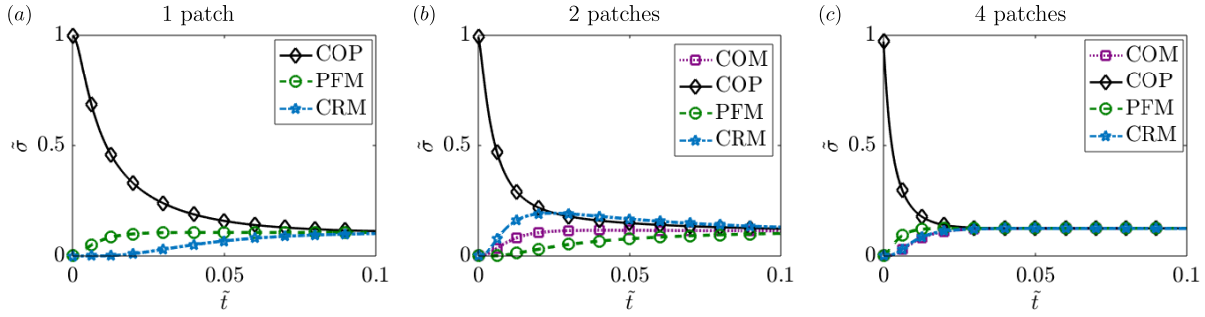

Figure 4.7: Temporal evolution of the protein density at the locations defined in figure 4.3 for a single patch of protein (*a*), two patches (*b*), and four patches (*c*).

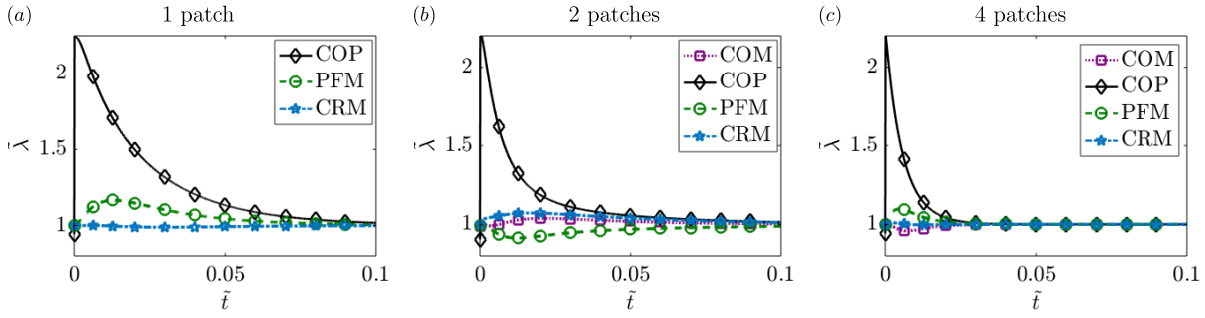

Figure 4.8: Temporal evolution of the membrane tension at the locations defined in figure 4.3 for a single patch of protein (*a*), two patches (*b*), and four patches (*c*).

membrane configuration is bent to accommodate the initial distribution of proteins (figure 4.4(a)), and the membrane tension for this initial distribution is heterogeneous as seen in figure 4.4(d), consistent with our previous results [67, 11]. Over time, the proteins diffuse from the center of the patch across the membrane, tending towards a homogeneous distribution (figure 4.4(b,c)), and this process is accompanied by a reduction in the membrane deflection. The homogenization of proteins results in homogenization of the membrane tension, which approaches its value at infinity (figure 4.4(e,f)). The tangential velocity is directed outward (figure 4.4(g,h,i)), and the dimensionless magnitude of the maximum velocity in figure 4.4(g) is 4.8×10^{-3}. Expectedly, the magnitude of this velocity decreases with time as seen in figure 4.4(h,i).

When the proteins are distributed in two and four patches as shown in figure 4.3(b,c), we found that the overall behavior of the system was quite similar to a single patch with some changes to the dynamics. First, because each patch had a lower density of proteins (half or quarter), the initial deformation was smaller and the protein distribution homogenized faster than in the case of a single patch (figure 4.5(a,b)). Similarly, the typical magnitude of membrane tension variations (figure 4.5(c,d)) and of the tangential velocity field (figure 4.5(e,f)) was also smaller to begin with and the system attained the homogeneous distribution rapidly.

To compare the effects of one, two, and four patches directly, we plotted the membrane deformation (figure 4.6), membrane protein distribution (figure 4.7), and membrane tension distribution (figure 4.8) at different locations for each case. The initial deformation is different for the different cases because of the differences in the local density of proteins. For a single patch, we observed that the maximum deformation occurs at the center of the patch (COP) and it takes a longer time for this deformation to go to zero in the case of a single patch compared to multiple patches (compare figure 4.6(a) to figure 4.6(b,c)). In the case of two and four patches, we also observe a small positive deformation at the center of the membrane (COM) and in the protein-free membrane (PFM). This can be explained by the fact that the continuity conditions of the surface will result in a small but upward displacement in protein-free regions in response to

the large downward displacement in the regions where the proteins are initially present.

Comparing the protein dynamics for one, two, and four patches, we observed that increasing the number of patches decreases the time it takes for the protein distribution to homogenize across the membrane domain (figure 4.7). Thus, although membrane bending and protein distribution are coupled, the distribution of multiple patches weakens the coupling and promotes rapid homogenization of the membrane proteins. While the steady state protein distribution is the same in all cases, the dynamics with which the protein-free regions show an appreciable increase in proteins also depends on the initial distribution of proteins. For example, in the case of a single patch, CRM takes much longer to reach steady state compared to the case of two or four patches. Figure 4.7 shows that for the initial conditions of a single patch and of four patches of protein, $\tilde{\sigma}$ approaches the uniform protein density monotonically. But for the case of two patches, the time evolution of the protein density is not monotonic, and we found the density of protein at the corner of the membrane (CRM) exceeds the density at the center of the patch (COP) for a brief time interval. We investigated this phenomenon further and studied the dependence on intra-membrane flow by varying the Péclet number in § 4.3.3.

Similar dynamics are observed for the membrane tension as well. Figure 4.8 shows that the membrane tension takes a larger time to reach its steady value for the case of one or two patches when compared to four patches (compare figures 4.8(a,b,c)). The initial rise in the membrane tension corresponds to the inviscid response of the membrane to the curvature-inducing protein distribution, while from the next time step onwards tension changes primarily due to viscous effects.

Effect of fluid advection on coupled membrane–protein dynamics

Next, we investigated the effect of fluid advection in the case of two patches by varying the Péclet number *Pe* in figure 4.9. We observed that at the center of the patch (figure 4.9(a)) there was no observable effect on the temporal evolution of the protein density. However, at

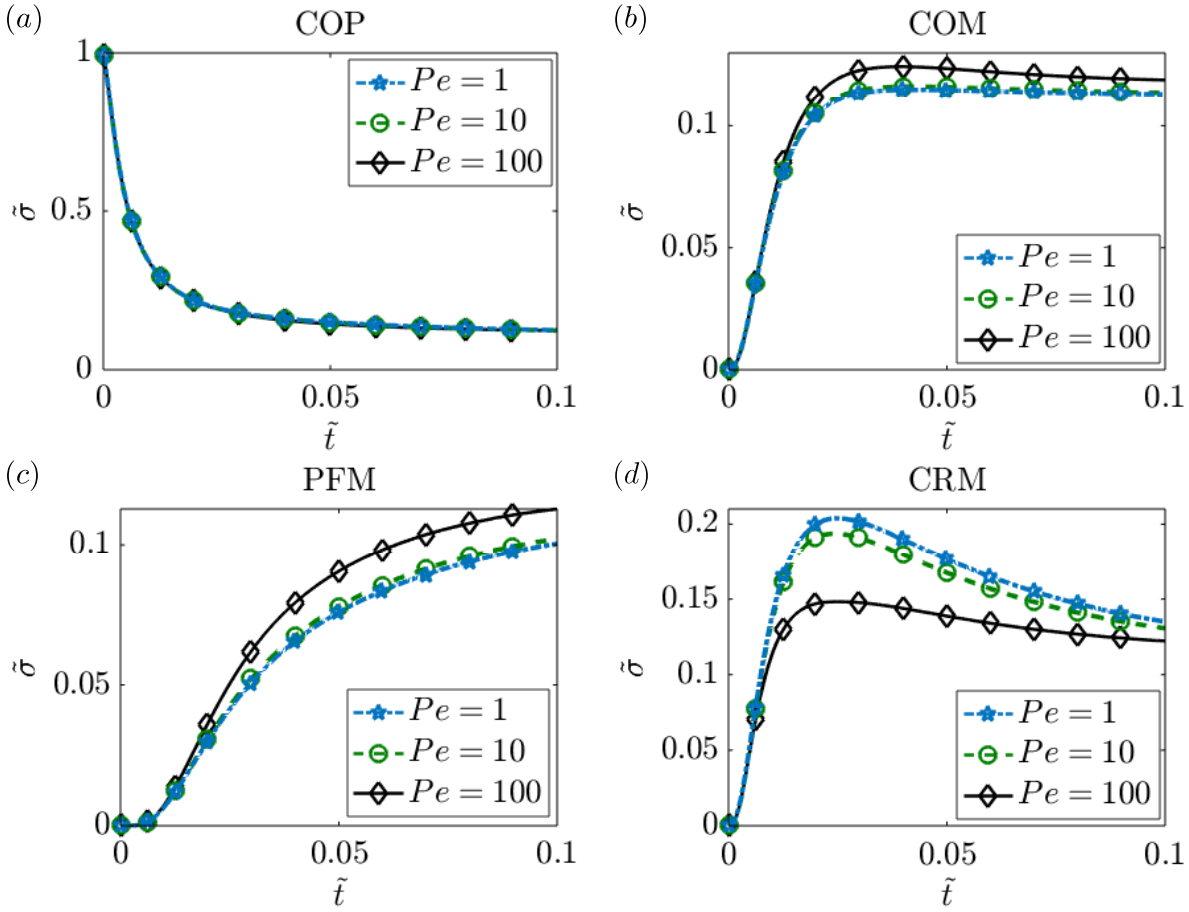

Figure 4.9: Temporal evolution of local protein density for different values of the Péclet number in the case of two patches of protein. The protein density is measured at the four locations defined in figure 4.3: COM (*a*), COP (*b*), PFM (*c*) and CRM (*d*).

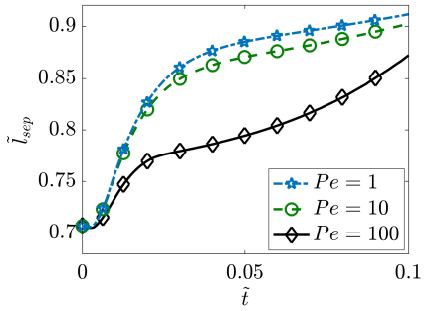

Figure 4.10: Evolution of the separation distance between the centroids of the protein patches in the case of two patches and for three different values of the Péclet number.

the center of the membrane (figure 4.9(b)) and in the protein-free membrane (figure 4.9(c)), we observed that increasing Péclet number had a small effect on the dynamics of the protein density, particularly at long times.

The effect of increasing the Péclet number was most dramatic at the corner of the membrane (figure 4.9(d)), where the initial rise in the protein density was found to be similar for all three values of Pe, but the increase resulted in a higher value for lower Pe. Eventually, $\tilde{\sigma}$ at the corner decreases towards the mean value of $\tilde{\sigma}$ over time. Thus, the coupling between lipid flow and protein diffusion seems to have a larger impact on transport in the regions that are initially protein-free.

To further investigate the role of convective transport, we tracked the separation distance $\tilde{l}_{sep}$ between the centers of mass of two effective patches (l_{sep}) as a function of time in figure 4.10. The center of mass of a patch is formally defined as

$$\tilde{\boldsymbol{r}}_c = \frac{\int_\Omega \tilde{\boldsymbol{r}}(\tilde{\sigma}-\tilde{\sigma}_m)\mathcal{H}(\tilde{\sigma}-\tilde{\sigma}_m)\,\mathrm{d}a}{\int_\Omega (\tilde{\sigma}-\tilde{\sigma}_m)\mathcal{H}(\tilde{\sigma}-\tilde{\sigma}_m)\,\mathrm{d}a} \quad \text{with,} \quad \tilde{\sigma}_m = \int_\Omega \tilde{\sigma}\,\mathrm{d}a, \tag{4.29}$$

where the effective extent of the patch is defined using the Heaviside function $\mathcal{H}$ as the area where protein density exceeds its mean value. We observed that $\tilde{l}_{sep}$ increases with time and decreases with increasing Péclet number (figure 4.10). This can be explained from the velocity profile for two patches in figure 4.5(e). The direction of the velocity is towards the center of the membrane in the area where the patch is located. Therefore, the advective transport due to the lipid tends to weaken the separation otherwise caused by diffusion. Since the effect of flow increases with increasing Pe, the separation of the two patches slows down for higher values Péclet number as shown in figure 4.10. This also explains the decrease of density of the protein at the corner of the membrane (CRM) and the increase of the protein density at the initial protein-free area (PFM) and center of the membrane (COM) with higher value of Pe as found in figure 4.9.

We can further understand the dynamics of the separation distance between the two

patches by considering the diffusion of a protein patch in one triangular half domain of lipid. This triangle is bounded by two of the domain boundaries and by the diagonal of the square domain that passes in between the two patches. The diagonal line is also a line of symmetry, and thus behaves as an effective no-flux boundary for the triangular half of the domain. Therefore, each triangular half-domain is subject to the no-flux condition on its three sides. In this half domain, the semicircular half patch of protein facing the corner of the membrane (CRM) diffuses to a smaller area compared to the other semicircle that faces the center of the membrane (COM). This results in an effectively larger protein gradient towards CRM. Therefore, the protein density shifts towards the protein-free corner and results in an effective shift of the patches towards the corners of the membrane.

4.4 Axisymmetric membranes

In the previous section, we focused on small deformations from a flat plane. However, membranes are known to undergo large deformations including bud-like shapes in the presence of proteins [11, 127, 128]. Here, we illustrate the interaction between membrane bending and protein diffusion for membrane buds. For these simulations, we assume that the membrane is rotationally symmetric and recast the governing equations of §4.2.2 in an axisymmetic framework.

4.4.1 Governing equations in axisymmetric coordinates

We represent tangential velocity vector in polar coordinates as

$$\boldsymbol{v} = v^s \boldsymbol{e}_s + v^\theta \boldsymbol{e}_\theta. \tag{4.30}$$

For an axisymmetric geometry as depicted in figure 4.11(a), we assume $\partial()/\partial\theta = 0$ and $v^\theta = 0$ [62]. Thus, we parametrize the geometry as

$$\boldsymbol{r}(s,\theta,t) = r(s,t)\boldsymbol{e}_r + z(s,t)\boldsymbol{k}, \tag{4.31}$$

where the unit vectors $(\boldsymbol{e}_r, \boldsymbol{e}_\theta, \boldsymbol{k})$ are a set of orthonormal basis vectors and s is the arclength measured from the axis of symmetry. The tangent and normal vectors are given by

$$\boldsymbol{a}_s = \cos\psi\boldsymbol{e}_r + \sin\psi\boldsymbol{e}_\theta, \quad \boldsymbol{a}_\theta = r\boldsymbol{e}_\theta, \quad \boldsymbol{n} = -\sin\psi\boldsymbol{e}_r + \cos\psi\boldsymbol{e}_\theta, \tag{4.32}$$

where ψ is the angle made by the tangent $\boldsymbol{a}_s$ with the radial unit vector $\boldsymbol{e}_r$. The corresponding surface metric ($a_{\alpha\beta}$) and curvature metric ($b_{\alpha\beta}$) are

$$a_{\alpha\beta} = \begin{bmatrix} 1 & 0 \\ 0 & r^2 \end{bmatrix}, \quad b_{\alpha\beta} = \begin{bmatrix} \psi_{,s} & 0 \\ 0 & r\sin\psi \end{bmatrix}. \tag{4.33}$$

Using these expressions, the incompressibility constraint becomes

$$\frac{1}{r}\frac{\partial(rv^s)}{\partial s} = 2wH. \tag{4.34}$$

The governing equation for surface pressure is

$$\begin{aligned} \frac{\partial\lambda}{\partial s} - 4\nu w\frac{\partial H}{\partial s} + 2\nu\left(2\frac{\partial wH}{\partial s} + Kv_s - \frac{\partial w}{\partial s}\frac{\partial\psi}{\partial s}\right) \\ = -\frac{\partial\sigma}{\partial s}\left[k_BT\log\left(\frac{\sigma}{\sigma_s}\right) - 2k\ell(H-\ell\sigma)\right], \end{aligned} \tag{4.35}$$

and the shape equation expressing the normal momentum balance is given by

$$\begin{aligned} k\frac{1}{r}\frac{\partial}{\partial s}\left(r\frac{\partial(H-\ell\sigma)}{\partial s}\right)+2k(H-\ell\sigma)(2H^2-K) \\ -2H\left[k_BT\sigma\left(\log\left(\frac{\sigma}{\sigma_s}\right)-1\right)+k(H-\ell\sigma)^2\right] \\ -2\nu\left[\frac{\partial\psi}{\partial s}\frac{\partial v^s}{\partial s}+\frac{\sin\psi\cos\psi v^s}{r^2}-w(4H^2-2K)\right]=p+2\lambda H. \end{aligned} \tag{4.36}$$

The transport equation for the protein density simplifies to

$$\begin{aligned} \frac{\partial\sigma}{\partial t}+\frac{\partial(\sigma v^s)}{\partial s}=D\frac{1}{r}\frac{\partial}{\partial s}\left(r\frac{\partial\sigma}{\partial s}\right)-2k\ell\left[\sigma\frac{1}{r}\frac{\partial}{\partial s}\left(r\frac{\partial H}{\partial s}\right)+\left(\frac{\partial H}{\partial s}\right)^2\right] \\ +2k\ell^2\left[\sigma\frac{1}{r}\frac{\partial}{\partial s}\left(r\frac{\partial\sigma}{\partial s}\right)+\left(\frac{\partial\sigma}{\partial s}\right)^2\right]. \end{aligned} \tag{4.37}$$

Finally, the kinematic relation for the normal velocity is given by

$$w=\boldsymbol{n}\cdot\frac{\partial\boldsymbol{r}}{\partial t}. \tag{4.38}$$

4.4.2 Non-dimensionalization

We non-dimensionalize the system of equations using a reference length scale L (which we assumed to be 20 nm) such that the radius of the domain is $20L$, with all other scales remaining

the same as in §4.3.1. The dimensionless governing equations are:

$$\frac{1}{\tilde{r}}\frac{\partial(\tilde{r}\tilde{v}^s)}{\partial\tilde{s}} = 2\tilde{w}\tilde{H}, \tag{4.39}$$

$$\begin{aligned}\frac{\partial\tilde{\lambda}}{\partial\tilde{s}} - 4\tilde{w}\frac{\partial\tilde{H}}{\partial\tilde{s}} + 2\left(2\frac{\partial\tilde{w}\tilde{H}}{\partial\tilde{s}} + K\tilde{v}_s - \frac{\partial\tilde{w}}{\partial\tilde{s}}\frac{\partial\psi}{\partial\tilde{s}}\right) = \\ -\frac{\partial\tilde{\sigma}}{\partial\tilde{s}}\left[\frac{2\hat{C}}{\hat{T}}\log\left(\frac{\tilde{\sigma}}{\tilde{\sigma}_s}\right) - \frac{4\hat{C}\hat{B}}{\hat{T}}(\tilde{H} - \hat{C}\hat{B}\tilde{\sigma})\right],\end{aligned} \tag{4.40}$$

$$\begin{aligned}\frac{1}{\tilde{r}}\frac{\partial}{\partial\tilde{s}}\left(\tilde{r}\frac{\partial(\tilde{H} - \hat{C}\hat{B}\tilde{\sigma})}{\partial\tilde{s}}\right) + 2(\tilde{H} - \hat{C}\hat{B}\tilde{\sigma})(2\tilde{H}^2 - K) \\ -2\tilde{H}\left[\hat{C}\tilde{\sigma}\left(\log\left(\frac{\tilde{\sigma}}{\tilde{\sigma}_s}\right) - 1\right) + (\tilde{H} - \hat{C}\hat{B}\tilde{\sigma})^2\right] \\ -\hat{T}\left[\frac{\partial\psi}{\partial\tilde{s}}\frac{\partial v^s}{\partial\tilde{s}} + \frac{\sin\psi\cos\psi\tilde{v}^s}{\tilde{r}^2} - \tilde{w}(4\tilde{H}^2 - 2\tilde{K})\right] = \frac{\hat{P}}{2} + \hat{T}\tilde{\lambda}\tilde{H},\end{aligned} \tag{4.41}$$

$$\begin{aligned}\frac{\partial\tilde{\sigma}}{\partial\tilde{t}} + Pe\frac{\partial(v^\alpha\tilde{\sigma})}{\partial\tilde{s}} = \frac{1}{\tilde{r}}\frac{\partial}{\partial\tilde{s}}\left(\tilde{r}\frac{\partial\tilde{\sigma}}{\partial\tilde{s}}\right) \\ -2\hat{B}\left[\frac{\partial(\tilde{H} - \hat{C}\hat{B}\tilde{\sigma})}{\partial\tilde{s}}\frac{\partial\tilde{\sigma}}{\partial\tilde{s}} + \tilde{\sigma}\frac{1}{\tilde{r}}\frac{\partial}{\partial\tilde{s}}\left(\tilde{r}\frac{\partial(\tilde{H} - \hat{C}\hat{B}\tilde{\sigma})}{\partial\tilde{s}}\right)\right],\end{aligned} \tag{4.42}$$

$$\tilde{w} = \frac{1}{Pe}\boldsymbol{n}\cdot\frac{\partial\tilde{\boldsymbol{r}}}{\partial\tilde{t}}. \tag{4.43}$$

4.4.3 Numerical implementation

The system of dimensionless governing equations (4.40)–(4.43) was solved using finite difference methods using the arclength parametrization [129]. In these simulations, the total area of the domain was kept constant. This was achieved by first dividing the initial arclength into $N-1$ discrete elements, which gives N grid points on which the equations were solved. We then calculated the area of each of the $N-1$ discrete area elements. At each time step, the local radius and arclength is back-calculated by keeping the area of these discrete elements constant in the following way:

$$r_{i+1}^2 = r_i^2 + 2\mathrm{d}A_i\cos\psi/\pi, \tag{4.44}$$

and

$$s_{i+1} = s_i + \mathrm{d}s_i = s_i + \frac{r_{i+1} - r_i}{\cos\psi}, \tag{4.45}$$

with

$$r_1 = s_1 = 0. \tag{4.46}$$

To solve the set of governing equations (4.40)–(4.43), we first obtained the membrane tension $\tilde{\lambda}$ by integrating equation (4.40) backward starting from the edge of the membrane where the boundary condition $\tilde{\lambda} = 1$ is enforced. We then consider the shape equation (4.41) where the first term can be written as $(1/\tilde{r})(\partial\tilde{L}/\partial\tilde{s})$ in terms of the normal bending stress [111]

$$\frac{\tilde{L}}{\tilde{r}} = \frac{\partial}{\partial\tilde{s}}\left[\frac{1}{2}\left(\psi_s + \frac{\sin\psi}{\tilde{r}}\right) - \hat{C}\hat{B}\tilde{\sigma}\right]. \tag{4.47}$$

The modified shape equation is solved for $\tilde{L}$ with boundary condition $\tilde{L} = 0$ at the center of the domain corresponding to the case where there is no pulling force acting on the center of the membrane. When doing do, other shape-dependent terms in the shape equation are treated explicitly, and iterations are performed until convergence. Equation (4.47) is then integrated for ψ at every point with the boundary condition $\psi = 0$ at the center of the membrane and at the boundary. Having determined ψ, the radial $\tilde{r}$ and the vertical $\tilde{z}$ position of the membrane are calculated. The continuity equation (4.39) is then integrated to obtain the value of tangential velocity $\tilde{v}^s$. Finally, the diffusion equation (4.42) is marched in time to update the protein distribution $\tilde{\sigma}$ across the membrane as described in §4.3.3.

4.4.4 Numerical results

We solved the dimensionless governing equations (4.39)–(4.43) for the solution domain and boundary conditions shown in figure 4.11(a). The domain is initialized with a protein distribution as shown in figure 4.11(b) such that the initial shape of the membrane is a bud,

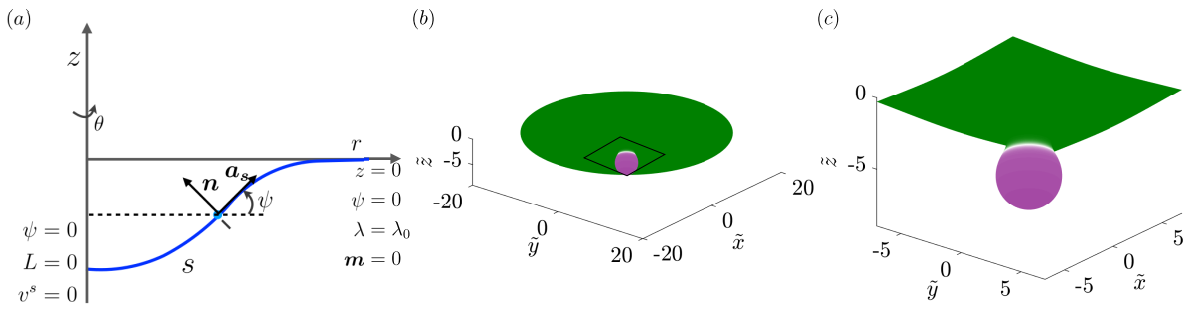

Figure 4.11: Parametrization of an axisymmetric membrane and bud-shaped initial condition: (*a*) Parametrization and boundary conditions for an axisymmetric membrane. (*b*) Solution domain showing the initial condition, where a circular patch of curvature-inducing protein (shown in purple) induces a bud-shaped deformation. (*c*) A magnified view of the domain shown in (*a*).

similar to those observed in membrane fission and fusion processes [130, 131]. This initial shape is obtained by solving equations (4.34)–(4.38) for an inviscid membrane. The black square highlights the curved bud region shown as a zoomed-in image in figure 4.11(*c*), and all simulation results are shown in this zoomed-in region.

We make no simplifying assumptions about linear deformations or curvature regimes in the axisymmetric case, which allows us to explore the nonlinear coupling between membrane curvature, protein diffusion, and lipid flow in full detail. We conducted the following simulations to map this relationship: (a) Diffusion of proteins on curved surfaces with no coupling between protein distribution and spontaneous curvature, so as to study the effect of surface curvature on protein diffusion, and (b) coupled diffusion of proteins and induction of spontaneous curvature.

We first investigate the diffusion of proteins on curved surfaces by simulating the scenario where there are two types of proteins on the membrane: the first protein does not induce any curvature ($C_1 = 0$) but can diffuse along the membrane ($D_1 = 0.1\,\mu\text{m}^2\,\text{s}^{-1}$), whereas the second protein is curvature-inducing (with spontaneous curvature $C_2 = 0.02\,\text{nm}^{-1}$) but immobile ($D_2 = 0$). Figure 4.12(*a*-*c*) shows the initial shapes of the three surfaces for increasing values of the spontaneous curvature. Figure 4.12(*a*) shows the case of a flat membrane ($C_2 = 0$) and captures diffusion of a protein with no spontaneous curvature ($\ell = 0$) similar to Fickian diffusion on a

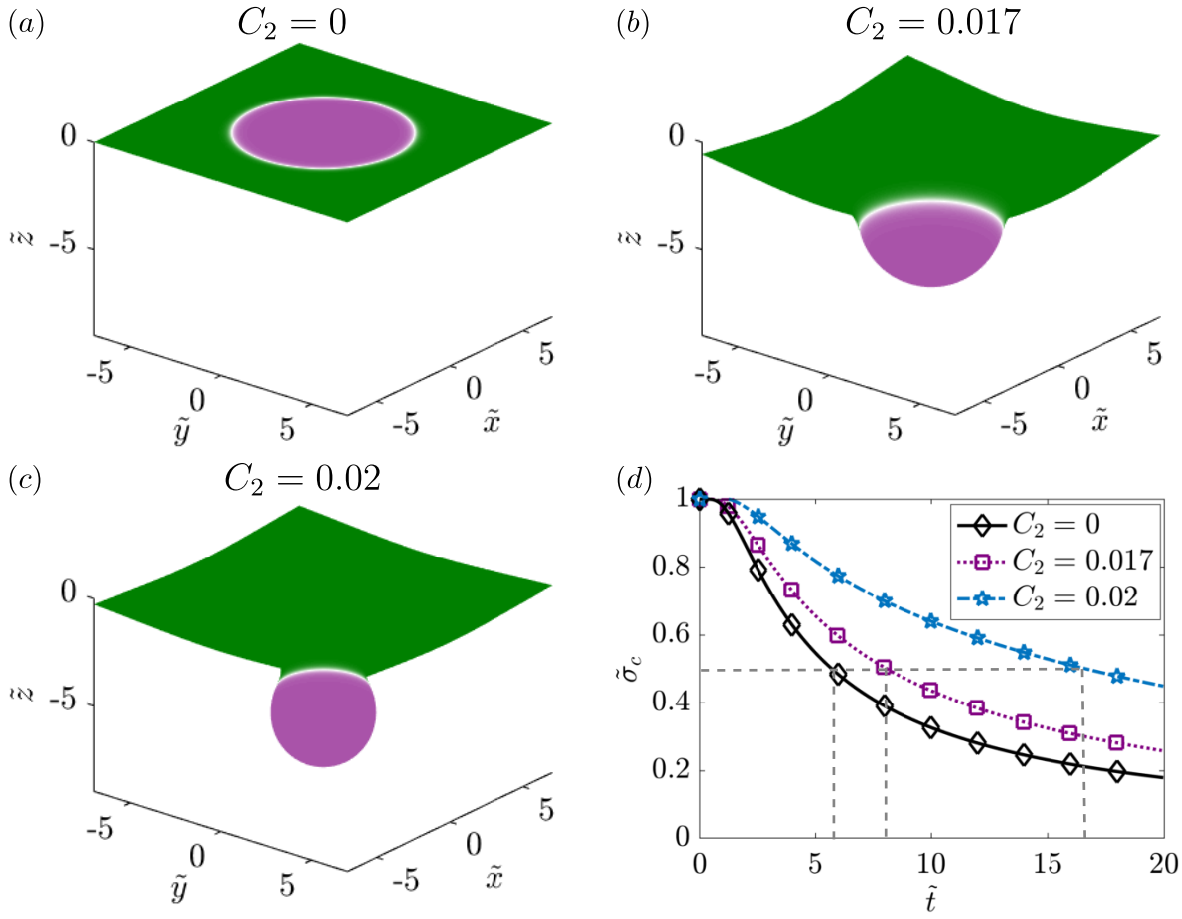

Figure 4.12: Dependence of surface curvature C_2 on the diffusion of the protein that does not induce curvature ($\ell_1 = 0$). Initial protein distribution on: (*a*) a flat membrane ($C_2 = 0$), (*b*) a membrane with preexisting curvature $C_2 = 0.015\,\mathrm{nm}^{-1}$, (*c*) a membrane with preexisting curvature $C_2 = 0.02\,\mathrm{nm}^{-1}$. (*d*) Temporal dynamics of protein density at the center of the membrane for the three different configurations. The dashed lines highlight the time it takes for $\tilde{\sigma}_c$ to decrease from 1 to 0.5.

flat plane. When the membrane is moderately curved in figure 4.12(*b*) or heavily curved in figure 4.12(*c*), diffusion from the center of the membrane takes a longer time compared to Fickian diffusion on a flat plane (compare purple and blue lines with the black line in figure 4.12(*d*)). The time required for proteins to diffuse away from the center to the flat regions of the membrane increases with the preexisting curvature. We compared the time taken for $\tilde{\sigma}_c$ to decrease from 1 to 0.5 and find that it increases nonlinearly with C_2, as shown by the dashed lines in figure 4.12(*d*). This result clearly shows that the curvature of the surface alters the timescale of surface diffusion in a nonlinear fashion.

Next, we simulated the full coupled system where the same protein protein induces spontaneous curvature and is free to diffuse in the plane of the membrane. Figure 4.13 tracks the evolution of the membrane shape and protein distribution as the initial aggregate of curvature-inducing protein diffuses over time. At the start of the simulation, the membrane forms an Ω-shaped bud with a narrow neck (figure 4.13(*b*)). The equilibrium solution of this system is a flat plane with uniform protein distribution. Upon initiation of the simulation, the membrane neck widens and forms a U-shaped neck. This widening of the neck is accompanied by a brief increase in the height of the tip of the membrane and a brief accumulation of proteins towards the bud (figure 4.13(*b,c*)). Once the U-shaped neck is formed, the direction of transport reverses and proteins diffuse rapidly away from the center of the bud with a corresponding flattening of the membrane (figure 4.13*d*). The value of the membrane tension, which is initially larger at the center, eventually reduces to its boundary value as the protein density becomes uniform (figure 4.13(*e,f,g*)). The flow profile follows the membrane deformation and the protein distribution over time. Initially, the tangential velocity is directed towards the center causing advection of the protein towards the tip (compare figure 4.13(*h*) and (*i*)). At later times, as the protein diffuses out and the membrane begins to flatten, the flow direction reverses direction, consistent with the continuity equation (figure 4.13(*j*)).

Figure 4.14 shows the change in the displacement (*a*), protein density (*b*), and membrane

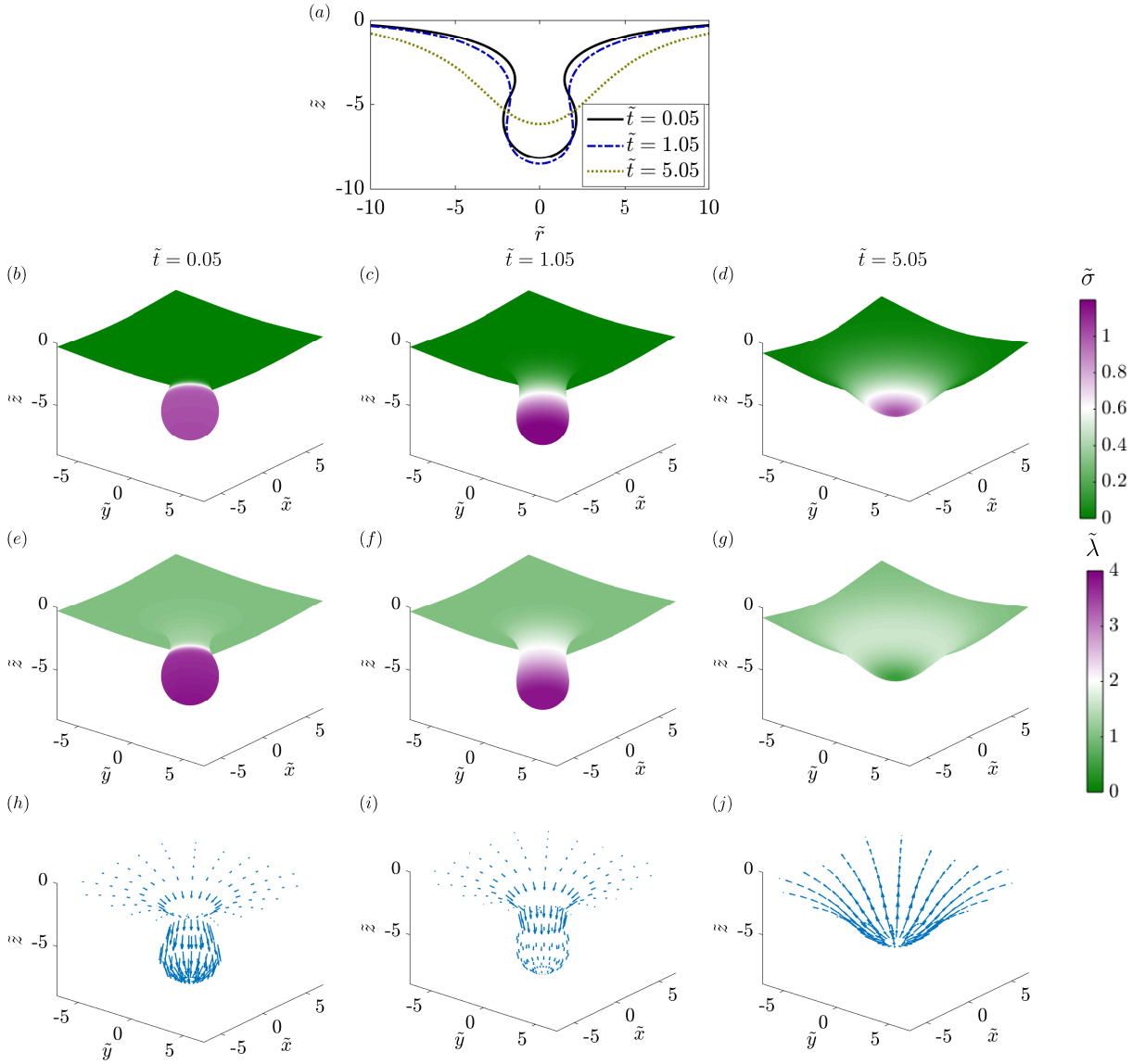

Figure 4.13: Dynamics of the evolution of membrane shape, protein distribution, membrane tension, and tangential velocity field at three different times. (*a*) Superposed membrane shapes at three different times. (*b-d*) Distributions of membrane protein density are shown at dimensionless times 0.05, 1.05, and 5.05. (*e-g*) Distributions of membrane tension at the same non-dimensional times. (*h-j*) Tangential velocity fields shown at the same non-dimensional times. Arrows are scaled according to tangential velocity magnitude, with a maximum dimensionless velocity of 8.4×10^{-2}.

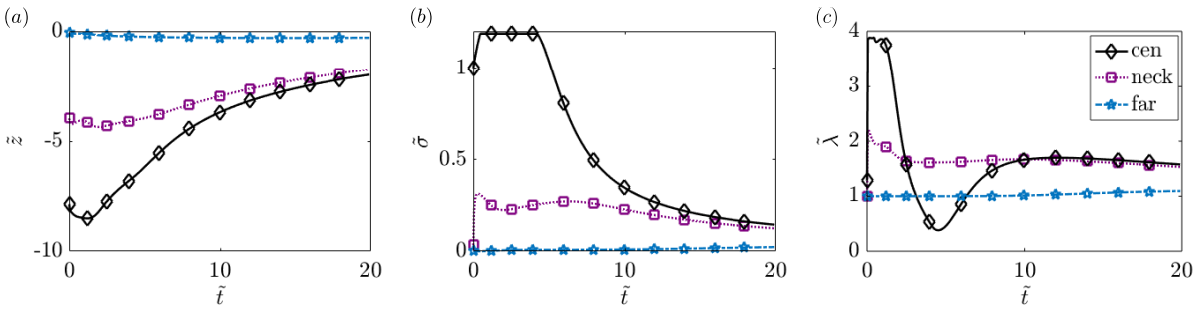

Figure 4.14: Temporal evolution of: (*a*) vertical displacement, (*b*) protein density and (*c*) membrane tension at three different locations: center of the membrane (cen), neck of the bud (neck) (dimensionless arclength distance from the center is 4.2), and far from the bud (far) (dimensionless arclength distance from the center is 14.3).

tension (*c*) at three different locations: center of the membrane (center), neck of the bud (neck), and a location far from the bud (far). We observe that the displacement at the center of the membrane and at the neck first increases and then decreases consistent with the initial widening of the neck (figure 4.14(*a*)). No observable change in deformation was noted far from the bud. The protein density increases at the center before decreasing over time (figure 4.14(*b*)). We enforced a maximum value of 1.25 for $\tilde{\sigma}$ in the simulations in place of introducing a surface saturation density of proteins on the membrane; this can be interpreted as a simple model for protein crowding. The protein density at the neck remains more or less uniform for a long time, consistent with the diffusion of proteins away from the bud towards the flat membrane. The membrane tension at the center initially decreases and then increases (figure 4.14(*c*)). Recall that the membrane tension is simply the negative of the surface pressure [55, 64, 67]. The drop in the membrane tension corresponds to the change in the direction of the viscous pressure drop that results from the change in direction of the velocity field. Membrane tension increases further as the contribution from the viscous component becomes weak over time and the elastic component dominates. This is consistent with the nature of the membrane tension for the linear Monge case (figure 4.8(*a*)).

Finally, we varied the extent of the curvature induced by the protein by varying the characteristic protein size ℓ (figure 4.15). For a small value of $\ell = 1\,\text{nm}$ such that the initial

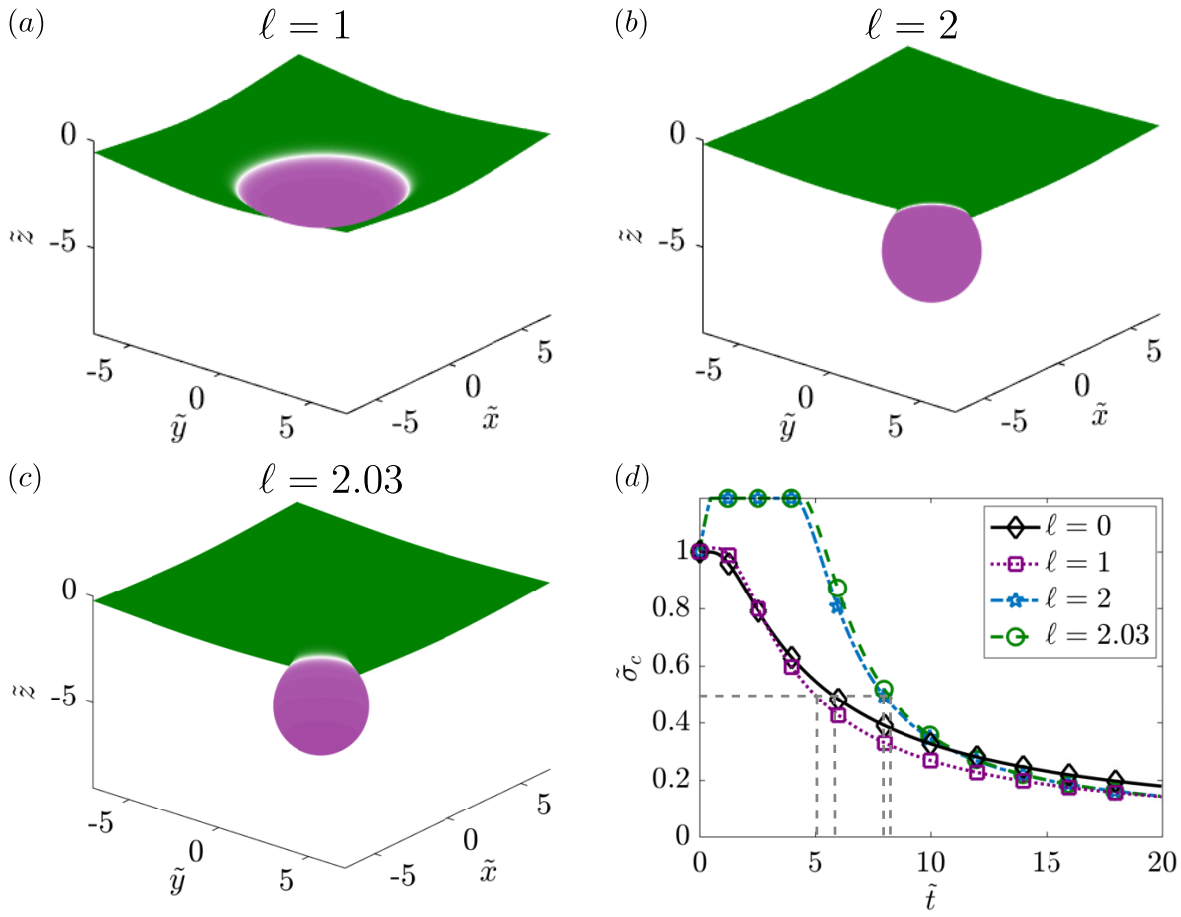

Figure 4.15: Coupling of protein curvature inducing effect and diffusion. Initial distribution of the protein for (*a*) $\ell = 1\,\text{nm}$, (*b*) $\ell = 2\,\text{nm}$, and (*c*) $\ell = 2.03\,\text{nm}$. (*d*) Temporal dynamics of the density of the protein at the center of the membrane for the three different configurations. The dashed lines highlight the time it takes for $\tilde{\sigma}_c$ to decrease from 1 to 0.5.

curvature was a small deviation from the flat plane (figure 4.15(a)), protein diffusion flattens out the membrane similar to the results observed in the Monge parametrization (figure 4.7(a)) and for diffusion on a flat surface (figure 4.12(d)) corresponding to the case where $\ell = 0$. However, increasing ℓ to 2 nm and 2.03 nm in figure 4.15(b,c) such that the initial shape is a well-defined bud leads to altered temporal dynamics. We compared the time required for $\tilde{\sigma}_c$ to decrease from 1 to 0.5 for different values of ℓ. Interestingly, we find that low curvatures promote slightly faster diffusion of protein from the center of the domain as compared to flat surfaces (compare $\ell = 0$ nm to $\ell = 1$ nm). For high values of ℓ, this time scale increases but the flattening of the membrane coupled with diffusion results in similar long-time dynamics, which is different from the case of fixed surface curvature. Thus, we find that the coupling between membrane bending, protein diffusion, and lipid flow reveals an intricate and a somewhat counterintuitive relationship, with nonlinear dependencies between protein diffusion timescales and membrane curvature.

4.5 Discussion

In this work, we have derived and analyzed the governing equations for the protein-induced deformation of a lipid membrane coupled with protein diffusion and in-plane viscous flow of the lipids. The coupling between diffusion and lipid flow completes the description of the key transport phenomena involved in lipid membranes. We conducted simulations in 1D and 2D (linearized Monge and axisymmetry) and further quantified the relationship between membrane bending and protein diffusion. The major conclusions from our study are that lipid flow and membrane protein diffusion, when coupled, can alter the dynamics of membrane protein distribution at different locations. We find that as the protein diffuses from an initial locally concentrated patch in the small deformation regime, the membrane deformation decreases and these dynamics are also related to the diffusion coefficient of proteins on the membrane. The flow of lipids also seems to induce a separation dynamics that depends on the Péclet number of the

system when multiple patches are present.

In the case of buds, because of the strong coupling between protein diffusion and membrane bending, certain nonlinearities are observed. First, we note that the diffusion of protein at the center of a bud depends on the extent of curvature induced by the protein. Second, we note that in buds, proteins first tend to move towards the center of the bud to enable widening of the neck and then diffuse away from the center. These findings have implications for membrane flattening after fusion in cellular processes such as exocytosis [132] and membrane repair [133].

Previously, we elaborated on the need for coupling between the viscous and elastic effects for the calculation of the Lagrange multiplier associated with the incompressibility constraint of the membrane [67, 64]. Here, we build on that framework to include protein diffusion. The coupled interaction between elasticity, diffusion, and viscous flow now fully describes the equations associated with the Lagrange multiplier λ, reinforcing its interpretation as a surface pressure [115, 64]. We note that further efforts are needed in simulation technologies such that complex geometries can be simulated [134, 135, 136, 137].

There have been many studies focused on modeling membrane-protein interactions [138, 13]. Here, we show that coupling the viscous flow of lipids on the membrane is important for modulating the dynamics of the system and fully describing interfacial transport phenomena. Future efforts will focus on adsorption of proteins from the bulk [139, 140] and phase separation of proteins to identify the coupling between lipid flow and chemical energies associated with these processes on an elastic membrane. Such theoretical developments not only have implications for our understanding of biological membranes, but also have the potential to impact curvature-driven, directed assembly in colloids and liquid crystals suspended in fluids, and particle interactions at interfaces between immiscible fluids and soft materials, enabling directed design and engineering of the next-generation of reconfigurable systems in soft matter [141, 142].

4.6 Acknowledgments

I would like to acknowledge my co-authors: Prof. Padmini Rangamani and Prof. David Saintillan. This chapter is primarily based on the published material appeared in the Journal of Fluid Mechanics (2020) authored by Arijit Mahapatra, David Saintillan, and Padmini Rangamani. The dissertation author was the primary author of the work. I would like to thank Prof. David Steigmann for initial discussions on the model development.

Chapter 5

Protein aggregation and curvature-driven feedback

5.1 Introduction

In Chapter 2, we developed a model that couples the in-plane flow of lipids and diffusion of proteins with the out-of-plane bending of the membrane. Building on this work, here, we focus on the role of explicit aggregation of proteins on the surface of the membrane in the presence of membrane bending and diffusion. The aggregation of particles in solvents is a well-studied theoretical problem. Flory [143] and Huggins [144] presented a theoretical formulation for a polymer chain in solution and established the conditions that can lead to its phase separation from the solvent. In binary alloy systems, there has been significant progress on the modeling of the phase transition mechanisms starting from the fundamental Ginzburg-Landau energy [145] that models the interaction energy between the phases as an algebraic expansion in the area fraction of the binary phases around a reference value. A continuum phase-field model of binary fluids is of interest from an engineering point of view to design complex fluids [146, 147]. Additionally, there are a number of studies that considered the effect of surface tension in the phase separation of

solid solutions with an elastic field as a function of concentration field of solute [148, 149, 150].

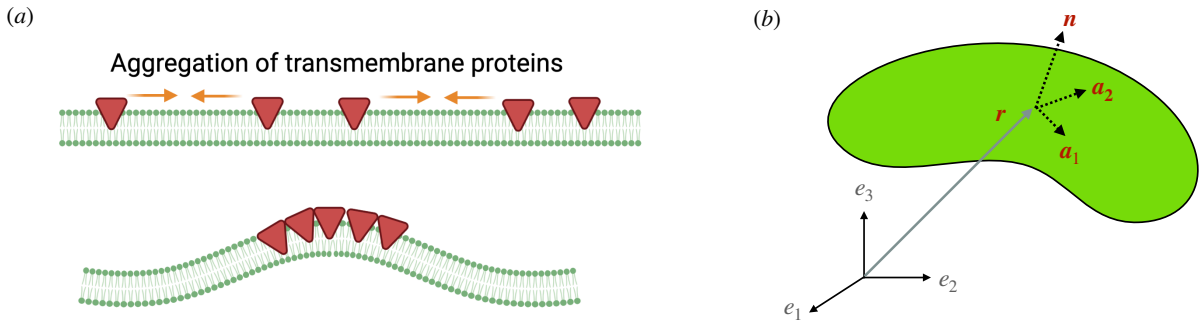

Figure 5.1: Schematic of protein aggregation and representation of a membrane surface. (*a*) Aggregation of transmembrane proteins on the membrane can lead to domain formation and curvature generation. Here, we develop a continuum model that captures these different interactions. (*b*) Representation of a membrane surface and the surface coordinates. $\boldsymbol{r}$ is the position vector, $\boldsymbol{a}_1$ and $\boldsymbol{a}_2$ are the tangent basis vectors, $\boldsymbol{n}$ is the unit surface normal.

While the classical theories were developed for three-dimensional continua, domain formation and phase separation on two-dimensional surfaces such as lipid bilayers have been of great interest recently. The aggregation of proteins on the membrane surface can be viewed as an example of a binary system with lipids and proteins as two phases in a two-dimensional curvilinear space. For example, a recent modeling study showed that in a reaction-diffusion system, a pair of activator and inhibitor molecules can lead to an aggregation instability in a specific parameter space, and this instability governs the pattern formation of proteins on membranes [151]. There are many models in the literature that investigate various aspects of phase separation on surfaces. Gera and Salac [60] numerically solved a Cahn-Hilliard system for aggregation-diffusion on a closed torus and observed the temporal evolution of the formation of the aggregation patches. In this case, the surface geometry was fixed. In a subsequent study, they analyzed the effect of bulk shear flow on the dynamics of the density distribution of species on a deformable vesicle, where the material properties are dependent on the species concentration [152]. Nitschke *et al.* [58] modeled aggregation-diffusion of a two-phase mixture on a spherical surface with in-plane viscous flow, and presented numerical results on pattern formation between

the two phases and its strong interplay with the surface flow. The relative interactions between the proteins on the cellular membrane can lead to phase segregation and form protein domains depending on the strength of interaction forces compared to the entropy of mixing [26]. Such aggregation phenomena have been modeled as a polymerization reaction with a very weak free energy of polymerization [26].

Here, we seek to develop a comprehensive mathematical model that captures the coupled diffusion and aggregation dynamics, where the proteins induce a curvature resulting in membrane bending and lipids can flow in the plane of the membrane. Such a framework allows us to explore how the different transport contributions in the plane of the membrane (protein aggregation, protein diffusion, and lipid flow) can contribute both to the formation of protein microdomains and to the curvature generation capability of the membrane. The chapter is organized as follows. The full system of governing equations is presented in Section 6.2. We first analyzed the special case in the absence of bending and reduced the model to a classic Cahn-Hilliard system in Section 5.3. We solved the Cahn-Hilliard equation numerically on a square domain and demonstrated the configuration of patch formations in the parameter space. Next, we simulated the fully coupled system in the case of small deformations from a flat plane in Section 5.4 and study the effect of bending energy on the dynamics of aggregation and diffusion of proteins. Our results show that coupling between curvature, protein aggregation, and diffusion can lead to a strong mechanical feedback loop stabilizing the protein microdomains in regions of high curvature.

5.2 Model development

We first formulate the governing equations for coupled diffusion and aggregation of curvature-inducing proteins on a deformable viscous lipid membrane with bending elasticity, building on previous models [88, 109, 87]. We begin by formulating a free energy function for

the membrane and apply the principle of energy minimization to derive the governing equations. Complete details of the derivation are provided in Appendix B.1.

5.2.1 Free energy of the membrane

Our system consists of the lipids that comprise the membrane and transmembrane proteins that are embedded in the plane of the membrane and are capable of inducing curvature (Figure 7.1). Our model does not include the binding or unbinding of proteins from the bulk or the interactions of the bulk fluid with the membrane. The lipid bilayer is modeled as a thin elastic shell with negligible thickness that can bend out of the plane and be subject to in-plane viscous flow. Importantly, we assume that the membrane is areally incompressible and this constraint is imposed on the membrane using a Lagrange multiplier. Additionally, we use a continuum description for the protein distribution on the membrane. We describe the different contributions to the total free energy of the system in detail below.

We obtain the total free energy density of the membrane, in terms of protein area fraction ϕ, by combining Equations (2.1), (2.8) and (2.12) as

$$W = \underbrace{k_B T \sigma_s \left[\phi \log \phi + (1-\phi)\log(1-\phi)\right]}_{\text{entropic}} + \underbrace{\frac{\gamma \sigma_s}{2}\phi(1-\phi) + \frac{\gamma}{4}|\nabla\phi|^2}_{\text{aggregation}} + \underbrace{\kappa(H-\ell\sigma)^2 + \bar{\kappa}K}_{\text{bending}}. \tag{5.1}$$

5.2.2 Mass conservation of proteins

Conservation of mass for the protein density σ is given by

$$\frac{\partial \sigma}{\partial t} + \nabla \cdot \boldsymbol{m} = 0, \tag{5.2}$$

where the flux is

$$\boldsymbol{m} = \boldsymbol{v}\sigma - \frac{1}{f}\phi\nabla\mu. \tag{5.3}$$

This flux has contributions from advection due to the in-plane velocity field $\boldsymbol{v}$ and from gradients in the protein chemical potential μ. The constant f denotes the thermodynamic drag coefficient of a protein and is related to its diffusivity D by the Stokes-Einstein relation: $D = k_B T/f$.

The chemical potential, μ, is obtained as the variational derivative

$$\mu = \frac{\delta F}{\delta \phi}, \tag{5.4}$$

where F is the total energy of the system of area A, given by,

$$F = \int_{\omega} W(\phi, \nabla\phi)\, dA. \tag{5.5}$$

Note that the energy density is a function of both the protein area fraction ϕ and its gradient $\nabla\phi$. Using the definition of the variational derivative, we get the expression of the chemical potential as:

$$\mu = \frac{\delta F}{\delta \phi} = \frac{\partial W}{\partial \phi} - \nabla \cdot \frac{\partial W}{\partial \nabla \phi}. \tag{5.6}$$

Using Equation (5.1) for W yields

$$\mu = k_B T \sigma_s [\log\phi - \log(1-\phi)] - 2\kappa\ell\sigma_s(H - \ell\sigma_s\phi) - \frac{\gamma\sigma_s}{2}(2\phi - 1) - \frac{\gamma}{2}|\nabla\phi|^2. \tag{5.7}$$

Substituting Equation (5.7) in Equation (5.3) will result in the evolution equation for σ.

5.2.3 System of governing equations

Here we summarize the governing equations for the coupled dynamics of the system. Using Equations (B.5), (B.7) and (D.10) for the stresses, the tangential force balance in Equa-

tion (B.2) becomes [108, 109, 88]

$$\nabla\lambda + \underbrace{2\nu(\nabla\cdot\boldsymbol{d} - \nabla w\cdot\boldsymbol{b}) - 4\nu w\nabla H}_{\text{viscous}} = \\ -\nabla\sigma\Bigg[\underbrace{k_BT\log\frac{\phi}{1-\phi}}_{\text{entropic}} - \underbrace{2\kappa\ell(H-\ell\sigma_s\phi)}_{\text{bending}} - \underbrace{\left(\frac{\gamma}{2}(2\phi-1)+\frac{\gamma}{2\sigma_s}\Delta\phi\right)}_{\text{aggregation}}\Bigg]. \tag{5.8}$$

Here, we have introduced a new variable λ, which is the Lagrange multiplier for area incompressibility and physically represents the membrane tension (see Equation (B.6) in the ESI for details), $\boldsymbol{d}$ is the rate-of-strain tensor (see Equation (B.8) in the ESI for the details), $\boldsymbol{b}$ is the curvature tensor of the surface, and $\Delta(\cdot) = \nabla\cdot\nabla(\cdot)$ is the surface Laplacian. Along with the surface incompressibility condition

$$\nabla\cdot\boldsymbol{v} = 2wH, \tag{5.9}$$

Equation (7.4) describes how the surface pressure gradient is balanced by the tangential contributions of lipid flow, membrane bending, and membrane-protein interactions. On the other hand, Equation (5.9) captures surface incompressibility for a deformed membrane. Equations (5.9) and (7.4) constitute the governing equations for the velocity field and tension on the evolving surface of the membrane.

The shape of the surface is obtained by the normal force balance Equation (B.3), which, after substituting in Equation (B.5), Equations (B.7) and (D.10), is given by

$$\underbrace{\kappa\Delta(H-\ell\sigma_s\phi) + 2\kappa(H-\ell\sigma_s\phi)(2H^2-K) - 2H(\kappa(H-\ell\sigma_s\phi)^2}_{\text{bending}} - \underbrace{2\nu\left[\boldsymbol{b}:\boldsymbol{d} - w(4H^2-2K)\right]}_{\text{viscous}} \\ -2H\Bigg[\underbrace{k_BT\sigma_s\{\phi\log\phi+(1-\phi)\log(1-\phi)\}}_{\text{entropic}} + \underbrace{\frac{\gamma\sigma_s}{2}\phi(1-\phi)+\frac{\gamma}{4}|\nabla\phi|^2}_{\text{aggregation}}\Bigg] = \underbrace{p+2\lambda H}_{\text{capillary}}. \tag{5.10}$$

While this equation is complex and contains many terms, it can be understood intuitively by

making the following observations. In the absence of all other stresses (bending, viscous, entropic, and aggregation), Equation (5.10) simply reduces to the Young-Laplace law. When the viscous, entropic, and aggregation terms are removed, we recover the so-called 'shape equation' that is commonly used in membrane mechanics [108]. The additional terms capture the non-trivial coupling between protein density, aggregation, lipid flow, and membrane bending, and are the novel aspect of the present model. Equation (7.4) and Equation (5.10) both involve the area fraction of proteins $\phi = \sigma/\sigma_s$, which evolves according to the mass conservation equation given by

$$\phi_t + \nabla\cdot(\boldsymbol{v}\phi) = \frac{1}{f}\Delta\phi\left[\frac{k_BT}{1-\phi} + 2\kappa\ell^2\sigma_s\phi - \gamma\phi\right] - \frac{1}{f}\phi\left[2\kappa\ell\Delta H + \frac{\gamma}{2\sigma_s}\Delta^2\phi\right] + \frac{1}{f}\nabla\phi\cdot\left[\nabla\phi\left(\frac{k_BT}{(1-\phi)^2} + 2\kappa\ell^2\sigma_s - \gamma\right) - 2\kappa\ell\nabla H - \frac{\gamma}{2\sigma_s}\nabla(\Delta\phi)\right], \tag{5.11}$$

where ϕ_t denotes the time derivative $\frac{\partial\phi}{\partial t}$. Note that, in the absence of flow and protein-induced spontaneous curvature, Equation (5.11) reduces to the Cahn-Hilliard equation for aggregation-diffusion as discussed in Section 5.3. Additionally, if we eliminate protein aggregation ($\gamma = 0$), in the limit of dilute concentration of proteins ($\phi \ll 1$), we recover the classical equation for Fickian diffusion.

5.2.4 Non-dimensionalization

We non-dimensionalize the system of Equations (7.4)–(5.11) using the following reference scales. The characteristic length scale is taken to be the size L of the domain. The membrane tension λ is scaled by its mean value λ_0. Velocities are non-dimensionalized by $v_c = \lambda_0 L/\nu$, and we use the diffusive time scale $t_c = L^2/D$. Note that the protein area fraction $\phi = \sigma/\sigma_s$ is already dimensionless. The governing equations in dimensionless form (where tildes are used to denote the dimensionless variables) are provided in the ESI (Equation (C.1)–Equation (C.4)).

Table 5.1: List of dimensionless numbers and their definitions in the model of protein aggregation

Dimensionless Number	Expression	Physical interpretation
$\hat{B}$	$\frac{k_B T}{\kappa}$	$\frac{\text{Thermal energy}}{\text{Bending energy}}$
$\hat{L}$	$\frac{\ell}{L}$	$\frac{\text{Spontaneous curvature length}}{\text{Domain length}}$
$\hat{A}$	$\frac{\gamma}{k_B T}$	$\frac{\text{Aggregation coefficient}}{\text{Diffusion coefficient}}$
$\hat{S}$	$\sigma_s L^2$	$\frac{\text{Domain area}}{\text{Protein footprint}}$
$\hat{T}$	$\frac{2L^2\lambda_0}{\kappa}$	$\frac{\text{Membrane tension energy}}{\text{Bending energy}}$
Pe	$\frac{\lambda_0 L^2}{\nu D}$	$\frac{\text{Advection strength}}{\text{Diffusion strength}}$

The system of dimensionless equations involves seven dimensionless groups that are defined in Table 5.1 along with their physical interpretation. In all the analyses that follow, we assume that the trans-membrane pressure, p, is zero. From here on, we use the dimensionless variables but omit the tildes for brevity.

5.3 Cahn-Hilliard system and stability analysis

5.3.1 Reduction to the Cahn-Hilliard system

We first consider the simplified diffusion-aggregation system in the absence of membrane bending and in-plane lipid flow to gain insight into how diffusion and aggregation compete in the plane of the membrane to form protein aggregates (also referred to as patterns or microdomains). We assume that the proteins have zero spontaneous curvature ($\hat{L} = 0$) in this case. As a result of these simplifications, the surface gradient reduces to the planar gradient $\nabla = \frac{\partial}{\partial x}\boldsymbol{i} + \frac{\partial}{\partial y}\boldsymbol{j}$ and the surface Laplacian Δ becomes $\nabla^2 = \frac{\partial^2}{\partial x^2} + \frac{\partial^2}{\partial y^2}$. Neglecting the flow and bending terms in

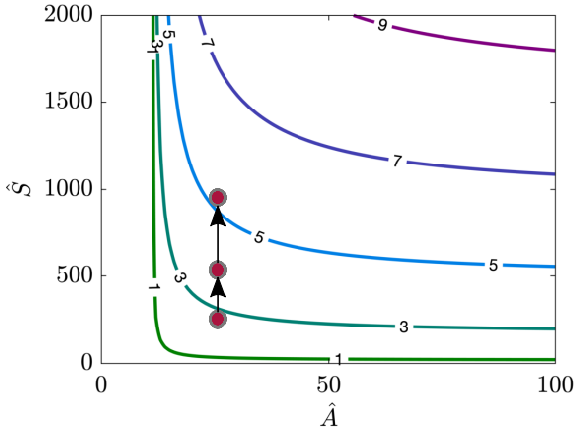

Figure 5.2: Marginal stability curves for the Cahn-Hilliard system in the $(\hat{A},\hat{S})$ plane for $\phi_0 = 0.1$ and various wavenumbers k, as predicted by Equation 5.12. We mark three points in this figure to identify the parameter values for which we perform nonlinear numerical simulations in Figure 5.3.

Equation (5.11), we arrive at a transport equation similar to the Cahn-Hilliard equation:

$$\phi_t = \nabla^2\phi\left[\frac{1}{1-\phi} - \hat{A}\phi\right] + |\nabla\phi|^2\left[\frac{1}{(1-\phi)^2} - \hat{A}\right] - \phi\left[\frac{\hat{A}}{2\hat{S}}\nabla^4\phi\right]. \tag{5.12}$$

Equation (5.12) reduces to Fickian diffusion in the dilute limit ($\phi \ll 1$) in the absence of aggregation ($\hat{A} = 0$). Equation (5.12) is also similar to the system presented by Givli and Bhattyacharya [94], for which they conducted a stability analysis on a closed surface. Here, we present a stability analysis of the equivalent Cahn-Hilliard system on a flat surface, and complement the analysis with numerical simulations of the nonlinear system in a periodic domain.

5.3.2 Linear stability analysis

We perform a linear stability analysis of Equation (5.12) to identify the parameter regimes that can lead to protein aggregation. The homogeneous state with uniform concentration ϕ_0 is perturbed by a small amount ϕ' such that $\phi = \phi_0 + \phi'$. Linearizing Equation (5.12) results in the

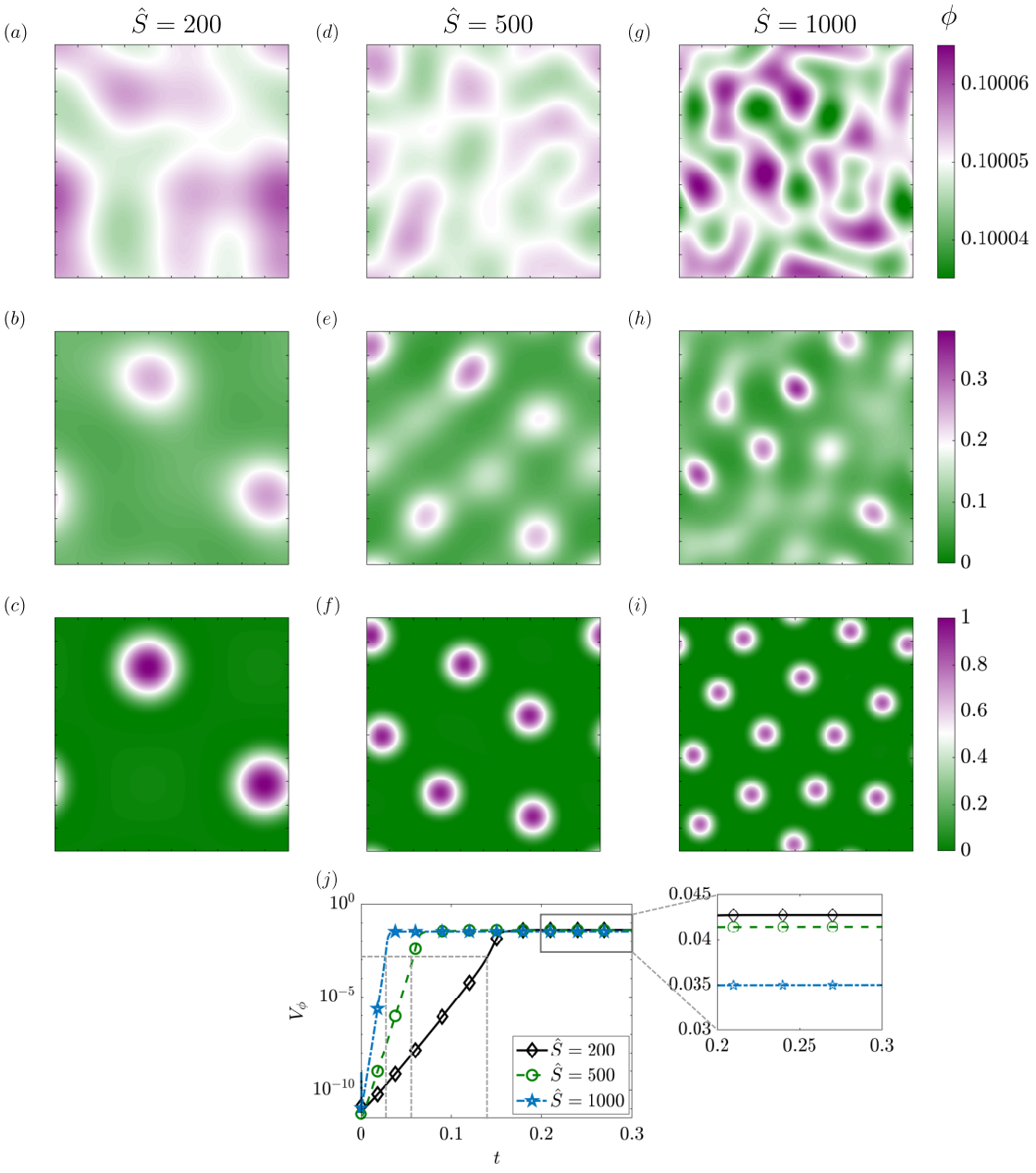

Figure 5.3: Temporal evolution of the protein distribution in simulations of the Cahn-Hilliard model of Equation 5.12 on a flat square patch of area 1 μm^2 for $\hat{A} = 25$ and three different values of $\hat{S}$. The three rows in panels (*a-i*) correspond to three distinct times: at an early time $t_b = 3 \times 10^{-3}$ shortly after the start of the simulation, at an intermediate time t_{in} when protein density variance reaches $V_\phi = 2 \times 10^{-3}$, and at a late time $t_s = 0.3$ when the system has reached steady state. The three columns correspond to $\hat{S} = 200$ (*a-c*), $\hat{S} = 500$ (*d-f*), and $\hat{S} = 1000$ (*g-i*). Also see Movies M1-M3 in the ESI for the corresponding dynamics. (*j*) Temporal evolution of the variance V_ϕ of the protein density for the same cases shown in (*a-i*). The dashed lines indicate the intermediate time t_{in} when the variance reaches $V_\phi = 2 \times 10^{-3}$.

equation for density fluctuation ϕ' as

$$\phi'_t = \nabla^2\phi'\left[\frac{1}{1-\phi_0} - \hat{A}\phi_0\right] - \frac{\hat{A}}{2\hat{S}}\phi_0\nabla^4\phi'. \tag{5.13}$$

We consider normal modes of the form $\phi' = e^{\alpha t}e^{i2\pi \boldsymbol{k}\cdot\boldsymbol{x}}$ and obtain the dispersion relation

$$\alpha = 4\pi^2\left[\hat{A}\phi_0 - \frac{1}{1-\phi_0}\right]k^2 - 8\pi^4\frac{\hat{A}}{\hat{S}}\phi_0 k^4. \tag{5.14}$$

We find that the growth rate α is always real. The first term in Equation (5.14) is positive and is destabilizing as long as the strength of aggregation exceeds a certain threshold: $\hat{A} \geq \hat{A}_c = [\phi_0(1-\phi_0)]^{-1}(\approx 11.1$ for $\phi_0 = 0.1)$,whereas the second term is always stabilizing. The marginal stability curves $\alpha = 0$ in the $(\hat{A},\hat{S})$ plane are plotted for various wavenumbers k in Figure 5.2. For a given choice of $\hat{A}$ and $\hat{S}$, this results in a band of unstable wavenumbers $0 \leq k \leq k_c$, where

$$k_c^2 = \frac{\hat{S}}{2\pi^2}\left[1 - \frac{\hat{A}_c}{\hat{A}}\right], \tag{5.15}$$

and the maximum growth rate occurs at wavenumber $k_m = k_c/\sqrt{2}$. The corresponding wavelength $\Lambda = 2\pi/k_m$ provides a prediction for the characteristic lengthscale of aggregation patches, which is expected to decay with increasing $\hat{S}$ but to increase with increasing $\hat{A}$.

5.3.3 Numerical simulations

We conducted numerical simulations of Equation (5.12) inside a square domain for various combinations of $\hat{A}$ and $\hat{S}$ that satisfy the necessary condition of aggregation as given in Equation (5.15) and Figure 5.2. The initial condition was set as a homogeneous distribution of $\phi_0 = 0.1$ with a small random spacial perturbation with magnitude $|\phi'| \leq 1 \times 10^{-4}$. We numerically restricted the value of ϕ to the interval $[\varepsilon, 1-\varepsilon]$ with $\varepsilon = 1 \times 10^{-3}$ to ensure that neither ϕ or $1-\phi$ becomes zero during the simulations. We used periodic boundary conditions

for the protein density and solved the equation numerically using a finite difference technique. In Figure 5.3, we show the evolution of the protein distribution over time for three different values of the dimensionless number $\hat{S}$ that denotes the ratio of domain area to the protein footprint, while maintaining the aggregation strength at $\hat{A} = 25$. In all cases, we find that the initial perturbation in the density field evolves towards the formation of distinct dense circular protein patches that are distributed randomly and nearly uniformly across the domain, in agreement with standard Cahn-Hilliard aggregation dynamics [60]. The main effect of varying $\hat{S}$, which is more dramatic than varying $\hat{A}$ as we further show below, is to control the number of patches as well as their size. Indeed, we recall that $\hat{S}$, which is a dimensionless measure of the finite size of the proteins, directly controls the stabilizing term in the dispersion relation Equation (5.14) and therefore the dominant wavenumber of the instability. Consistent with the stability predictions, we find that larger values of $\hat{S}$ produce larger numbers of patches with smaller sizes. During the transient evolution, proteins get drawn towards the emerging patches due to aggregation, and at steady state we find that the density inside the patches approached the saturation density ($\phi = 1$), whereas it approaches zero outside (Also see Movies M1-M3 in the ESI). We quantify the growth of density fluctuations by plotting in Figure 5.3*j* the time evolution of the density variance, defined as

$$V_\phi = \int_A (\phi - \phi_0)^2 dA. \tag{5.16}$$

We find that the growth of the variance is exponential at short times, consistent with the expected behavior for a linear instability, before reaching a constant plateau at long times. The growth is observed to increase with $\hat{S}$ in agreement with the linear prediction of Equation (5.14). The steady state value, on the other hand, is found to decrease slightly with $\hat{S}$, although the differences are small.

A more complete exploration of pattern formation is provided in Figure 5.4*a*, showing the long-time configurations of aggregated protein patches in the parameter space of $\hat{A}$ and $\hat{S}$. We

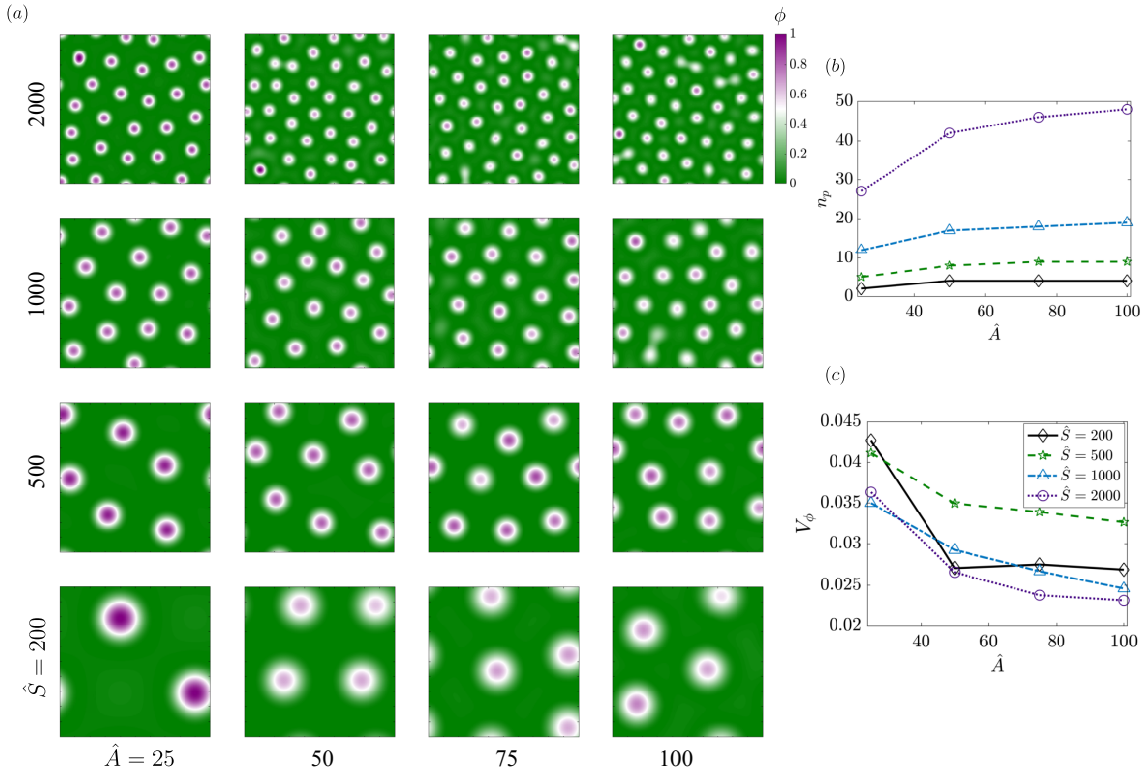

Figure 5.4: (*a*) Configurations of protein aggregates on a flat square membrane at a late time $t = 0.3$ approaching steady state for various combinations of $\hat{A}$ and $\hat{S}$. (*b*) Variation of the number of protein patches with $\hat{A}$, for different values of $\hat{S}$. (*c*) Variation of of the protein density variance V_ϕ with $\hat{A}$ for different values of $\hat{S}$.

note that the number of patches, their size, and their homogeneity vary with both parameters. As we already observed in Figure 5.3, increasing $\hat{S}$ for a given value of $\hat{A}$ increases the number of patches and decreases their size. On the other hand, increasing $\hat{A}$ for a given $\hat{S}$ tends to increase inhomogeneity among patches, with some visibly denser patches while others tend to be more diffuse. The dependence of the number of patches as a function of both $\hat{A}$ and $\hat{S}$ is shown in Figure 5.4*b*, while the steady-state variance is plotted in Figure 5.4*c*. The variance is found to decrease with $\hat{A}$, as the more diffuse patches forming at large $\hat{A}$ result in weaker spatial fluctuations.

5.4 Coupling of aggregation with bending: analysis in the small deformation regime

To understand how the inclusion of membrane curvature alters the aggregation-diffusion landscape, we simulated the dynamics of the coupled system Equations (C.1) to (C.4) in the regime of small deformations from a plane. The surface is represented using the Monge parametrization, such that the position vector is given by $\boldsymbol{r} = x_\alpha \boldsymbol{e}_\alpha + z(x_1, x_2, t)\boldsymbol{e}_3$. In the regime of small deformations from the plane, we consider gradients of the surface deformation to be small and ignore the higher-order terms [88]. The surface gradient and Laplacian in the Monge parameterization simplify to $\nabla = \frac{\partial}{\partial x}\boldsymbol{i} + \frac{\partial}{\partial y}\boldsymbol{j}$ and $\nabla^2 = \frac{\partial^2}{\partial x^2} + \frac{\partial^2}{\partial y^2}$. In the limit of small deformations, the system of governing equations Equation (C.2) to Equation (C.4) reduces to Equation (B.14) to Equation (B.17).

5.4.1 Linear stability analysis

We first perform a stability analysis of the system of equations (Equation (B.14) to Equation (B.17)) to identify the parameter regimes similar to the analysis of Section 5.3.2 but in

the presence of bending due to spontaneous curvature induced by the protein. In the base state, the membrane is flat and at rest with uniform tension ($z_0 = 0$, $\boldsymbol{v}_0 = \mathbf{0}$, $\lambda_0 = 1$), and the protein density is uniform with value ϕ_0. We showed in an earlier study [88] that a uniform protein distribution on a flat membrane is indeed a steady state even when the proteins induce a spontaneous curvature. We perturb the variables by small amounts with respect to this base state:

$$\phi = \phi_0 + \phi', \quad z = 0 + z', \quad \boldsymbol{v} = \mathbf{0} + \boldsymbol{v}', \quad \text{and,} \quad \lambda = 1 + \lambda'. \tag{5.17}$$

Linearizing Equations (B.14) and (B.15) provides the governing equations for velocity and tension fluctuations as

$$\nabla \cdot \boldsymbol{v}' = 0, \tag{5.18}$$

and,

$$\nabla\lambda' + \nabla^2\boldsymbol{v}' + \nabla(\nabla\cdot\boldsymbol{v}') = -\nabla\phi'\left[\frac{2\hat{B}\hat{S}}{\hat{T}}\log\frac{\phi_0}{1-\phi_0} + \frac{4\hat{L}^2\hat{S}^2}{\hat{T}}\phi_0 - \frac{\hat{A}\hat{B}\hat{S}}{\hat{T}}(2\phi_0 - 1)\right]. \tag{5.19}$$

The normal force balance of Equation (B.16) reduces to

$$\nabla^4 z' - 2\hat{L}\hat{S}\nabla^2\phi' - 2\hat{B}\hat{S}\nabla^2 z'\left[\{\phi_0\log\phi_0 + (1-\phi_0)\log(1-\phi_0)\} + \frac{\hat{A}}{2}\phi_0(1-\phi_0) + \frac{\hat{L}^2\hat{S}}{\hat{B}}\phi_0^2\right] = \hat{T}\nabla^2 z'. \tag{5.20}$$

Finally, the transport equation for the protein density given in Equation (B.17) becomes

$$\phi_t' = \nabla^2\phi'\left[\frac{1}{1-\phi_0} + \frac{2\hat{L}^2\hat{S}}{\hat{B}}\phi_0 - \hat{A}\phi_0\right] - \phi_0\left[\frac{\hat{L}}{\hat{B}}\nabla^4 z' + \frac{\hat{A}}{2\hat{S}}\nabla^4\phi'\right]. \tag{5.21}$$

We find that the linearized equations the velocity field and tension partially decouple from the shape equation (5.20) and protein transport equation (5.21): in other words, lipid flow and tension fluctuations do not affect the membrane shape and protein transport in the linear regime. To

analyze the dynamics of protein aggregation, we therefore need only consider Equations (5.20) and (5.21). Performing a normal model analysis (see ESI for details), we obtain the dispersion relation as

$$\alpha = 4\pi^2 k^2 \left[\hat{A}\phi_0 - \frac{1}{1-\phi_0} - \frac{2\hat{L}^2\hat{S}}{\hat{B}}\phi_0 g(k) \right] - 8\pi^4 \phi_0 \frac{\hat{A}}{\hat{S}} k^4, \tag{5.22}$$

where $g(k)$ is given by

$$g(k) = 1 - \frac{16\pi^4 k^4}{M(k)}, \tag{5.23}$$

and,

$$M(k) = 16\pi^4 k^4 + 8\pi^2 k^2 \hat{B}\hat{S}\left[\{\phi_0 \log\phi_0 + (1-\phi_0)\log(1-\phi_0)\} + \frac{\hat{A}}{2}\phi_0(1-\phi_0) + \frac{\hat{L}^2\hat{S}}{\hat{B}}\phi_0^2 \right] + 4\pi^2 k^2 \hat{T}. \tag{5.24}$$

Similar to Equation (5.14), the second term in Equation (5.22) is always stabilizing, and therefore protein aggregation takes place only if the first term is positive. The necessary condition for protein aggregates to form becomes

$$\hat{A} - \frac{2\hat{L}^2\hat{S}}{\hat{B}} g(k) \geq \frac{1}{\phi_0(1-\phi_0)}, \tag{5.25}$$

or

$$\hat{A} \geq \hat{A}_c + \frac{2\hat{L}^2\hat{S}}{\hat{B}} g(k), \tag{5.26}$$

where $\hat{A}_c$ was previously defined in Section 5.3.2 in the Cahn-Hilliard case. Here again, we find that there exists an unstable range of wave numbers $0 < k < k_c$, where k_c satisfies the implicit equation

$$k_c^2 = \frac{\hat{S}}{4\pi^2}\left[1 - \frac{\hat{A}_c}{A} - \frac{2\hat{L}^2\hat{S}}{\hat{B}\hat{A}} g(k_c) \right]. \tag{5.27}$$

The maximum growth rate occurs at wavenumber k_m, also given by an implicit equation:

$$k_m = \frac{k_c}{\sqrt{2}}\left[1 + \frac{1}{4\pi^2 k_m}\frac{\hat{L}^2\hat{S}^2}{\hat{B}\hat{A}} g'(k_m) \right]^{-1/2}. \tag{5.28}$$

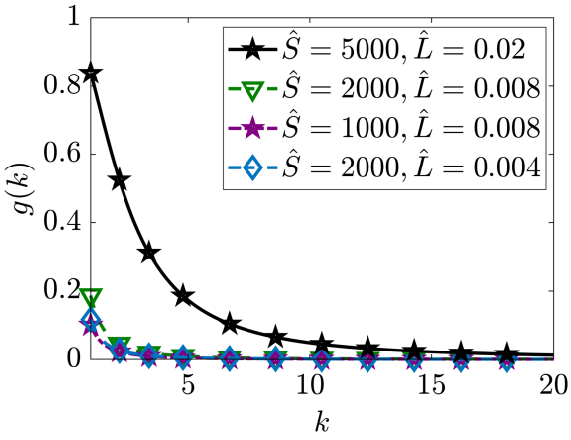

Figure 5.5: Dependence of g defined in Equation (5.23) on wavenumber k for different values of $\hat{S}$ and $\hat{L}$, with $\hat{A} = 25$.

Figure 5.5 shows the dependence of $g(k)$ on wave number k for $\hat{A} = 25$ and various combinations of $\hat{L}$ and $\hat{S}$. When both $\hat{L}$ and $\hat{S}$ increase, $g(k)$ tends to increase for small wavenumbers and thus stabilizes the system. This means in particular that proteins with large spontaneous curvature, as captured by $\hat{L}$, can in fact have a stabilizing effect on protein aggregation, and this counterintuitive observation will be confirmed in numerical simulations as we discuss next.

5.4.2 Numerical simulations

We solved Equations (B.14) to (B.17) numerically on a square domain with periodic boundary conditions for a small random density perturbation over a homogeneous steady state density of $\phi = 0.1$. The proteins now induce a spontaneous curvature in the membrane, and the model also captures the viscous flow on the membrane manifold. Typical transient dynamics are illustrated in Figure 5.6 in a simulation with $\hat{L} = 8 \times 10^{-3}$, $\hat{A} = 25$, and $\hat{S} = 2000$. The initial random distribution resolves into strong patches of proteins over time with the same number of patches as we observed in the Cahn-Hilliard system (compare Figure 5.3*a-c* with Figure 5.6*a-c*). Because the system of equations now accounts for coupling of curvature with protein dynamics, we observe that the formation of dense protein patches is accompanied by the

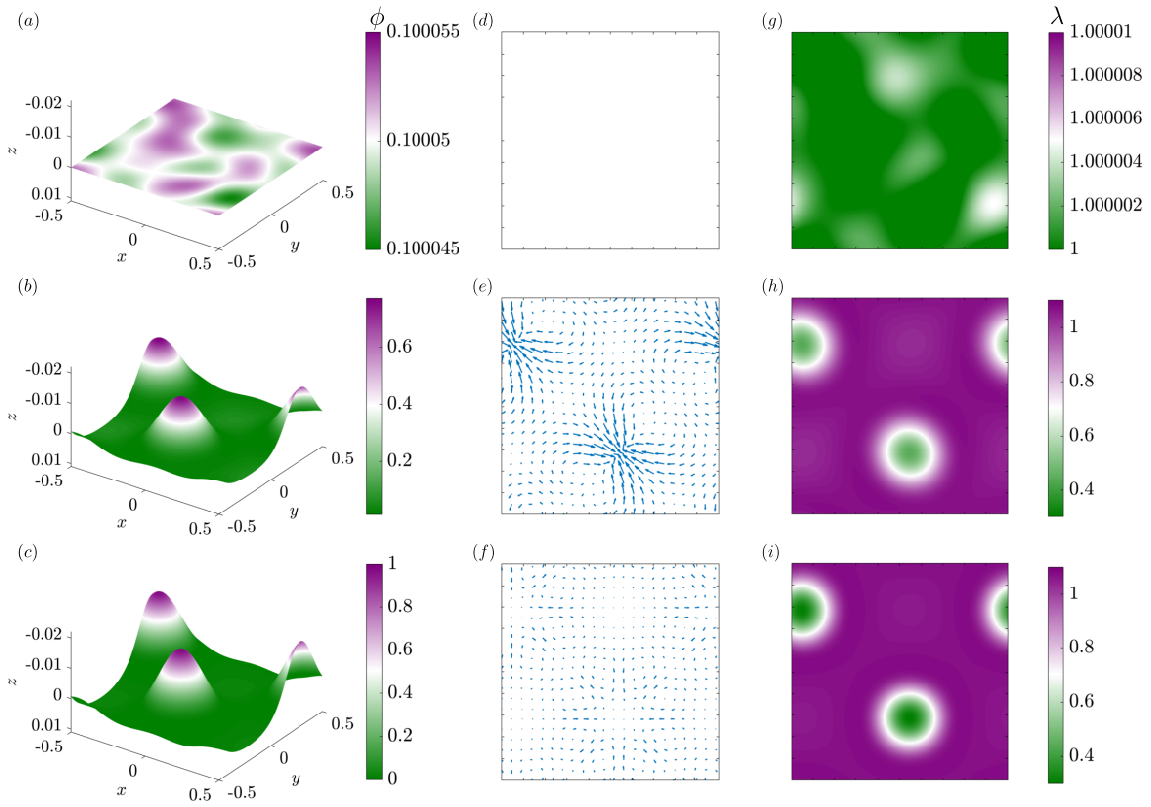

Figure 5.6: Temporal evolution of protein distribution, membrane shape, in-plane velocity and tension for a square membrane of size 1 μm^2 with $\hat{A} = 25$, $\hat{S} = 200$, and $\hat{L} = 8 \times 10^{-3}$. (*a-c*) Height of the membrane colored with the local protein density, (*d-f*) in-plane velocity field, and (*g-i*) membrane tension at dimensionless times 0.003, 0.216, and 0.3.

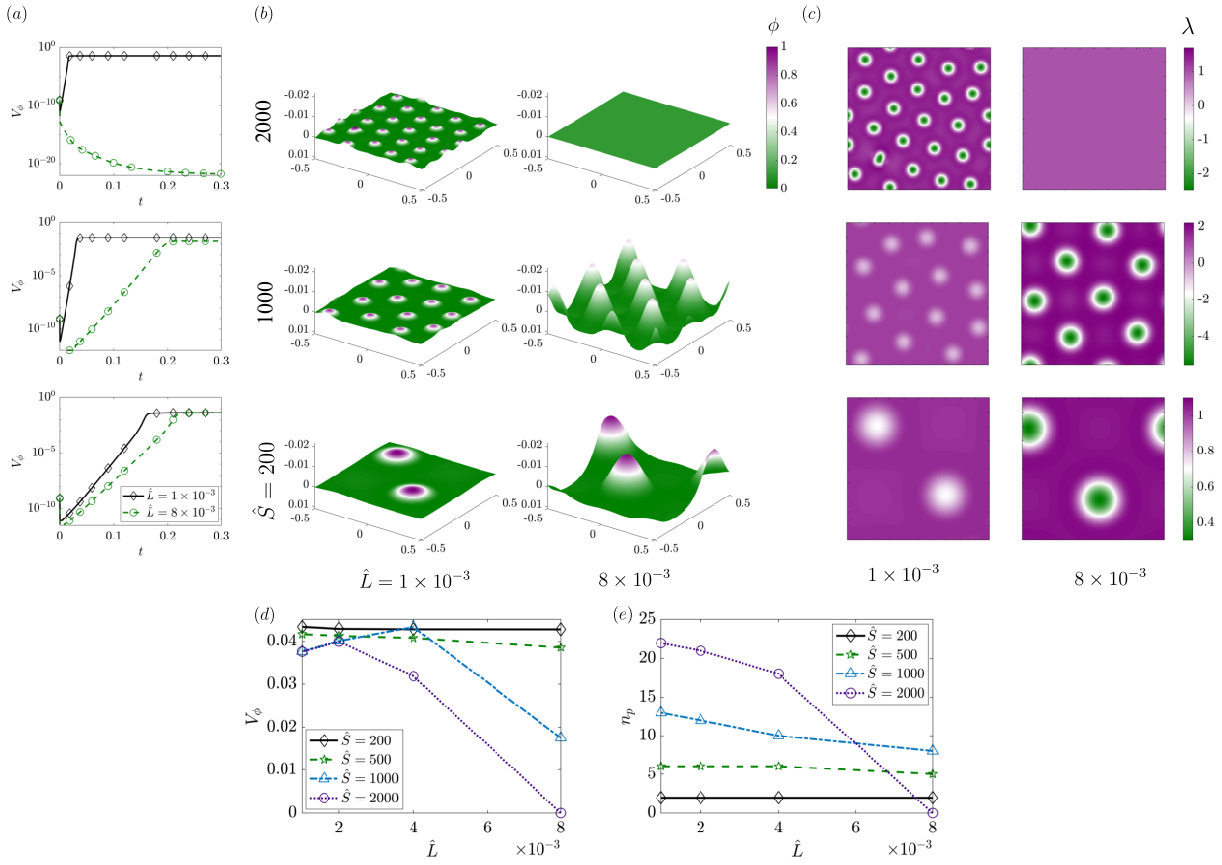

Figure 5.7: Effect of $\hat{S}$ and $\hat{L}$ on protein aggregation and membrane dynamics. (*a*) Temporal evolution of the protein density variance V_ϕ for two values of $\hat{L}$ and the same three values of $\hat{S}$ shown in (*b*). (*b*) Distribution of protein density on the deformed membrane at a long time approaching steady state ($t = 0.3$) for various combinations of $\hat{L}$ and $\hat{S}$, with $\hat{A} = 25$. The corresponding dynamics are also shown in movies M4-M6 of the ESI. (*c*) Distribution of the local membrane tension for the same cases as in (*b*). (*d*) Variance of protein density V_ϕ and (*e*) number of protein patches n_p at $t = 0.3$ as functions of $\hat{L}$, for various values of $\hat{S}$.

localized growth of membrane deformations, in the form of nearly circular peaks surrounded by flatter regions of oppositely-signed curvature (Figure 5.6*a*-*c*). We also observe that the formation of protein aggregates is coupled with a tangential velocity field in the plane of the membrane, to accommodate the deformation of the membrane (Figure 5.6 *d*-*f*): as the protein aggregates form and deflect the membrane in the normal direction, a source-like flow is generated locally as dictated by the continuity relation Equation (B.14). During this process, the magnitude of the velocity increases until the system approaches a steady state where aggregation balances diffusion. As the steady state is approached, the flow in the membrane changes nature as the normal velocity vanishes, with each protein patch driving a weaker flow with quadrupolar symmetry.

As we have noted in prior works [109, 112, 88], coupling of lipid flow to membrane deformation not only completes the description of the physics underlying the viscoelastic nature of the membrane but also allows for the accurate calculation of the membrane tension field (the Lagrange multiplier for incompressibility). This is particularly relevant for understanding how microdomains of proteins can alter the tension field in the membrane. The tension field on the membrane tracks with the protein microdomains and the deformation in the coupled system (Figure 5.6*g*-*i*). Initially, the membrane has nearly uniform tension, but as regions of high protein aggregation and therefore high membrane curvature form, these locations are found to have lower tension in comparison with the rest of the membrane (see [112] for a detailed discussion on this point). Thus, the dynamics of the coupled system is able to capture key experimental observations in the field of membrane-protein interactions: (a) regions of high curvature and aggregation are correlated for curvature-inducing proteins suggesting a positive feedback between these two important factors [153], (b) lipid flow is important to sustain the deformations ([154]), and (c) membrane tension is a heterogeneous field and varies with the local membrane composition [155].

To further quantify these behaviors, we investigated the parameter space of $\hat{S}$ and $\hat{L}$, to understand how the spontaneous-curvature induction versus protein footprint compete in a fixed

regime of aggregation-to-diffusion ($\hat{A} = 25$ fixed) (see Equation (5.26)). We varied $\hat{S}$ in the range of 200 to 2000 and $\hat{L}$ from 1×10^{-3} to 8×10^{-3} and summarize these results in Figure 5.7. We first observed that the growth rate of the variance of ϕ shows a strong dependence on $\hat{L}$ (Figure 5.7*a*). For $\hat{S} = 200$, the growth rate for the two different values of $\hat{L}$ differ slightly with the growth rate being slower for larger $\hat{L}$. This effect persists and is amplified for larger $\hat{S}$: as both $\hat{S}$ and $\hat{L}$ increase, the growth rate decreases, indicating that it takes longer time for patterns to form on the membrane. However, when $\hat{S} = 2000$, we see a decay in the variance of protein density ϕ as opposed to the exponential growth and eventual plateau for the cases where protein aggregrates form. This result, which is consistent with the stability analysis of Section 5.4.1 suggests that the induction of curvature on the membrane can alter significantly the dynamics of protein aggregation.

The steady-state patterns and deformations are illustrated in Figure 5.7*b* (also see Movies M4-M6, and Figures B.1 and B.2 in the ESI), where we observe that the number of protein patches is largely unaffected by $\hat{L}$ for $\hat{S} = 200$. The number of patches increases with $\hat{S}$ for a given $\hat{L}$ (as already found in Figure 5.4). However, when $\hat{S}$ increases to 1000, the number of patches decrease with $\hat{L}$. Since the deformation is directly affected by spontaneous curvature, we find however that $\hat{L}$ has a strong effect on the magnitude of membrane deflections, with larger protein footprints resulting in stronger deflections. Surprisingly, when $\hat{S} = 2000$, we noticed that protein aggregates do not form for the value of $\hat{L} = 8 \times 10^{-3}$ and the membrane remains flat. This phenomenon can be explained from the critical value of $\hat{A}$ in Equation (5.26). Since both $\hat{L}$ and $\hat{S}$ have a stabilizing effect on density fluctuations ϕ' (Equation (5.26)), for higher value of $\hat{S}$ and $\hat{L}$, an aggregation coefficient of $\hat{A} = 25$ is not sufficient to overcome the stabilizing barrier. However, for lower values of $\hat{L}$ or lower values of $\hat{S}$, where the stabilizing effect is relatively weak, we see the formation of protein aggregates.

The tension profile in the membrane follows the inhomogeneity of the protein distribution as expected (Figure 5.7*c* and Figure B.2). As previously noted in Figure 5.6, the patches are

associated with tension minima. We find that the range of λ depends strongly on $\hat{S}$ and $\hat{L}$, as $\nabla\lambda$ linearly depends on the negative of the gradient of the spontaneous curvature, which in turn depends on both ℓ and σ. This is consistent with our previous results showing that λ is a heterogeneous field on the membrane and varies with the protein-induced spontaneous curvature [112, 88]. Figure 5.7*c* further highlights the coupling between curvature, flow, and aggregation dynamics. Finally, we look at the variance and the number of patches as a function of both $\hat{S}$ and $\hat{L}$ (Figure 5.7*d,e*). We note that for a given value of $\hat{S}$, the variance decreases with increasing $\hat{L}$ for higher values of $\hat{S}$ and this decrease is more dramatic when compared to the Cahn-Hilliard model (Figure 5.4*b*). Even though the number of patches remains more or less unaltered for small values of $\hat{S}$ as $\hat{L}$ increases, the number decreases with increasing $\hat{L}$ for larger values of $\hat{S}$ (Figure 5.7*e*), consistent with the stability behavior noted in Equation (5.26). These results suggest that the landscape of protein inhomogeneity is not only governed by the $\hat{A}$-$\hat{S}$ space as is the case in the Cahn-Hilliard model; rather the curvature parameters, specifically $\hat{L}$ in this case, can have a significant impact on the protein aggregation behavior. Thus, we find that the aggregation-diffusion landscape on the surface of the membrane is altered by the protein-induced spontaneous curvature – tuning these different effects can allow for differential control of curvature-aggregation feedback.

5.5 Discussion

The interaction of peripheral and integral membrane proteins with the lipid bilayer of cellular membranes is fundamental to cellular function [156, 157, 158]. In this work, we have developed a comprehensive modeling framework that couples the multiple effects that take place in such membrane-protein interactions: protein diffusion in the plane of the membrane, interaction between the proteins resulting in aggregation, lipid flow in the plane of the membrane, and out-of-plane curvature generation due to protein-induced spontaneous curvature. The resulting system of

equations now completely describes the mechanics of a lipid membrane with a second species that can both diffuse and aggregate in the plane of the membrane. We compared this system against a reduced system of Cahn-Hilliard equations to show how the coupling with membrane bending alters the system behavior using both linear stability analysis and numerical simulations. In the absence of curvature coupling (the Cahn-Hilliard system), the dynamics of protein aggregation is driven by the competition between two key parameters, $\hat{S}$, representing the relative size of the protein footprint and $\hat{A}$, representing the relative strength of protein aggregation over diffusion. In the presence of curvature coupling due to protein-induced spontaneous curvature, these dynamics are altered and depend strongly on the strength of the spontaneous curvature induced by these proteins. These altered dynamics can be summarized as follows: for certain regimes of $\hat{S}$ and $\hat{L}$, microdomains of proteins form on the membrane and are closely tied to the membrane curvature as is expected, generating a strong feedback between curvature and aggregation. We also found that for certain regimes of $\hat{S}$ and $\hat{L}$, the growth rate decays, preventing the formation of protein aggregates and the membrane remains flat.

The interaction between curvature and protein aggregation in membranes has been studied in multiple modeling [159, 160, 93, 94], simulation [25, 26, 60], and experimental contexts [161, 162, 163, 164, 165]. Our work builds on this literature with a few key differences. Many of the theoretical models analyze the governing equations in simplified settings. In some cases, the geometry is fixed and the emergence of patterns is analyzed, and in other cases, the dynamics of the protein interactions on the surface is ignored [94, 60]. Here, we have analyzed the fully coupled system without any assumptions on the dominant regimes and demonstrated how curvature generation can affect aggregation. Another important feature of our model is the calculation of membrane tension. Since the lipid bilayer is assumed to be incompressible, the calculation of the Lagrange multiplier, which is widely interpreted as membrane tension (see detailed discussion in [112] and references therein), is an important aspect of the coupled physics. By incorporating the viscous nature of the membrane, we ensure that the incompressibility constraint is met

rigorously at all times and therefore obtain the tension fields on the membrane. Our calculation of the heterogeneous tension fields are consistent with previous models as noted above and with experimental observations [166]. Moreover, a lower tension inside the phase-separated domain further supports the existence of line tension at the domain boundary, which has been observed experimentally [155].

Finally, we discuss the relevance of our model in the context of biological systems. Coarse-grained molecular dynamic simulations of N-BAR proteins on flat membranes and spherical vesicles showed that at low protein density these proteins form linear aggregates and meshes on the membrane surface [167]. Many proteins, especially those that belong to the coat family of proteins including clathrin and COP, are known to aggregate on the membrane and their aggregation results in morphologolical changes of the membrane [168]. The nucleation of these protein aggregates and the subsequent deformation of the membrane has been studied using simplified systems [169]. While the exact role of lipid flow, diffusion, and aggregation is often not unraveled in these experiments, they have shown that the extent of curvature induced depends on multiple physical parameters including the composition of the membrane and the nature of the protein [157, 170]. From a physiological perspective, many neurodegenerative diseases such as Alzheimer's disease, Parkinson's disease, and Huntington's disease are associated with surface aggregation of proteins in cells. Even though the precise mechanisms of such aggregation are not fully established, the role of membrane-protein interactions, particularly aggregation, is becoming increasingly important [171].

The formation of domains is not specific to lipid-protein systems but is also observed in vesicles that have two different kinds of lipids. The temporal behavior of formation of disordered lipid domains was studied in a ternary mixture of fluid membrane [154] and it was shown that in-plane flow was critical to the formation of such domains [58] and that smaller domains can be attracted towards larger domains following the internal flows [172].

In developing models for many of these experimental observations described above,

aggregation of domains of protein-induced curvature is often assumed *a priori* or curvature is proposed as an organizing factor to explain cellular observations and experiments in reconstituted systems [173, 174, 175, 176, 177, 178, 179]. By developing a general theoretical framework that accounts for the coupled effects of protein diffusion, aggregation, and curvature generation, we have eliminated the need for such strong assumptions and more importantly, demonstrated that the intricate interactions between these different physics can lead to different regimes of pattern formation and membrane deformations. These regimes can be tuned and controlled by different parameters, allowing for exquisite control of experimental design. In summary, the comprehensive model that we have developed here allows for a broader interpretation and understanding of membrane-protein interactions in a unifying framework.

5.6 Acknowledgments

I would like to acknowledge my co-authors: Prof. Padmini Rangamani and Prof. David Saintillan. This chapter is primarily based the published material appeared in Soft Matter (2021) authored by Arijit Mahapatra, David Saintillan, and Padmini Rangamani. The dissertation author was the primary author of the work.

Chapter 6

Binding and unbinding of curvature inducing proteins to the membrane

6.1 Introduction

Chapter 5 showed how the aggregation of proteins competes with their diffusion to initiate phase transition of the proteins, which drives the localization of curvature-inducing proteins and generates membrane curvature [180]. The mass of proteins are considered to be conserved in the membrane plane. However, protein exchange happens from membrane to the cytoplasm through binding and unbinding. The equilibrium and non-equilibrium binding of proteins to the membrane from the cytoplasm can lead to the phase transition of proteins [83], which cause local deformation of the membrane. The protein binding on the other hand are found to be curvature dependent in numerous experiments [86]. This establishes a strong curvature-driven feedback in the process of protein binding.

A series of experimental [181, 182] and numerical studies [84, 85] investigated the kinetics of binding and unbinding of proteins, and the resulting protein dynamics mimic several biophysical processes. The equilibrium binding of non-interacting particles in membranes

follows the Langmuir isotherm as a function of bulk concentration and available binding sites in membranes, which is modified to include the effect of crowding, reaction rates, and diffusion of particles subsequently [183]. Non-equilibrium binding of proteins shows formations of hexagonal lattices in Monte Carlo simulation [184]. However, a multicomponent reaction-diffusion system in the presence of binding shows a wide variety of chemical instabilities in the plane of membranes ranging from pattern formation, chemical turbulence, standing, and traveling waves [185]. The instabilities are found in living cells, and simplified experiments carried out in lipid vesicles and supported lipid bilayers are backed up by rigorous theories of stability analysis [182]. Such instabilities are pertinent in the limiting cases of single component binding.

In this chapter, we will focus on how the binding and unbinding of proteins to the membrane from the cytoplasm influence the protein's dynamics and how bending influences the energy landscape. We first extended the theoretical framework presented in Chapter 4 and Chapter 5 to encounter protein binding in addition to the bending of the membrane, in-plane flow of lipid, aggregation, and diffusion of proteins. Here we also considered the dynamics of the density of proteins at the bulk during binding and unbinding, which gives a two-component dynamical system. We performed a stability analysis to find the necessary condition for phase separation in the membrane in such a system. Subsequently, we demonstrate our model with the help of numerical simulations in axisymmetric geometries and identified some of the significant phase-transition behavior in curved membranes.

6.2 Model development

In this section, we formulate the governing equations for coupled diffusion and aggregation of curvature-inducing proteins on a deformable viscous lipid membrane with bending elasticity, building on our previous model [88]. We first formulate a free energy function for the membrane and subsequently present the governing conservation equation and equations of motion.

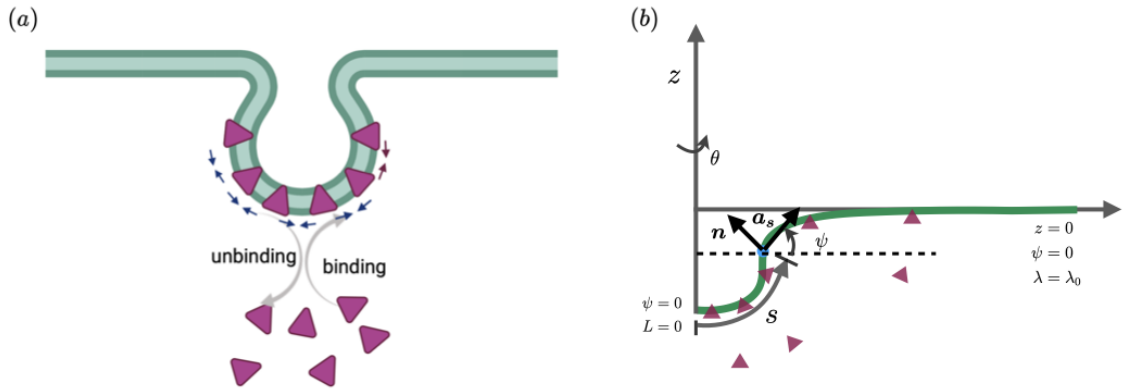

Figure 6.1: Membrane representation in axisymmetry with protein distribution area and boundary conditions. (a) Schematic of binding and unbinding of a curvature-inducing protein and resultant aggregation in the plane of the membrane. (b) Solution domain with protein coat and boundary conditions.

6.2.1 Free energy of the membrane

$$W = \underbrace{k_B T \sigma_s \left[\phi \log \phi + (1-\phi)\log(1-\phi)\right]}_{\text{entropic}} + \underbrace{\frac{\gamma \sigma_s}{2}\phi(1-\phi) + \frac{\gamma}{4}|\nabla\phi|^2}_{\text{aggregation}} + \underbrace{\kappa(H-\ell\sigma)^2 + \bar{\kappa}K}_{\text{bending}} - \underbrace{\mu_b \sigma}_{\text{binding}} . \tag{6.1}$$

Here σ is the density of the proteins, σ_s denotes the saturation density, and $\phi = \sigma/\sigma_s$ represents the area fraction of protein in the surface of the membrane. The entropic, aggregation and bending contributions of the free energy of the membrane have been discussed in [180]. The free energy of protein binding in Equation (5.1) linearly depends on the density of proteins; the slope μ_b is defined as the chemical potential of binding.

6.2.2 Mass conservation of proteins

Conservation of mass for the protein density σ in the plane of the membrane is expressed as

$$\frac{\partial \sigma}{\partial t} + \boldsymbol{\nabla} \cdot \boldsymbol{m} = q(\sigma, \sigma_b). \tag{6.2}$$

Here, q is the net rate of binding of the proteins, and σ_b is the density of the proteins in bulk. The proteins flux in the membrane, $\boldsymbol{m}$, is given by the following constitutive relation in the presence of a tangential velocity field $\boldsymbol{v}$

$$\boldsymbol{m} = \boldsymbol{v}\sigma - \frac{1}{f}\phi \boldsymbol{\nabla} \mu, \tag{6.3}$$

where f is a constant denoting the thermodynamic drag coefficient of the protein and is related to its diffusivity D by the Stokes-Einstein relation: $D = k_B T/f$. The chemical potential μ is obtained as the variational derivative of free energy given in Equation (6.1) and is given by

$$\mu = k_B T \sigma_s [\log \phi - \log(1-\phi)] - 2k\ell\sigma_s(H - \ell\sigma_s\phi) - \frac{\gamma\sigma_s}{2}(2\phi - 1) - \frac{\gamma}{2} a^{\alpha\beta} |\boldsymbol{\nabla}\phi|^2 - \mu_b \sigma_s, \tag{6.4}$$

where σ_b is the density of the protein in the bulk domain Ω, which is assumed to be a well-mixed. A well-mixed system depicts the situation when the diffusion coefficient on the membrane is much lower than the diffusion coefficient at the bulk. The conservation equation for σ_b at the bulk is given by

$$\frac{\partial \sigma_b}{\partial t} = -\frac{1}{V}\int_A q(\phi, \sigma_b) \mathrm{d}A. \tag{6.5}$$

6.2.3 Binding rate

In this study we considered a non-linear binding rate of proteins as given by the following relation [181]

$$q(\phi, \sigma_b) = \sigma_b (k_1 + k_2\phi)(1-\phi) - k_3\phi - k_4. \tag{6.6}$$

The binding rate resembles the binding of a Min-D in abundance of Min-E in the membrane and the cytoplasm. Here k_1 and k_2 denotes the rate constant of cytoplasmic and Min-D interaction with membrane, k_3 and k_4 denotes the unbinding rate constant of by which membrane Min-D interacts with cytoplasmic components.

6.2.4 Governing equations

The tangential force balance given in Equation (2.27) becomes

$$\begin{aligned}\lambda_{,\alpha} - 4\nu w \nabla H + 2\nu(\nabla \cdot \boldsymbol{d} - \nabla w \cdot \boldsymbol{b}) = \\ - \nabla\sigma\left[k_B T \log\left(\frac{\phi}{1-\phi}\right) - 2\kappa\ell(H - \ell\sigma_s\phi) - \frac{\gamma}{2}(2\phi - 1) - \frac{\gamma}{2\sigma_s}\Delta\phi - \mu_b\sigma_s\right],\end{aligned} \tag{6.7}$$

where λ is the Lagrange multiplier of area incomprehensibility representing the tension in the membrane, $\boldsymbol{b}$ is the curvature tensor, and $\boldsymbol{d} = \frac{1}{2}\left(\nabla \boldsymbol{v} + \nabla \boldsymbol{v}^T\right)$ denotes the rate of strain. The surface incomprehensibility relation is depicted by

$$v^{\alpha}_{;\alpha} = 2wH. \tag{6.8}$$

The shape of the surface is described by the normal force balance relation as given by Equation (2.28), and reduces to

$$\begin{aligned}&\kappa\Delta(H - \ell\sigma_s\phi) + 2k(H - \ell\sigma_s\phi)(2H^2 - K) - 2H\left[k_B T\sigma_s\{\phi\log\phi + (1-\phi)\log(1-\phi)\}\right. \\ &\left. + \kappa(H - \ell\sigma_s\phi)^2 + \frac{\gamma}{2}\phi(1-\phi) + \frac{\gamma}{4}|\nabla\phi|^2\right] - 2\nu\left[\boldsymbol{b} : \boldsymbol{d} - w(4H^2 - 2K) - \mu_b\sigma\right] \\ &= p + 2\lambda H,\end{aligned} \tag{6.9}$$

where $\Delta(\cdot) = \boldsymbol{\nabla}\cdot\boldsymbol{\nabla}(\cdot)$ denotes the surface Laplacian of a scalar variable. The mass conservation of proteins in the membrane given by Equation (2.34) reads as

$$\begin{aligned}\phi_{,t} + \boldsymbol{\nabla}\cdot(\boldsymbol{v}\phi) = {} & \Delta\phi\left[\frac{k_BT}{f}\left(\frac{1}{1-\phi}\right) + \frac{2k\ell^2\sigma_s}{f}\phi - \frac{\gamma}{f}\phi\right] - \phi\left[\frac{2k\ell}{f}\Delta H + \frac{\gamma}{2f\sigma_s}\Delta^2\phi\right] \\ & + \boldsymbol{\nabla}\phi\cdot\left[\boldsymbol{\nabla}\phi\left(\frac{k_BT}{f}\left(\frac{1}{1-\phi}\right)^2 + \frac{2k\ell^2\sigma_s}{f} - \frac{\gamma}{f}\right) - \frac{2k\ell}{f}\boldsymbol{\nabla}H - \frac{\gamma}{2f\sigma_s}\boldsymbol{\nabla}(\Delta\phi)\right] \\ & + \frac{1}{\sigma_s}q(\sigma_b,\phi),\end{aligned} \tag{6.10}$$

where σ_b is obtained from the mass conservation equation of protein at the bulk, as given by

$$\frac{\partial\sigma_b}{\partial t} = -\frac{1}{V}\int_A q(\sigma_b,\phi)dS. \tag{6.11}$$

6.2.5 Non-dimensionalization

We non-dimensionalize the system of equations (Equation (6.7)–Equation (6.10)) using the following reference scales. The characteristic length scale is taken to be the size L of the domain. The scale for membrane tension λ is its mean value λ_0. Velocities are non-dimensionalized by $v_c = \lambda_0 L/\nu$, and we use the diffusive time scale $t_c = L^2/D$. Note that the protein area fraction $\phi = \sigma/\sigma_s$ is already dimensionless. We non-dimensionalize the bulk protein density as $\Phi = \frac{\sigma_s}{V/A}$. The net binding rate is non-dimensionalized as $Q = \frac{qL^2}{D\sigma_s}$. The dimensionless governing equations are given below, where the dimensionless quantities are presented with a tilde. We present dimensionless form of the governing equations for the coupled dynamics in Appendix C.

6.3 Cahn-Hilliard system with binding

In this section we present the conservation equation of proteins on the membrane and at the bulk in presence of binding. We get mass conservation equation of proteins in the plane of the

Table 6.1: List of dimensionless numbers and their definitions in the model of protein binding

Dimensionless Number	Expression	Physical interpretation
$\hat{B}$	$\frac{k_B T}{\kappa}$	$\frac{\text{Thermal energy}}{\text{Bending energy}}$
$\hat{L}$	$\frac{\ell}{L}$	$\frac{\text{Spontaneous curvature length}}{\text{Domain length}}$
$\hat{A}$	$\frac{\gamma}{k_B T}$	$\frac{\text{Aggregation coefficient}}{\text{Diffusion coefficient}}$
$\hat{S}$	$\sigma_s L^2$	$\frac{\text{Domain area}}{\text{Protein footprint}}$
$\hat{T}$	$\frac{2L^2\lambda_0}{\kappa}$	$\frac{\text{Membrane tension energy}}{\text{Bending energy}}$
Pe	$\frac{\lambda_0 L^2}{\nu D}$	$\frac{\text{Advection strength}}{\text{Diffusion strength}}$
$\hat{M}$	$\frac{\mu}{k_B T}$	$\frac{\text{Binding potential}}{\text{Thermal energy}}$
Φ	$\frac{\sigma_b V}{\sigma_s A}$	$\frac{\text{Bulk protein density}}{\text{Saturation density in membrane}}$

membrane (Equation (6.10)) in absence of bending and flow simplifies to

$$\begin{aligned}\phi_{,t} = Q(\Phi,\phi) + \Delta\phi\left[\frac{1}{1-\phi} - \frac{\gamma}{k_B T}\phi\right] - \phi\left[+\frac{\gamma}{2k_B T L^2 \sigma_s}\Delta^2\phi\right] \\ + \boldsymbol{\nabla}\phi\cdot\left[\boldsymbol{\nabla}\phi\left(\frac{1}{(1-\phi)^2} - \frac{\gamma}{k_B T}\right) - \frac{\gamma}{2k_B T L^2\sigma_s}\boldsymbol{\nabla}(\Delta\phi)\right].\end{aligned} \tag{6.12}$$

Here the density of protein Φ at bulk is governed by

$$\frac{\partial\Phi}{\partial t} = -\int_A Q(\Phi,\phi)dA. \tag{6.13}$$

6.3.1 Stability analysis

The linearized equations for perturbation of protein density over a homogeneous steady state density both at the membrane (ϕ_0) and at the bulk (Φ_0) are derived from Equation (6.12)

andEquation (6.13), given by

$$\phi_t' = Q_{,\phi}(\Phi_0,\phi_0)\phi' + Q_{,\Phi}(\Phi_0,\phi_0)\Phi' + \nabla^2\phi'\left[\frac{1}{1-\phi_0} - \hat{A}\phi_0\right] - \phi_0\left[\frac{\hat{A}}{2\hat{S}}\nabla^4\phi'\right], \tag{6.14}$$

and

$$\frac{\partial\Phi'}{\partial t} = -Q_{,\Phi}(\Phi_0,\phi_0)\phi' - Q_{,\Phi}(\Phi_0,\phi_0)\Phi'. \tag{6.15}$$

We take normal modes of ϕ' and Φ'

$$\phi' = \hat{\phi}e^{\alpha t}e^{i2\pi\boldsymbol{k}\cdot\boldsymbol{x}} \quad \text{and} \quad \Phi' = \hat{\Phi}\,e^{\alpha t}. \tag{6.16}$$

Equation (6.14) and Equation (6.15) give the following Jacobian after applying the normal modes given in Equation (6.16)

$$J = \begin{bmatrix} Q_{,\phi} + 4\pi^2k^2\left(\hat{A}\phi_0 - \frac{1}{1-\phi_0}\right) & Q_{,\Phi} \\ -Q_{,\phi} & -Q_{,\Phi} \end{bmatrix}. \tag{6.17}$$

The stability of the system is given by the eigenvalues of the Jacobian, given by

$$\alpha^{\pm} = \frac{1}{2}\left(\mathrm{Tr} \pm \sqrt{\mathrm{Tr}^2 - 4\Delta}\right), \tag{6.18}$$

where

$$\mathrm{Tr} = Q_{,\phi} - Q_{,\Phi} + 4\pi^2k^2\left(\hat{A}\phi_0 - \frac{1}{1-\phi_0}\right) \quad \text{and} \quad \Delta = 4\pi^2k^2(\hat{A}\phi_0 - \frac{1}{1-\phi_0})Q_{,\Phi}, \tag{6.19}$$

are trace and determinant of the Jacobian. Note that the necessary condition for instability is

$$Q_{,\phi} > Q_{,\Phi} - 4\pi^2k^2\left(\hat{A}\phi_0 - \frac{1}{1-\phi_0}\right). \tag{6.20}$$

The last part in Equation (6.20) comes from the aggregation potential which is studied in Chapter 5, and the system can be unstable in absence of the aggregation as well.

6.3.2 Numerical simulation in axisymmetric membranes

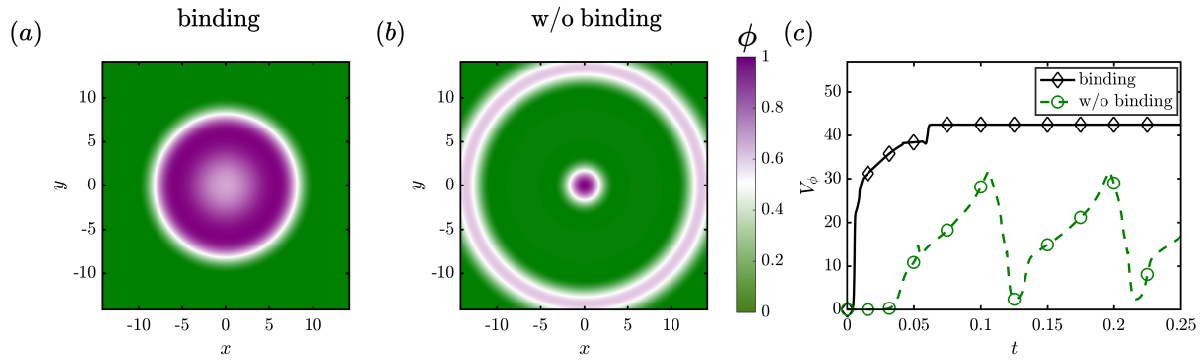

Figure 6.2: Role of protein binding on the localization of proteins in the plane of the membrane. (a) Equilibrium configuration of proteins in the plane of the membrane with protein binding for $\hat{A} = 25$ and $\hat{S} = 320$. (b) Configuration of proteins in the plane of the membrane at long time without protein binding for $\hat{A} = 25$ and $\hat{S} = 320$. (c) Variance $V_\phi \left(= \int (\phi - \phi_{\text{mean}})^2 dA\right)$ of protein distribution with time.

In this section, we present a numerical simulation in an axisymmetric membrane. In these simulations, we considered the proteins which do not have the curvature-inducing effect; therefore, the membrane remains flat. First, we focused on how binding affects the aggregation dynamics of the proteins in Figure 6.2. We notice that in the absence of binding, proteins form an aggregation patch at the center and an annular patch. However, we observe the formation of a single dense patch at the center of the membrane with binding. The most notable difference was in the variance plot. The dynamics of proteins do not achieve a steady state in the absence of binding; instead, the aggregation and diffusion alternate dominance as depicted by the oscillating nature of the variance.

Next, we study the dynamics of protein distribution in the plane of the membrane with the binding of proteins. Figure 6.3 represents the temporal evolution of the protein density in the plane of the membrane in the presence and absence of aggregation potential. We notice here even

without aggregation potential, proteins aggregate, and over a long time aggregate to a single big patch at the center of the membrane. The density of the patch for a long time is higher for $\hat{A} = 25$. In both cases, we notice that aggregation patch forms as an annular ring, and the ring diameter decreases until it becomes a patch at the center. The number of annular rings increases for higher values of $\hat{A}$, which is consistent with the result of Chapter 5, which suggests higher aggregation strength leads to more patches. However, the effect of binding becomes predominant for a long time, and multiple patches merge.

Now we study the effect of aggregation parameters on the protein binding dynamics. In Figure 6.3 we observe the binding dominates over longer time for $\hat{A} = 25$ and $\hat{S} = 320$. Given this result, we explore this behavior in the parameter space of $\hat{A}$ and $\hat{S}$, and notice until what value of $\hat{A}$ and $\hat{S}$ the binding dominates to give an aggregation patch at the center of the membrane. Figure 6.4a depicts the equilibrium configurations of the patches in the plane of $\hat{A}$ and $\hat{S}$. We observe that, for all values of $\hat{A}$ and $\hat{S}$, the distribution of protein reaches a steady state (Figure 6.4b,c), unlike the oscillation we observed in Figure 6.2 in the absence of binding. We see that for lower values of $\hat{A}$ and $\hat{S}$, the binding dominates, and we see a single patch at the center. In the absence of aggregation potential $\hat{A}$, the effect of $\hat{S}$ is insignificant, but for higher values of $\hat{A}$, we see the effect of $\hat{S}$ dominates the equilibrium behavior. Higher values of $\hat{A}$ and $\hat{S}$ give significant deviation from the binding dominated distribution depicted by one big patch at the center. In the variance plot (Figure 6.4b,c), we noticed that as long as the protein patch is concentrated at the center, variance increases with both $\hat{A}$ and $\hat{S}$. However, the variance declines when the patches split into one or more axisymmetric patches.

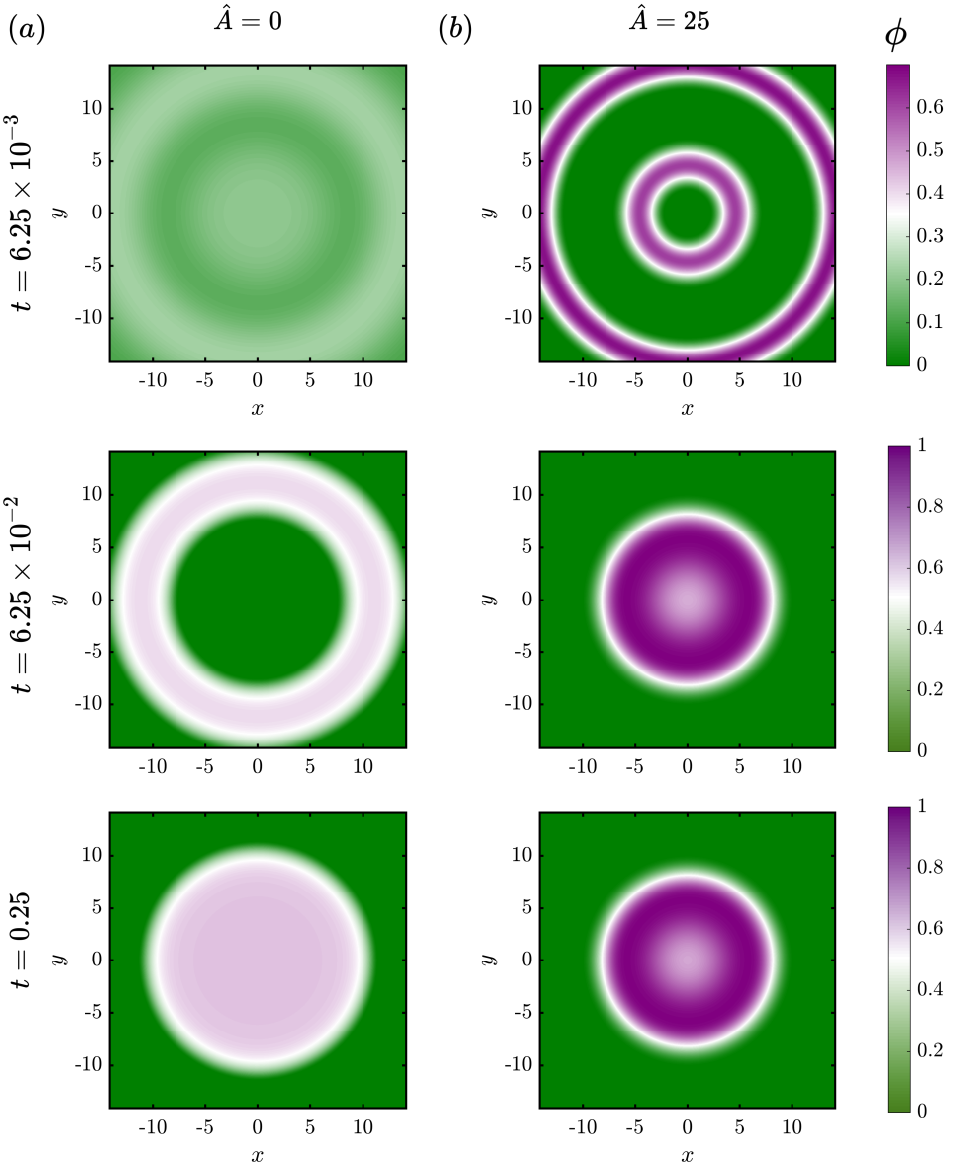

Figure 6.3: Temporal evolution of protein density in the plane of the membrane with binding of protein in absence of bending. (a) Temporal evolution of protein density in the plane of the membrane at three different times in absence of aggregation potential with $\hat{S} = 320$. (a) Temporal evolution of protein density in plane of the membrane at three different times with aggregation potential ($\hat{A} = 25$) with $\hat{S} = 320$.

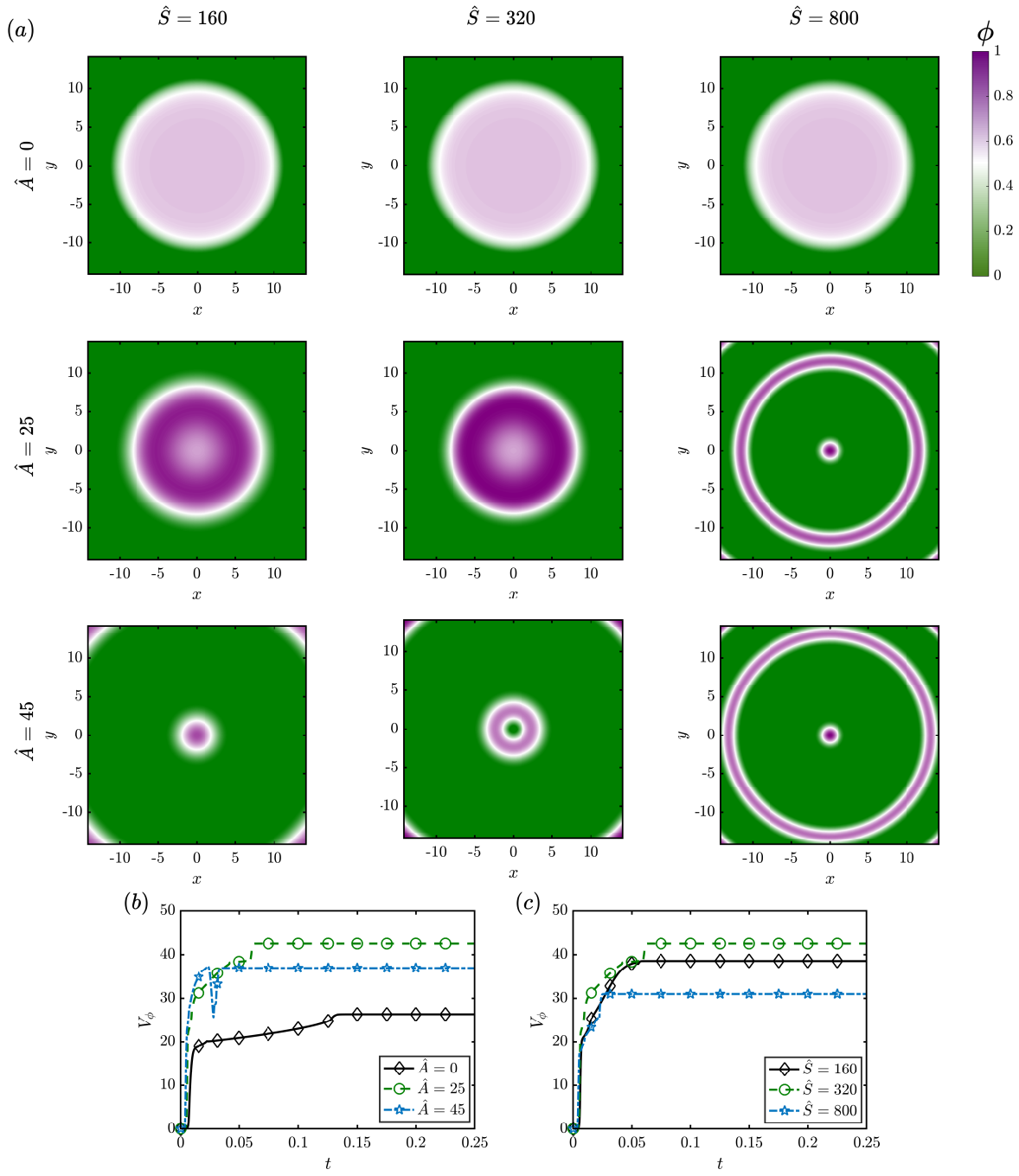

Figure 6.4: Configuration of protein distribution in the plane of the membrane with binding of proteins in the parameter space of $\hat{A}$ and $\hat{S}$, in the absence of membrane bending. (a) Equilibrium protein distribution. (b) Temporal evolution of variance of protein distribution with $\hat{A}$ for $\hat{S} = 320$. (c) Temporal evolution of variance of protein distribution with $\hat{S}$ for $\hat{A} = 25$.

6.4 Coupling with bending and flow with aggregation potential

6.4.1 Stability analysis

In the presence of bending the density perturbation equation in the membrane becomes

$$\phi_t' = Q_{,\phi}(\Phi_0,\phi_0)\phi' + Q_{,\Phi}(\Phi_0,\phi_0)\Phi' + \nabla^2\phi'\left[\frac{1}{1-\phi_0} + \frac{2\hat{L}^2\hat{S}}{\hat{B}}\phi_0 - \hat{A}\phi_0\right] - \phi_0\left[\frac{\hat{L}}{\hat{B}}\nabla^4 z' + \frac{\hat{A}}{2\hat{S}}\nabla^4\phi'\right], \tag{6.21}$$

where $\nabla^4 z'$ comes from the shape equation, given by

$$\nabla^4 z' = 2\hat{L}\hat{S}\nabla^2\phi' + 2\hat{B}\hat{S}\nabla^2 z'\left[\{\phi_0\log\phi_0 + (1-\phi_0)\log(1-\phi_0)\} + \frac{\hat{A}}{2}\phi_0(1-\phi_0) + \frac{\hat{L}^2\hat{S}}{\hat{B}}\phi_0^2\right] + \hat{T}\nabla^2 z'. \tag{6.22}$$

The modified Jacobian of the system is given by

$$J = \begin{bmatrix} Q_{,\phi} + 4\pi^2k^2\left[\hat{A}\phi_0 - \frac{1}{1-\phi_0} - \frac{2\hat{L}^2\hat{S}}{\hat{B}}\phi_0 g(k)\right] - 8\pi^4\phi_0\frac{\hat{A}}{\hat{S}}k^4 & Q_{,\Phi} \\ -Q_{,\phi} & -Q_{,\Phi} \end{bmatrix}. \tag{6.23}$$

Note that the necessary condition for instability becomes

$$Q_{,\phi} > Q_{,\Phi} - 4\pi^2k^2\left[\hat{A}\phi_0 - \frac{1}{1-\phi_0} - \frac{2\hat{L}^2\hat{S}}{\hat{B}}\phi_0 g(k)\right]. \tag{6.24}$$

Similar to Chapter 5, bending here also has a stabilizing effect on the phase separation.

6.4.2 Numerical simulation in axisymmetry membranes

Governing equations in an axisymmetric membrane

In the case of axisymmetry, we reduce the dimensionless form of governing equations in the following simplified form. For bravity, we represent all the dimensionless quantities without tildes. The tangential force balance relation (Equation (C.1)) simplifies to

$$\begin{aligned}\frac{\partial \lambda}{\partial s} - 4w\frac{\partial H}{\partial s} + 2(2\frac{\partial wH}{\partial s} + Kv_s - \frac{\partial w}{\partial s}\frac{\partial \psi}{\partial s}) = -\frac{\partial \phi}{\partial s}\Bigg[\frac{2\hat{B}\hat{S}}{\hat{T}}\log\frac{\phi}{1-\phi} \\ - \frac{4\hat{L}\hat{S}}{\hat{T}}(\tilde{H} - \hat{L}\hat{S}\phi) - \frac{\hat{A}\hat{B}\hat{S}}{\hat{T}}(2\phi - 1) - \frac{\hat{A}\hat{B}}{\hat{T}}\Delta\phi - \frac{2\hat{M}\hat{B}\hat{S}}{\hat{T}}\Bigg]\end{aligned} \tag{6.25}$$

where $\Delta(\cdot) = \frac{1}{r}\frac{\partial}{\partial s}\left(r\frac{\partial(\cdot)}{\partial s}\right)$, denotes the Laplacian operator of a scalar field. The continuity (Equation (C.2)) is represented here as

$$\frac{1}{r}\frac{\partial (rv^s)}{\partial s} = 2wH. \tag{6.26}$$

Subsequently, we present the shape equation (Equation (C.3)) as two first order ODEs

$$\begin{aligned}&\frac{1}{r}\frac{\partial L}{\partial s} + 2(H - \ell\sigma_0 L\sigma)(2H^2 - K) - 2\hat{B}\hat{S}\tilde{H}\Bigg[\phi\log\phi + (1-\phi)\log(1-\phi) + \frac{\hat{A}}{2}\phi(1-\phi) \\ &+ \frac{\hat{A}}{4\hat{S}}\left|\frac{\partial\phi}{\partial s}\right|^2 - \hat{M}\phi\Bigg] + \frac{\gamma}{2k_BT}\phi(1-\phi) + \frac{\gamma}{4K_BT\sigma_s L^2}\left|\frac{\partial\phi}{\partial s}\right|^2 - \frac{\mu_b}{k_BT}\phi\Bigg] \\ &- \hat{T}\Bigg[\psi_s\frac{\partial(rv^s)}{\partial s} + \frac{\sin\psi\cos\psi v^s}{r^2} - w(4H^2 - 2K)\Bigg] = p + \hat{T}\lambda H\end{aligned} \tag{6.27}$$

with

$$\frac{L}{r} = \left[\frac{\partial H}{\partial s} - \hat{L}\hat{S}\frac{\partial\sigma}{\partial s}\right]. \tag{6.28}$$

The diffusion equation of protein (Equation (C.4)) reduces to the following form:

$$\begin{aligned}\phi_{,t} + Pe\,\frac{\partial(\tilde{v^s}\phi)}{\partial s} &= \Delta\phi\left[\frac{1}{1-\phi} + \frac{2\hat{L}^2\hat{S}}{\hat{B}}\phi - \hat{A}\phi\right] - \phi\left[\frac{2\hat{L}}{\hat{B}}\Delta H + \frac{\hat{A}}{2\hat{S}}\Delta^2\phi\right] \\ &+ \frac{\partial\phi}{\partial s}\left[\frac{\partial\phi}{\partial s}\left(\frac{1}{(1-\phi)^2} + \frac{2\hat{L}^2\hat{S}}{\hat{B}} - \hat{A}\right) - \frac{2\hat{L}}{\hat{B}}\frac{\partial\tilde{H}}{\partial s} - \frac{\hat{A}}{2\hat{S}}\frac{\partial(\Delta\phi)}{\partial s}\right] + Q(\phi,\Phi).\end{aligned} \tag{6.29}$$

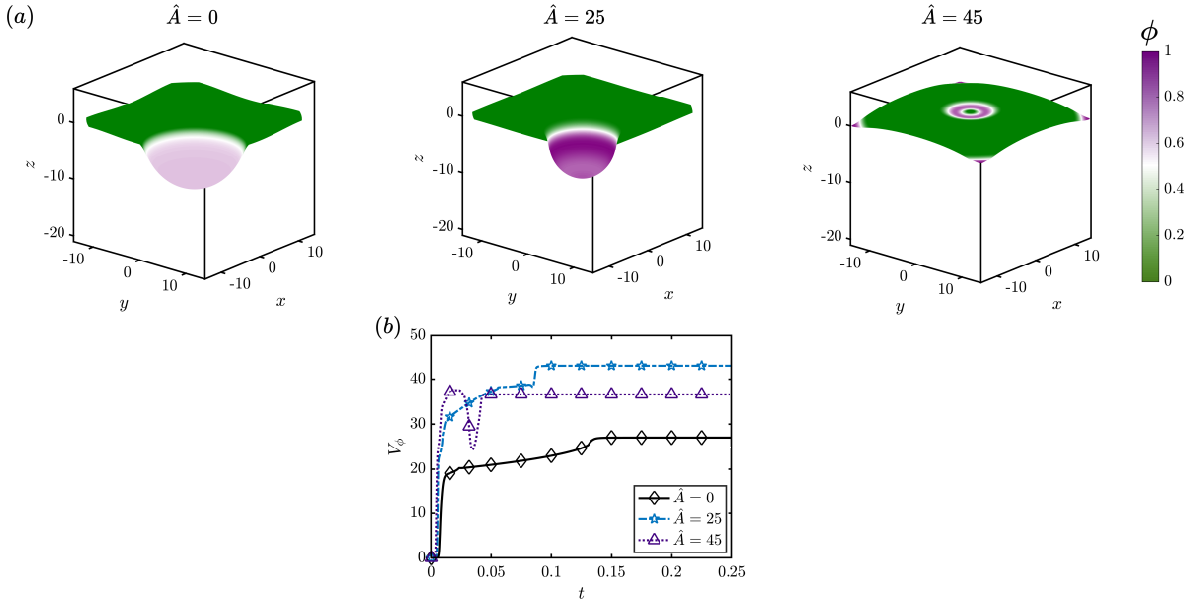

Figure 6.5: Configuration of the protein aggregate and the membrane shape as a function of aggregation strength $\hat{A}$ with the binding of curvature-inducing proteins. (a) Configuration of membrane at long time for $\hat{S} = 2000$, $\hat{L} = 0.002$ and three different values of $\hat{A}$. (b) Variance of proteins density with time.

Results

We solved the system of equations (Equation (6.25) to Equation (6.29)) in axisymmetry with bending and in-plane viscous flow, with the numerical methods described in the Section 3.4.3. Here we exclusively study the membrane shapes and how the shape affects the protein distributions. Figure 6.5 shows the membrane shape and associated distribution of the curvature-inducing proteins at long time in presence of binding. We notice here the aggregation patterns follow

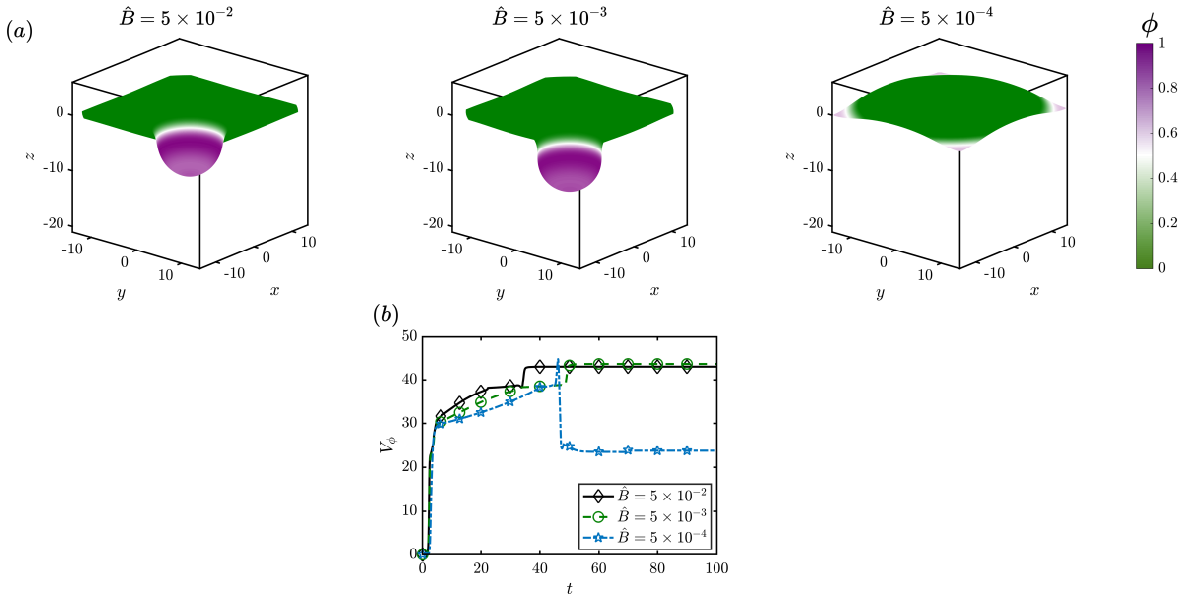

Figure 6.6: Configuration of the protein aggregate and the membrane shape as a function of membrane stiffness $\hat{B}$ with the binding of curvature-inducing proteins. (a) Configuration of membrane at long time for $\hat{S} = 2000$, $\hat{L} = 0.002$ and three different values of $\hat{B}$. (b) Variance of proteins density with time.

the behavior without bending. Patches become denser at higher value of $\hat{A}$, but if we increase $\hat{A}$ further, the effect of aggregation potential dominates the binding dynamics, gives multiple annular patches, which gives lower bending of the membrane. When there are multiple patches across the membrane, the net effect of curvature-inducing effect is weaker compared to the case when proteins are localized at the center. This results a lower deformation in the membrane. The results in this figure do not show a strong curvature-driven feedback on the aggregation as we observed in Chapter 5.

Thereafter we increased the effect of bending to study the curvature-driven feedback in the protein dynamics. Figure 6.6 presents the effect of $\hat{B}$ on the protein dynamics and resultant shape. Recall that $\hat{B}$ is the ratio of thermal energy to the bending rigidity, and aggregation and diffusion is scaled with the thermal energy. Therefore, lower values of $\hat{B}$ denotes the stiffer membrane, and here we achieved by lowering temperature. As the linear stability suggested the dimensionless number $\hat{B}$ has a strong influence on the stability, and as in Chapter 5 we notice for a

nearly planner membrane how the bending limits the aggregation. Panel (a) shows the distribution of protein at long time for three different values of $\hat{B}$. We noticed that if we decrease $\hat{B}$ one order of magnitude lower corresponding to room temperature, the dynamics of proteins remains almost unchanged. However, one more order of magnitude decrease leads to a massive change in the proteins distribution. The protein patch moves towards the boundary, and that causes lower deformation to the membrane. In the variance plot in panel (b) we see a sudden drop for this case, indicating diffusion of the patch after a threshold time. At long time the distribution of proteins reaches a steady state.

6.5 Discussion

The role of protein binding in the localization of proteins and inducing local deformation to the membrane is crucial for many biophysical processes. In this present work, we have developed a comprehensive theory of binding of proteins along with the in-plane transport and curvature generation. We considered a well-mixed bulk system that indicates the diffusion coefficient in bulk as much more dominant compared to the planner diffusion. We have considered one particular binding rate of proteins to the membrane from the cytoplasm and explored the effect of bending and protein-protein interaction. The resulting system of equations completely describes the dynamics of membrane deformation protein distributions. We have further presented a reduced system in the absence of bending and flow to demonstrate how the curvature-induced interaction can alter phase separation dynamics. We compared the systems to linear stability and numerical simulation studies in axisymmetry. We observed that the aggregation of proteins could occur due to binding alone, and lower values of $\hat{A}$ and $\hat{S}$ assist the aggregation. However, more elevated values of $\hat{A}$ or $\hat{S}$ alter the wavenumber of the patch, resulting in a reduction in the extent of aggregation. We further detected curvature-induced feedback in the binding dynamics. Higher spontaneous curvature limits the formation of the patch. The results support the stability analysis

and are consistent with our past findings.

The effect of binding and unbinding was studied in experiments [85], theory [84, 82], and numerical simulations [83] in multiple occurrences. The majority of the theoretical models did not consider interaction forces among proteins, and the resulting system of equations resembles the diffusion-driven instability as seen in a Turing pattern. Additionally, this study improves the a-priori assumption of the binding rate as a curvature-dependent binding and unbinding rate and demonstrates curvature dependence as an outcome of strong coupling. Furthermore, the curvature-coupling in the large deformation captures a more substantial effect as opposed to small-deformation analysis [83], and energy landscape analysis in spherical geometries [82]. Our model mimics the experimental setup by providing conservation equations of binding of curvature-inducing proteins, both in the membrane and at the bulk, and resultant shape of the membrane.

6.6 Acknowledgments

I would like to acknowledge my co-author Prof. Padmini Rangamani. This chapter is primarily based on the manuscript in preparation authored by Arijit Mahapatra and Padmini Rangamani. The dissertation author was the primary author of the work. I would also like to thank Prof. David Saintillan for critical feedback.

Chapter 7

Snap-through transition in membrane tube formation

7.1 Introduction

Plasma membrane tubes are omnipresent in cellular membranes and in the membranes of intracellular organelles, and play crucial roles in biophysical functions (Figure 7.1) like trafficking, ion transport, and cellular motility [186]. The formation of plasma membrane tubes can be due to forces acting on the membrane due to the cytoskeleton or motor proteins [187, 50, 188] or by the induced curvature of membrane-bound proteins [189]. The force-mediated tubular protrusion has been studied extensively theoretically and with experiments on giant unilamellar vesicles (GUV) [188]. However, the mechanics of protein-induced tube formation and the corresponding energy landscape are poorly understood. Here, we present a mathematical framework to model tubular protrusions mediated by proteins that induce anisotropic spontaneous curvature. We use a free energy that accounts for membrane bending due to anisotropic spontaneous curvature, and the free energy is then minimized to get the shape of the membrane. We demonstrate our model with numerical simulations in an axisymmetric framework to study the role of the parameters,

such as bending rigidity, membrane tension, area of curvature inducing proteins, and spontaneous curvature of the proteins. We observed that the membrane undergoes a shape transition from a dome-like shape to a long tube along a specific region in the parameter space. Such a transition is similar to a snap-through instability. We study the energy landscape across this shape transition and identify the critical values of dimensionless numbers across the shape transition. Finally, we perform a stability analysis for a simplified geometry to find the necessary condition of this shape transition and predicted threshold values of dimensionless numbers.

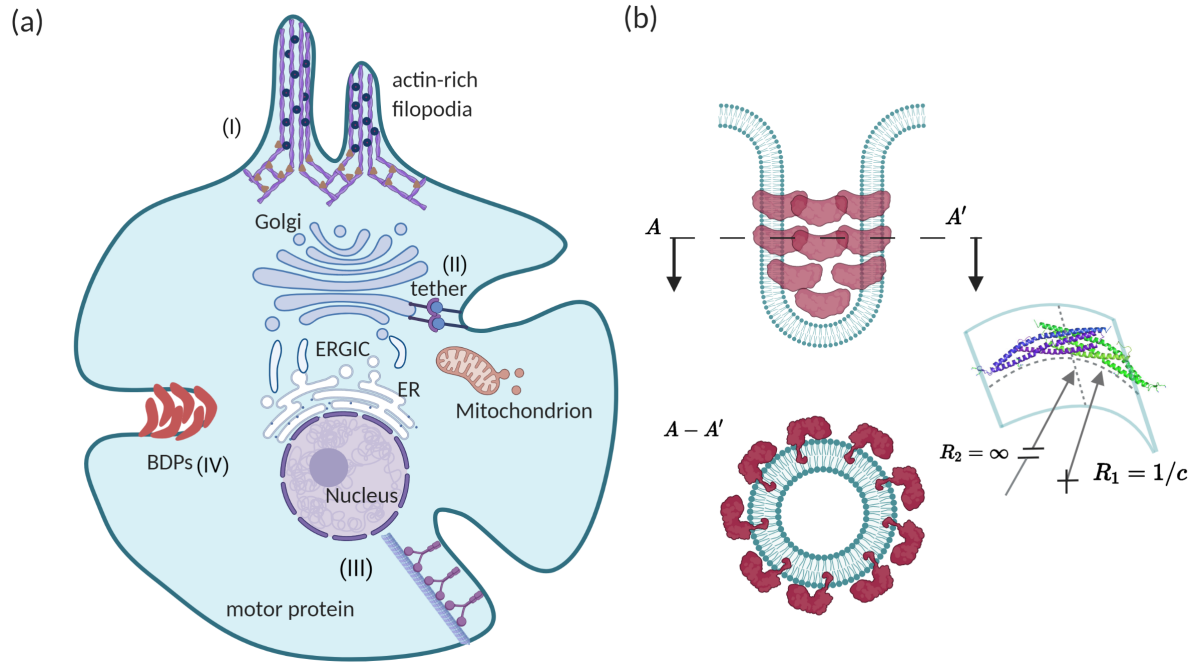

Figure 7.1: Schematic of protein-induced tube formation on cellular membranes. a)Mechanisms of tube formation in cellular membranes, (I) Tubes can be formed due to forces exerted on the membrane by the cytoskeleton, e.g. filopodial protrusion by actin filaments, (II) localized forces such as tethers and motors (III) can also lead to the formation of tubes. Tubules can also be formed by proteins, such as, BAR-domain proteins (BDPs) (IV). BDPs are know to form cylindrical tubules by inducing curvature on the lipid bilayer. In this work, we focus on modeling tubule-formation due to proteins such as these. (b) Schematic depicting proteins that have anisotropic curvatures assembled on the cylindrical portion of a membrane tube. The structure of a typical BAR-domain protein dimer induces two different curvatures in the parallel and perpendicular direction.

Table 7.1: Summary of the notation used in the model protein-induced tube formation

Notation	Description	Unit
W	Free energy density of the membrane	$\mathrm{pN/nm}$
κ	Bending modulus of the membrane	$\mathrm{pN-nm}$
κ_d	Deviatoric modulus of the membrane	$\mathrm{pN-nm}$
$\boldsymbol{n}$	Surface normal	1
$\boldsymbol{\zeta}$	Orientation vector of proteins	1
$\boldsymbol{\mu}$	Orientation vector of protein ($\boldsymbol{\mu}=\boldsymbol{n})\times\boldsymbol{\zeta}$	1
$a_{\alpha\beta}, a^{\alpha\beta}$	Metric tensor and its contravarient	–
$b_{\alpha\beta}, b^{\alpha\beta}$	Curvature tensor and its contravarient	–
s	Arclength of the membrane	nm
ψ	Angle made by surface tangent with the horizontal direction	1
H	Mean curvature	nm^{-1}
D	Deviatoric curvature	nm^{-1}
C	Spontaneous mean curvature	nm^{-1}
D_0	Spontaneous deviatoric curvature	nm^{-1}
$\boldsymbol{T}$	Surface traction	$\mathrm{pN/nm}$
p	Normal pressure acting on the membrane	$\mathrm{pN/nm^2}$
λ	Membrane tension	pN/nm

7.2 Model development

BAR-domain proteins (BDP) are one-dimensional curved proteins, as shown in Figure 1, which induce anisotropic curvature to the membrane [69, 70, 190]. If the curvatures c_1 and c_2 are induced in the two principal directions, the spontaneous mean (C_0) and deviatoric (D_0) can be estimated as

$$C_0 = \frac{c_1 + c_2}{2}, D_0 = \frac{c_1 - c_2}{2}. \tag{7.1}$$

Note that if we consider the induced principal curvature c_1 equal to the curvature of the BDP's (curvature c in Figure 7.2b), the other principal curvature c_2 will depend on the orientation of the proteins. In the example shown in Figure 7.2b, BDPs orient circumferentially along a tube, c_2 becomes zero in this case. For a common orientation, the spontaneous mean (C_0) and deviatoric curvature (D_0) can be estimated from the curvature of the proteins and their orientation angle [191, 42].

7.2.1 Assumptions

We first assume membrane thickness and change in thickness are negligible compared to bending, and thus a continuum description is valid in this case. The membrane is elastic in bending, and the bending rigidity is assumed to be constant in the region. We consider an incompressible patch of the membrane where the force balance relation depicts equilibrium shapes at rest. We assume that the spontaneous mean and deviatoric curvature induced by membrane-bound BDPs are divided into two region (Figure 7.2):

i. at the tip of the coat, a spontaneous mean curvature cap $C_0 = c$ with zero spontaneous deviatoric curvature ($D_0 = 0$) (region 1 in Figure 7.2)

ii. the rest of the coat with equal values of spontaneous mean and deviatoric curvature $C_0 = D_0 = c/2$ (region 2 in Figure 7.2)

Note that this type of spontaneous curvature distribution arises when BDPs axially at the tip of the tube and circumstantially rest of the tubular area. Such a type of orientation follows from the minimization of bending energy of the BAR proteins. However, the spontaneous curvature at the tip of the coat might be induced by other curvature-generating proteins.

7.2.2 Free Energy of the membrane

We consider a free energy of the membrane similar to the elastic energy given by the Helfrich hamiltonian [36] with the modification of the deviatoric components [191, 42, 190]

$$W = \kappa(H - C_0)^2 + \kappa_d(D - D_0)^2, \tag{7.2}$$

where κ, κ_d are the bending rigidities, H and D are the mean and deviotoric curvature of the membrane, C_0, D_0 are the spontaneous curvatures induced by proteins.

7.2.3 Governing equations

At the equilibrium configuration, an element on the membrane follows the local stress balance relation given by[55, 111, 64]

$$\boldsymbol{T}^{\alpha}_{;\alpha} + p\boldsymbol{n} = \boldsymbol{0}, \tag{7.3}$$

where, p is normal pressure on the membrane and $\boldsymbol{T}$ is the surface stress tensor. Equation 7.3 resolves to two separate force balance relations (see section 1.2 in the supporting information) in the tangential and normal direction of the membrane. The tangential force balance relation reduces to [111, 64, 11, 190]

$$\lambda_{,\alpha} = -W_{,\alpha|exp}, \tag{7.4}$$

where λ is the Lagrange multiplier for area constraints, physically it represents the tension in the plane of the membrane. $W_{,\alpha|exp}$ in Equation 7.4 represents the explicit dependence of coordinate on energy [111, 64] . The normal force balance relation depicts the equilibrium shape of the membrane as is given by [190]

$$\begin{gathered}\frac{1}{2}[W_D(\zeta^{\alpha}\zeta^{\beta} - \mu^{\alpha}\mu^{\beta})]_{;\beta\alpha} + \frac{1}{2}W_D(\zeta^{\alpha}\zeta^{\beta} - \mu^{\alpha}\mu^{\beta})b_{\alpha\gamma}b^{\gamma}_{\beta} + \Delta(\frac{1}{2}W_H) + \\ (W_K)_{;\beta\alpha}(2Ha^{\beta\alpha} - b^{\beta\alpha}) + W_H(2H^2 - K) + 2H(KW_K - W) - 2H\lambda = p.\end{gathered} \tag{7.5}$$

Here $\boldsymbol{\zeta}$ is the direction of orientation of the BDP's, $\boldsymbol{\mu} = \boldsymbol{n} \times \boldsymbol{\zeta}$, with $\boldsymbol{n}$ as the unit surface normal [190].

7.2.4 Governing equations in axisymmetry

In polar coordinates the geometry of the membrane can be parameterized by

$$\boldsymbol{r}(r, z, \theta) = \boldsymbol{r}(s, \theta), \tag{7.6}$$

where s is the arclength, and θ angle in the azimuthal direction. In the limit of axisymmetry, $\frac{\partial(\cdot)}{\partial\theta} = 0$ and the membrane can be parameterized by the arclength s only, as shown in Figure 7.2. In axisymmetry, the tangential force balance relation in Equation (7.4) reads

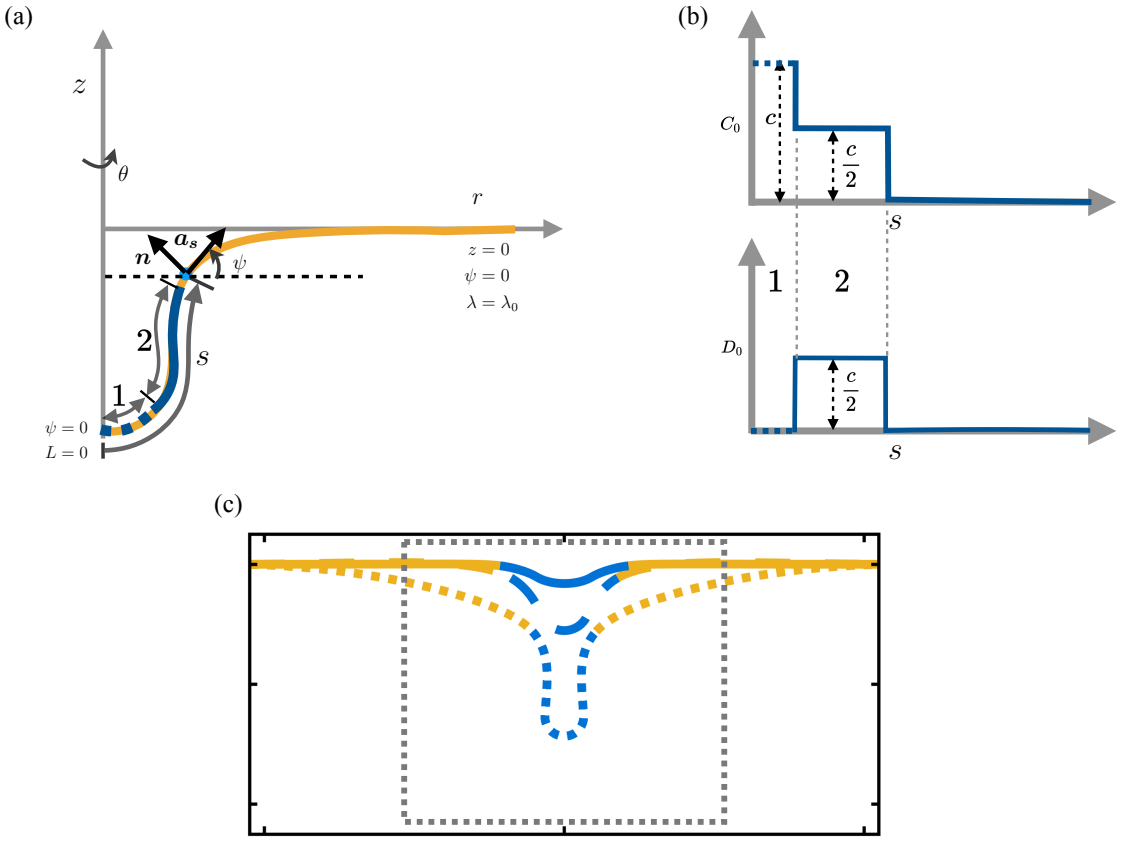

Figure 7.2: Membrane representation in axisymmetry with protein distribution area and boundary conditions. (a) Solution domain with protein coat and boundary conditions. (b) Distribution of spontaneous mean and deviatoric curvature on the membrane along the arclength. (c) The membrane deformation configuration with protein distributions, the dashed-lines shows the region in the $r-z$ plane we focused to show subsequent figures.

$$\lambda' = 2\kappa(H - C_0)C_0' + 2\kappa_d(D - D_0)D_0', \tag{7.7}$$

where $(\cdot)' = \frac{\partial(\cdot)}{\partial s}$. The normal force balance in Equation (7.4) simplifies to

$$p = \frac{L'}{r} + 2\kappa(H - C_0)\left(2H^2 - K\right) - 2H\left(W + \lambda - 2\kappa_d D(D - D_0)\right) \tag{7.8}$$

where,

$$L/r = \left[\kappa(H - C_0) - \kappa_d(D - D_0)\right]' - 2\kappa_D(D - D_0)\frac{\cos\psi}{r}, \tag{7.9}$$

denoting the normal component of traction on the membrane. Note that a form of these equations presented in [190] but the definition of L is missing the last term in equation Equation (D.32). We explained the mistake in detail in the section 2.1 of the supporting information. The detailed derivations are shown in Appendix D.1 and Appendix D.2.

7.2.5 Numerical schemes

We solve the system of equations (Equation (D.33) to Equation (D.35)) numerically to get the equilibrium shape of the membrane for a coat of protein at the center of an axisymmetric area patch. The solution domain is presented in Figure 7.2a, along with the input protein coat and the boundary conditions. The protein coat includes both the spontaneous mean curvature cap and a combination of mean and deviatoric spontaneous curvature in the rest annular region (Figure 7.2b). Note that we introduce a shape variable ψ which denotes the angle made by the tangent from its radial plane. The membrane is clamped at the domain boundary, where both the displacement and the angle ψ vanish. The membrane tension is also prescribed at the boundary. At the center, ψ is taken to be zero, which indicates the smoothness at the center of the membrane. L is also taken as zero, indicating no pulling force acting at the center. To solve the system of equations, we used MATLAB bvp4c, a finite difference-based ODE solver with fourth-order accuracy. We used a nonuniform grid ranging from 1000 to 10000 points, with the finer grid towards the center. We presented the numerical results in the highlighted region of Figure 7.2c for subsequent figures.

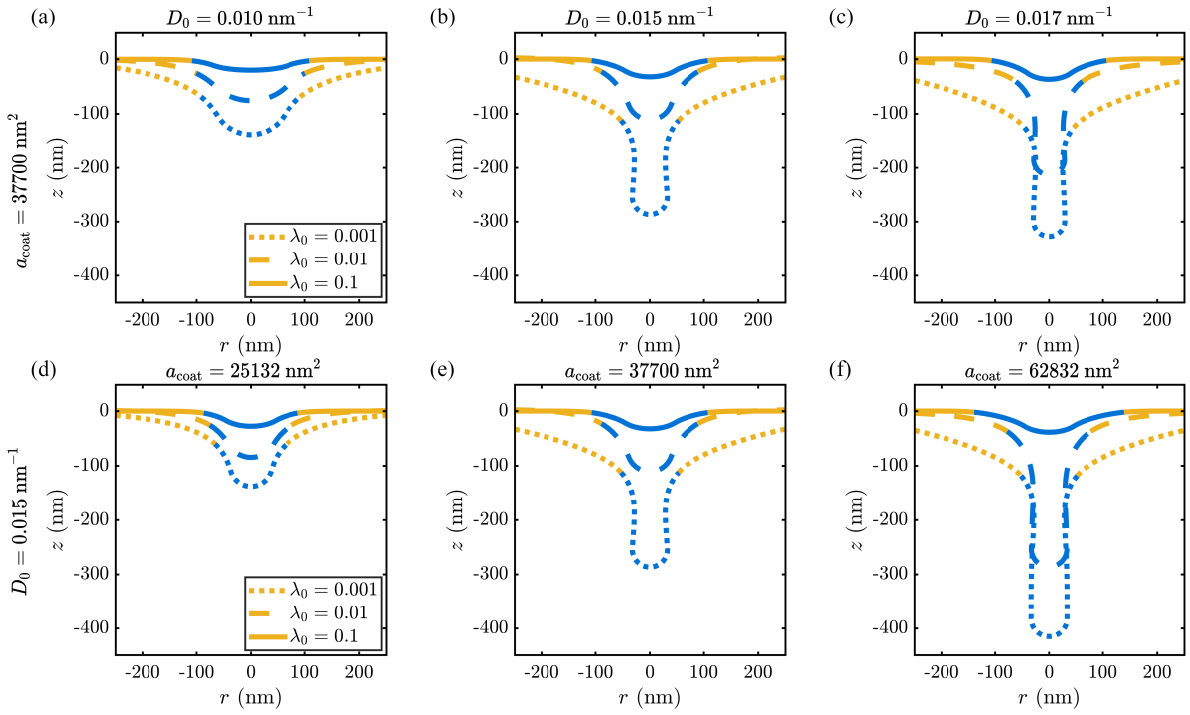

Figure 7.3: Membrane tension limits the tubulation of the membrane. (a,b,c) Equilibrium shape of the membrane for 3 different spontaneous deviatoric curvatures, compared with three different values of tension (0.001, 0.01, 0.1 pN/nm). Fixed values are taken for area of the protein coat is taken as 25132 nm^2 and bending rigidity of the membrane 42 pN $\cdot$ nm. (d,e,f) Equilibrium shape of the membrane for 3 different protein coats areas, compared with three different values of tension (0.001, 0.01, 0.1 pN/nm). Fixed values are taken for spontaneous deviatoric curvature as 0.015 nm^{-1} and bending rigidity of the membrane 42 pN $\cdot$ nm.

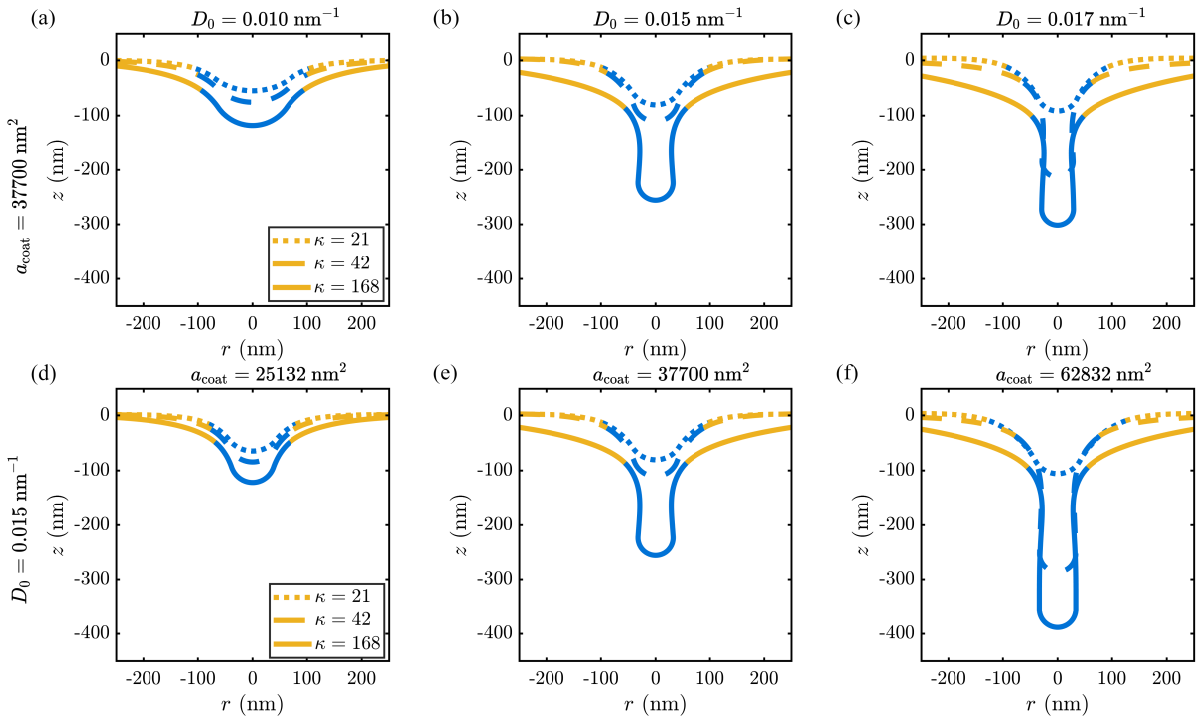

Figure 7.4: Bending rigidity assists in the tubulation of the membrane. (a,b,c) Equilibrium shape of the membrane for 3 different spontaneous deviatoric curvatures, compared with three different values of bending rigidities (21, 42, 168 pN – nm). Fixed values are taken for area of the protein coat is taken as 25132 nm^2 and membrane tension 0.01 pN/nm. (d,e,f) Equilibrium shape of the membrane for 3 different protein coats areas, compared with three different values of bending rigidities (21, 42, 168 pN – nm). Fixed values are taken for spontaneous deviatoric curvature as 0.015 nm^{-1} and membrane tension 0.01 pN/nm.

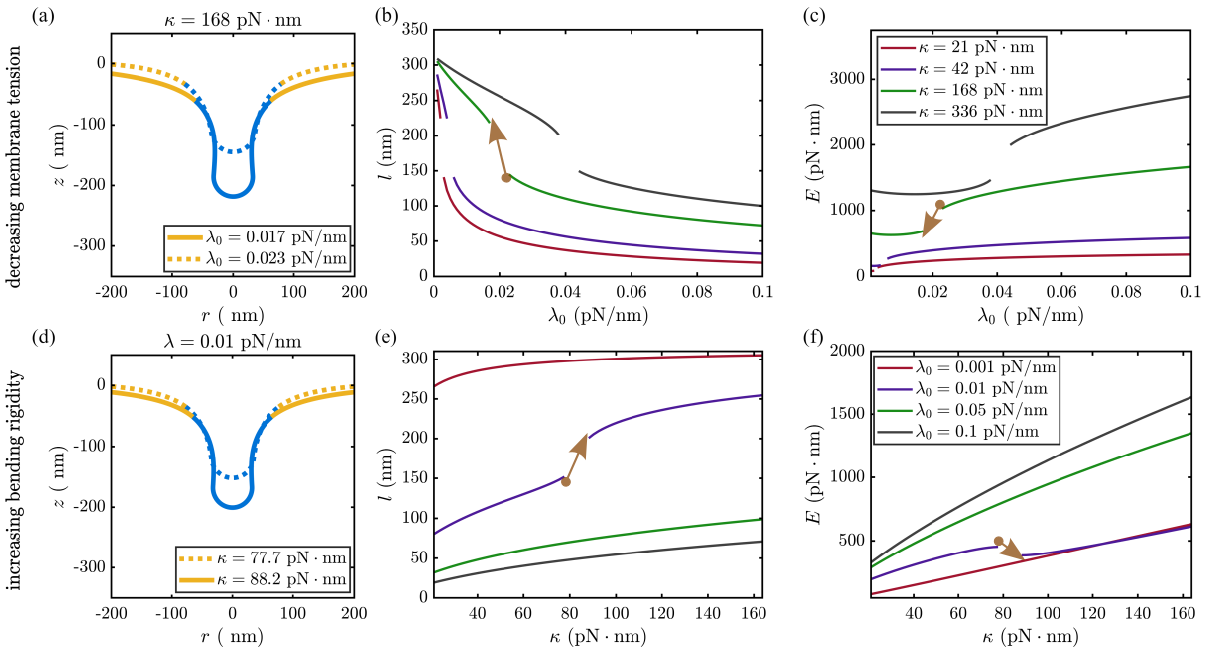

Figure 7.5: Snap through instability and the role of membrane tension and bending rigidity. (a,b,c) Snap through instability caused by decreasing membrane tension membrane tension with $a_{\text{coat}} = 3.77 \times 10^4$ nm^2 and $D_0 = 0.015$ nm^2 with the landscape of energy and membrane deformation. Both the length of the tubular structure (b) and the bending energy (c) experienced discontinuities across the snap through, and are shown for 4 different values of bending rigidity κ. The morphology of the membrane changed from a tent to a tube shape (a). (d,e,f) Snap through instability caused by increasing bending rigidity κ with $a_{\text{coat}} = 3.77 \times 10^4$ nm^2 and $D_0 = 0.015$ nm^2 with the landscape of energy and membrane deformation. The length of the tubular structure (e) and the bending energy (f) are shown with bending rigidity for for different values of membrane tension. For$\lambda_0 = 0.01$ pN/nm a discontinuity is observed, the morphology of the membrane changed from a tent to a tube shape (d).

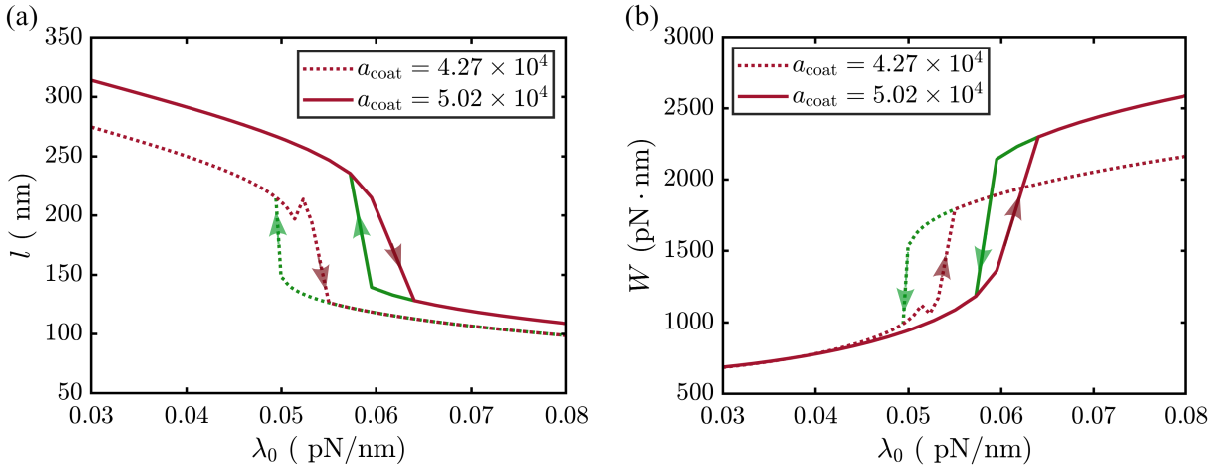

Figure 7.6: Forward and backward transition in tube morphology. (a) Transition of tube length in the direction of increasing and decreasing membrane tension for $D_0 = 0.017$ nm^{-1} and $\kappa = 168$ pN$\cdot$nm and two different values of coat area of proteins. (b) Transition of bending energy in the direction of increasing and decreasing membrane tension for $D_0 = 0.017$ nm^{-1} and $\kappa = 168$ pN$\cdot$nm and two different values of coat area of proteins.

7.3 Results

We conducted numerical simulations across the parameter space of bending rigidity κ, membrane tension λ, spontaneous curvatures C_0, D_0 and the coat areas of proteins a_{coat}. Note that C_0 and D_0 are not independent in our case. We show the variation with D_0 for the subsequent results; C_0 relates to D_0 as described in the section. Note that the value of D_0 is constant in the cylindrical region of the protein coat (region 2 in Figure 7.2a). We use this constant value as a parameter and refer to D_0 moving forward. Figure 7.3 represents the shape of the membranes as a function of membrane tension λ_0 for different values of spontaneous curvatures (a-c) and coat areas (d-f). We notice that for higher values of coat areas and spontaneous curvatures, membranes shapes are found in long rigid tubes for membrane tension of 0.01 and 0.001 pN/nm. However, for higher values of membrane tension (0.1 pN/nm), the membrane remains almost flat for all the values of protein coat area and spontaneous curvature. We see a similar behavior for bending rigidity κ on shape. The higher values of κ favor the tubular shape, whereas for lower κ membrane remains almost flat. The deformation behavior with κ is counterintuitive as

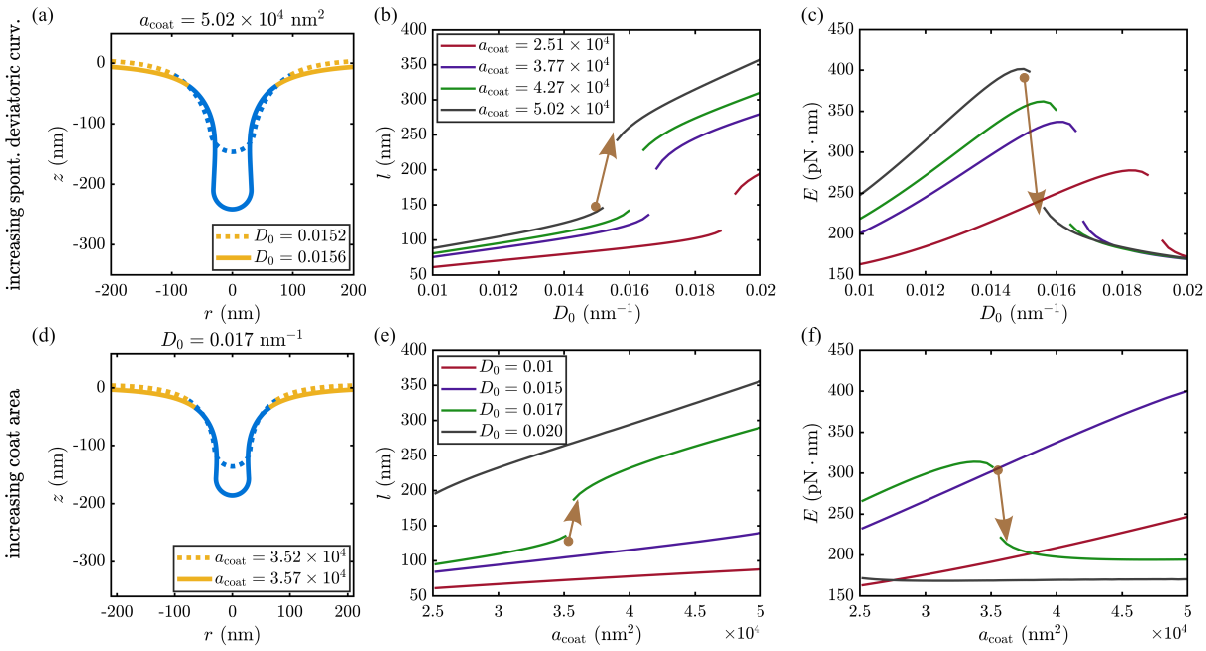

Figure 7.7: Snap through instability and the role of spontaneous deviatoric curvature and the coat area. (a,b,c) Snap through instability caused by increasing spontaneous deviatoric curvature with $\kappa = \kappa_d = 42$ pN/nm and $\lambda_0 = 0.01$ pN/nm^2 with the landscape of energy and membrane deformation. Both the length of the tubular structure (b) and the bending energy (c) experienced discontinuities across the snap through, and are shown for 4 different values of bending rigidity κ. The morphology of the membrane changed from a tent to a tube shape (a). (d,e,f) Snap through instability caused by increasing coat area of protein with $\kappa = \kappa_d = 42$ pN/nm and $\lambda_0 = 0.01$ pN/nm^2 with the landscape of energy and membrane deformation. The length of the tubular structure (e) and the bending energy (f) are shown with bending rigidity for for different values of membrane tension. For $\lambda_0 = 0.01$ pN/nm a discontinuity is observed, the morphology of the membrane changed from a tent to a tube shape (d).

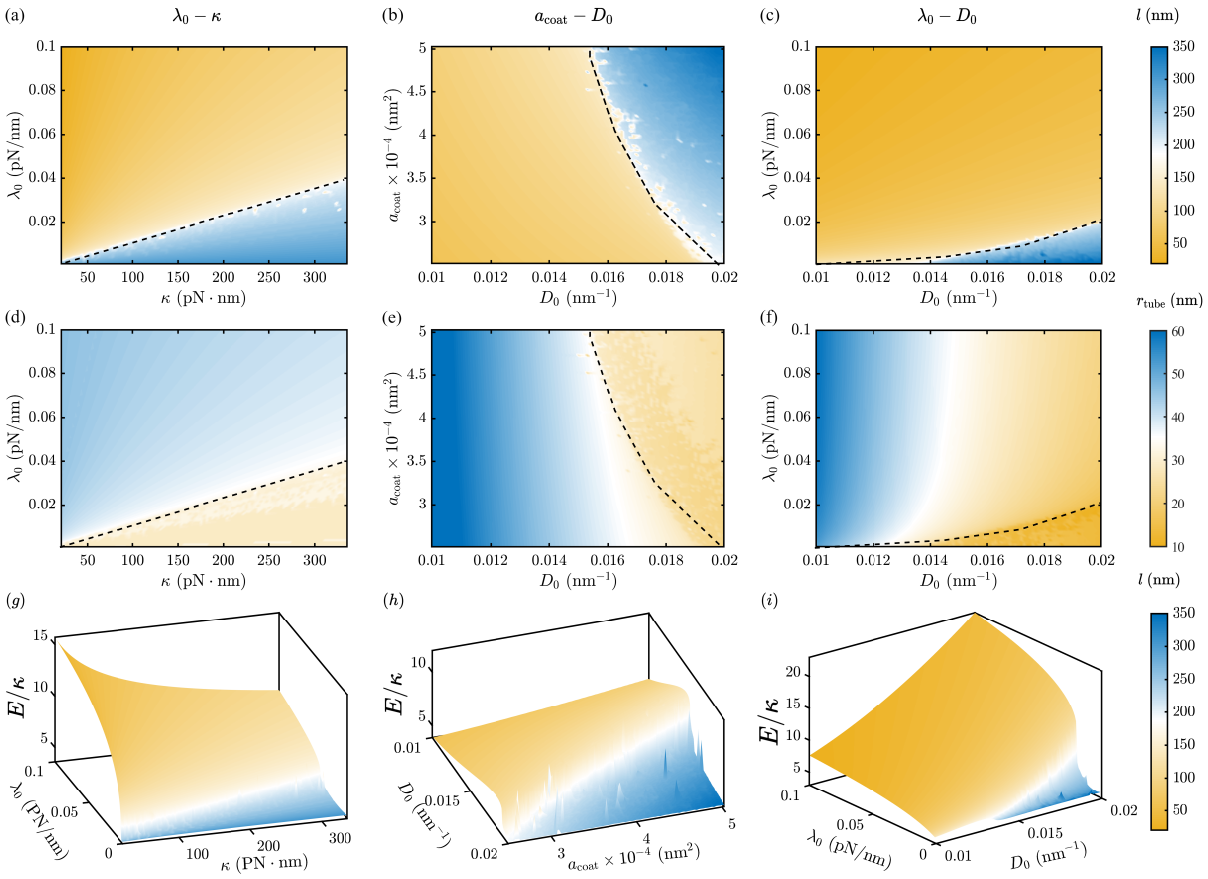

Figure 7.8: Phase-space diagram of protein-induced tube formation. Variation of length in the parameter space of λ_0 and κ (a), a_{coat} and D_0 (b), and λ_0 and D_0 (c). Variation of tube radius in the plane of λ_0 and κ (d, a_{coat} and D_0 (e), and λ_0 and D_0 (f). Landscape of bending energy in the parameter space of λ_0 and κ (g), a_{coat} and D_0 (h), and λ_0 and D_0 (i).

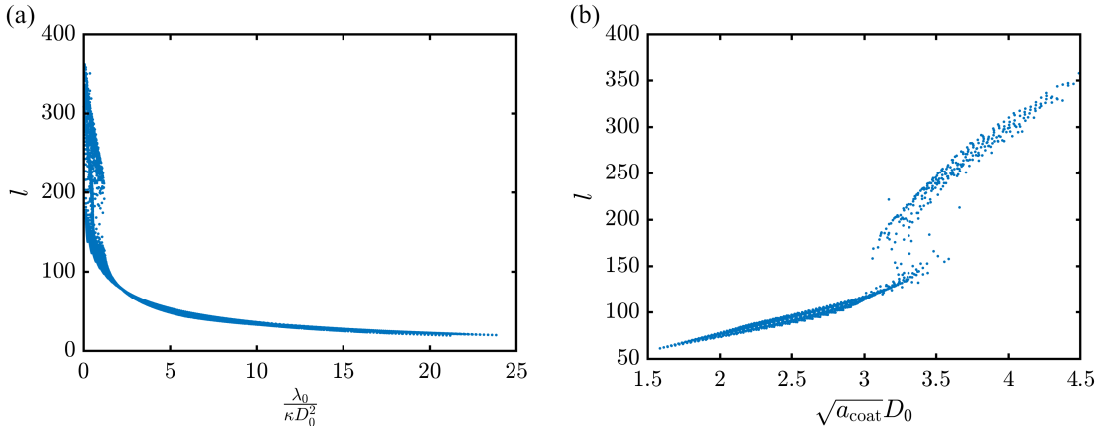

Figure 7.9: Variation of tube length as a function of dimensionless numbers. (a) Variation of length with dimensionless number $\frac{\lambda_0}{\kappa D_0^2}$ for protein coat area of 3.77×10^4 nm^2. (b) Variation of length with the dimensionless number $\sqrt{a_{\text{coat}}}D_0$ for bending rigidity κ of 42 pN$\cdot$nm and tension λ_0 of 0.01 pN/nm.

more bending rigidity implies a stiffer membrane, which undergoes lower deformation. However, in the case of deformation with spontaneous curvatures, the intrinsic shape of the membrane is the tension-free membrane, the curvature of which follows the local spontaneous curvature. Therefore, a membrane with lower tension will give the shape close to a tube, and with increasing tension, the shape will deviate from the tube shape and becomes flatter. In such circumstances, the membrane with more bending rigidity will offer more resistance to deviate from the tubular configuration, and thus we see a long tube for higher κ and vice versa.

Next, we studied the role of each four parameters on the shape, and we varied each separately, keeping the other parameter constant. In Figure 7.5 we varied membrane tension and bending rigidity and focused on the transition of shape from a tent to a tube. We noticed that the transition from a tent is similar to a snap-through transition. We observed the shape transition with decreasing membrane tension (a-c) and increasing bending rigidity. Panel (a) represents the shape of the membrane before and after the transition for decreasing membrane tension with bending rigidity of 168 pN/nm. Panel (b) shows the length of the tube as a function of λ_0 for different values of κ, and panel (c) shows the corresponding bending energy. We see a sudden change in the transition from a tent to a tube shape in both cases. Panel (d)-(f) shows the plots for

transition shapes, tube length, bending energy, and increasing bending rigidity. In panel (e) and (f), we noticed for some values of λ_0 the variations of tube length and the bending energy are smooth. There is no shape transition in this range of κ: a tube remains a tube, and a tent stays as a tent in this range.

The sudden transition of membrane shape resembles many of the snap-through behaviors for elastic deformations. Many of those transitions are demonstrated by saddle-node bifurcations. However, the stability analysis became immensely complex since the equilibrium shape is curved in our present problem. Furthermore, a closed-form solution of the equilibrium deformation is also not available close to the transition. Instead, we have taken an alternative approach. In this snap-through transition, we expect a pair of saddle-node bifurcations. Therefore we expect a pair of stable equilibrium solutions in the neighborhood of the transition. We have solved the system of equations for a parameter with an increasing and decreasing direction to find that. We gave our solver a sense of direction by providing an initial guess of the solution corresponding to the last value of the parameter. We showed a similar study for the membrane tension, and the corresponding tube length and the energy are shown in Figure 7.6. Close to transition, we see two different solutions of shape, and there is a lag in the tube length and bending energy when we change λ_0 in forward and backward directions. Note that the numerical solution is not smooth near the transition region, and for some points, the solution does not converge to a stable solution.

Next we explore the snap-through transition with parameters of spontaneous curvature D_0 and a_{coat}. Panel (a)-(c) shows the transition for increasing spontaneous curvature D_0 with different coat areas. We see a sharp increase in tube length in panel (b) and corresponding bending energy drops at the transition, as shown in panel (c). Figure (a) shows the shapes across the transition for $a_{\text{coat}} = 5.02 \times 10^4$. Panel (d)-(f) shows the similar snap-through transition with the coat area of proteins for four different values of spontaneous curvatures D_0. We see a sharper transition only for $D_0 = 0.017\text{nm}^{-1}$, for which the energy declines along with the transition. However, the rest of D_0 do not show any transition, a tube remains as a tube as a tent remains as a tent in these

cases. The corresponding energies are also monotonic.

Next, we show a phase diagram for tube length, tube radius, and bending energy in the parameter space of $\lambda_0 - \kappa$, $a_{\text{coat}} - D_0$, and $\lambda_0 - D_0$. We notice a sharper transition of tube length in the parameter space. For example, we see a linear transition boundary in the parameter space of $\lambda_0 - \kappa$. However the transition boundary becomes parabolic in $a_{\text{coat}} - D_0$, and $\lambda_0 - D_0$. The tube radius follows a similar behavior of length, and the longer tube corresponds to the tube of smaller radius. We scaled the energy with the bending rigidity κ to show the energy landscape. We see that there is a downhill bending energy across the transition line. The bending energy corresponding to the long tubes is less compared to the shorter tubes. This comes from the fact that the long tubes are less deformed than their base state.

We seek dimensionless numbers from these numerical simulations that could describe the solution in reduced parameter space. We present such an analysis in Figure 7.9. Panel (a) shows that the tube length collapse to a line for the dimensionless number $\frac{\lambda_0}{\kappa D_0}$. These simulations are performed for different values of λ_0, κ, and D_0, keeping coat area a_{coat} constant. We further see that close to the length of 200 nm there, the points are less denser. This corresponds to the transition region. In panel (b) we present the tube length for different values of a_{coat} and D_0, and see that the length merges to a line when we plot them with dimensionless number $\sqrt{a_{\text{coat}}} D_0$. Here also, we see the transition region along $150 - 200$ nm, depicted by less dense points.

7.4 Discussion

In the paper, we have presented a theoretical formulations of tube formation due to protein-induced anisotropic curvature. In the theoretical formulation we considered a continuum the free energy of membrane bending, where we included the effect of orientation of proteins by giving the specified values of spontaneous curvature. We derived a system of equations by minimizing the free energy in an axisymmtric geometry. The derivation did exist in the literature

with an error which led to the introduction of a numerical force term, and that was included in the subsequent studies. Here, we have redefiend the quantity L so that it gives normal bending stress, gives a natural boundary condition for the boundary-value problem. We solved the system of equations in wide range of parameters and observed a snap-through transition, which corresponds to the change in shape from a tent to a tube. The snap-through transition is omnipresent across all the parameters, and that led us to the finding of a dimensionless number with which the shape variables collapse. Furthermore, we observed a downhill of energy across this transition, suggesting how the bending energy landscape favors the transition of shape.

The idea that deviatoric curvature favors tubular protrusion is proposed in a series of studies [190, 192, 193], where a cylindrical membrane is coated with proteins that induce deviatoric curvature. However, formation of a tube from a flat membrane due to anisotropic curvature alone, has not been studied, except the study by Perutkova et al. [193] that showed tubular shapes in such cases are energetically favorable. Secondly, the snap-through transition was observed via systematic numerical simulations, and a hysteresis-like behavior was also reported. In the study of the snap-through in formation of a bud and force pulled tube, the role of tension was investigated in detail. In addition to finding the role of tension we have extended the study to find the role of bending rigidity as well, which finds its implication in the biophysical processes where changes of composition and saturation leads to changes in bending rigidity.

This model has numerous implication in the biophysical problems related to tubular structures generated by proteins, such as formation of t-tubule in cardiac myocytes, cristae formation in mitochondria, and Drosophila cellularization. Transition of shapes from a tent to a tube and the dissolve of tube to a tent has been observed in biological systems. For example t-tubules in cardiac myocytes disintegrated in a culture, and disappearance of cristae is also observed under certain conditions. Furthermore, these disintegration is noticed in many disease states. The snap-through transition across parameter space could demonstate this transition in a qualitative way.

7.5 Acknowledgments

I would like to acknowledge my co-author Prof. Padmini Rangamani. This chapter is primarily based on the manuscript in preparation authored by Arijit Mahapatra and Padmini Rangamani. The dissertation author was the primary author of the work. The author also like to thank Prof. David Saintillan for critical feedback.

Chapter 8

Concluding remarks and future directions

In this thesis, we presented a comprehensive theory of the coupled transport phenomena that occurs in membrane-protein interaction: out of plane bending of the membrane, in-plane lipid flow and resulting advection-diffusion transport of protein, and interaction among proteins leading to the formation of aggregates. The system of equations we obtained gives the equation of motion of the membrane shape and spatio-temporal distribution of the proteins. Moreover, this study considers the viscous flow of lipid, which offers completeness in the expression of membrane tension as opposed to the inviscid study. We presented a linear stability analysis to predict the parameter space that favors the formation of protein aggregates from homogeneously distributed proteins. Subsequently, we demonstrated numerical simulations in the small deformation in a square domain and large deformation in the limit of axisymmetry. We observed the role of curvature-driven feedback and in-plane velocity field in the dynamics of protein distribution in a diffusion-dominated regime in Chapter 4. The aggregation strength $\hat{A}$ and the relative size number $\hat{S}$ have critical roles in forming aggregates, while the influence of curvature-driven feedback depicted by dimensionless spontaneous curvature $\hat{L}$ inhibits the aggregation of proteins as shown in Chapter 5. Our linear stability analysis could also verify the role of bending in limiting the formation of protein aggregates. However, in the case of protein binding, aggregates can form in

the absence of aggregation potential, where the aggregation landscape changes in the influence of protein-protein interaction as depicted by $\hat{A}$ and $\hat{S}$ as shown in Chapter 6. However, the effect of curvature-driven feedback limiting the aggregation is consistent among the studies.

The problem we discussed in Chapter 7 demonstrates the snap-through transition of the membrane shape caused by localized anisotropic curvature-inducing proteins. We formulate free energy of bending from a Helfrich-like Hamiltonian with the modification of the anisotropic term. We corrected the derivation of the system of equations over the existing model in the literature and introduced a modified expression of normal bending stress that uses natural boundary conditions. The resultant equations for shape are solved in an axisymmetric geometry at equilibrium. The parametric analysis shows that the snap-through transition of shape is always present across all the parameters. Furthermore, we noticed a hysteresis-like behavior that resembles the saddle-node and subcritical pitchfork bifurcation in elastic structures. We identified two dimensionless groups with which the shape behaviors collapse in lines and dictate the snap-through transition.

This study serves the need for a comprehensive coupled model of transport phenomena that bridges the gap between the study of dynamics of shape in an inviscid membrane and viscous flow in a fixed membrane. Furthermore, we mitigated the assumption of localized proteins in generating membrane shape providing a detailed mechanism of protein aggregation. The dynamics presented in the study break the limitation of equilibrium study and show the role of coupling clearly. This kind of approach has the potential to understand fast processes compared to relaxation time, such as ultrafast endocytosis. Our numerical implementations are focused on a simplified geometry, which offers an understanding of the role of individual physical processes in the coupled system. The stability analysis we provided across the chapters helps us interpret the numerical simulation even with better clarity.

This study can further be generalized and extended in many directions. The interaction with the bulk flow and transport of species at bulk can be included in this model with the help of boundary integral techniques. Next, the restrictions of idealized geometry can be overcome

by considering realistic geometry obtained from the microscopic data, and discrete differential geometry can be used to model such non-idealized membranes. Further, the thermal fluctuation of the membrane can also be included to study the more realistic dynamics. In such a case, a discrete model of protein-lipid interaction would be helpful in understanding the dynamics of protein aggregation more accurately. Finally, the transport of proteins on the membrane can be extended to a multi-component reaction-diffusion system, which we see in signaling pathways.

Appendix A

Analytical justification and validations of numerical simulation

A.1 Analytical justification for the flat plane as the equilibrium solution

Our 1D simulations in §4.3.2 show that at steady state the protein distribution reaches a uniform distribution while the string approaches the flat configuration. Here, we rationalize this result and prove theoretically that the flat configuration with uniform protein density is indeed an exact solution. To this end, we consider the arc-length parametrization and write the energy Lagrangian as

$$\mathcal{L} = \int [k(H-C)^2 + \lambda]\,\mathrm{d}s = \int [k(\psi_s - C)^2 + \lambda]\,\mathrm{d}s. \tag{A.1}$$

In the above relation, ψ is the angle made by the string with the horizontal direction and s is the arc-length. The curvature, in this case, is given by ψ_s. The tangential force balance reads

$$2k[\psi_s - C(s)]C'(s) = \lambda_s, \tag{A.2}$$

which provides an equation for the string tension λ for a given shape and spontaneous curvature. For a uniform protein density, the spontaneous curvature is also uniform: $C(s) = C_0$, and equation (A.2) then implies a uniform tension $\lambda(s) = \lambda_0$ everywhere in the domain. The Lagrangian then simplifies to

$$\mathcal{L} = \int_{-L/2}^{L/2} \left[(\psi_s - C_0)^2 + \Lambda_0\right] \mathrm{d}s, \quad \text{with} \quad \Lambda_0 = \frac{\lambda_0}{k}. \tag{A.3}$$

Here, we have taken the domain to be $-L/2 \leq s \leq L/2$, and we assume the following boundary conditions at both ends:

$$y(-L/2) = y(L/2) = 0, \qquad \psi(-L/2) = \psi(L/2) = 0. \tag{A.4}$$

Without loss of generality, we can consider symmetric deformations with respect to $s = 0$, and seek the solution for ψ_s as a Fourier cosine series of the form

$$\psi_s = a_0 + \sum_{n=1}^{\infty} a_n \cos \frac{2n\pi s}{L}. \tag{A.5}$$

Substituting this series into equation (A.3) yields

$$\begin{aligned} \mathcal{L} &= \int_{-L/2}^{L/2} \left[k\left(a_0 + \sum_{n=1}^{\infty} a_n \cos \frac{2n\pi s}{L} - C_0 \right)^2 + \lambda_0 \right] \mathrm{d}s \\ &= \frac{L}{2} \sum_{n=1}^{\infty} k a_n^2 + L(kC_0^2 + \lambda_0). \end{aligned} \tag{A.6}$$

We find that $\mathcal{L}$ is independent of a_0. Minimizing $\mathcal{L}$ with respect to the Fourier coefficients leads to $a_i = 0$ for $i \neq 0$. We therefore find that $\psi_s = a_0$, which integrates to $\psi = a_0 s + b$. Using the boundary conditions (A.4), we obtain

$$\psi(s) = 0, \tag{A.7}$$

which indicates that the flat configuration is the equilibrium solution in this case.

A.2 Validation of algorithm for pressure-Poisson equation

In §4.3, we solved the coupled membrane tension and velocity for the case of linear Monge by solving the pressure-Poisson equation with the help of the integral representation of equation (4.27). Here, we present a validation of this method and compare the result with the Stokes-Neumann system [1]. Recall the governing equations for the fluid flow in the present case:

$$\tilde{\boldsymbol{\nabla}} \cdot \tilde{\boldsymbol{v}} = 2\tilde{w}\tilde{H}, \tag{A.8}$$

$$\begin{aligned} \tilde{\boldsymbol{\nabla}}\tilde{\lambda} + \tilde{\nabla}^2\tilde{\boldsymbol{v}} + \tilde{\boldsymbol{\nabla}}(\tilde{\boldsymbol{\nabla}} \cdot \tilde{\boldsymbol{v}}) - 4\tilde{w}\tilde{\boldsymbol{\nabla}}\tilde{H} - 2\tilde{\boldsymbol{\nabla}}\tilde{w} : \tilde{\boldsymbol{\nabla}}\tilde{\boldsymbol{\nabla}}\tilde{z} = \\ \tilde{\boldsymbol{\nabla}}\tilde{\sigma}\left[\frac{2\hat{C}\hat{B}}{\hat{T}}\tilde{\nabla}^2\tilde{z} - \frac{4\hat{C}^2\hat{B}^2}{\hat{T}}\tilde{\sigma} - \frac{2\hat{C}}{\hat{T}}\log\left(\frac{\tilde{\sigma}}{\tilde{\sigma}_s}\right)\right]. \end{aligned} \tag{A.9}$$

The velocity field $\boldsymbol{v}$ can be written as a Helmholtz decomposition:

$$\tilde{\boldsymbol{v}} = \tilde{\boldsymbol{\nabla}}\phi + \tilde{\boldsymbol{\nabla}} \times \tilde{\boldsymbol{\zeta}} = \tilde{\boldsymbol{v}}_d + \tilde{\boldsymbol{u}}, \tag{A.10}$$

where $\tilde{\boldsymbol{v}}_d$ is the curl-free and $\tilde{\boldsymbol{u}}$ is divergence-free. In particular, the continuity equation (A.8) becomes $\tilde{\boldsymbol{\nabla}} \cdot \tilde{\boldsymbol{v}}_d = 2\tilde{w}\tilde{H}$. Now, substituting $\tilde{\boldsymbol{v}} = \tilde{\boldsymbol{u}} + \tilde{\boldsymbol{v}}_d$ into the governing equations (A.8)–(A.9) for the fluid flow yields the modified system of equations:

$$\tilde{\boldsymbol{\nabla}} \cdot \tilde{\boldsymbol{u}} = 0, \tag{A.11}$$

$$\tilde{\boldsymbol{\nabla}}\tilde{\lambda} + \tilde{\nabla}^2\tilde{\boldsymbol{u}} + \tilde{\boldsymbol{f}} = 0, \tag{A.12}$$

where,

$$\begin{aligned} \tilde{\boldsymbol{f}} = 2\tilde{\boldsymbol{\nabla}}(2\tilde{w}\tilde{H}) - 4\tilde{w}\tilde{\boldsymbol{\nabla}}\tilde{H} - 2\tilde{\boldsymbol{\nabla}}\tilde{w} : \tilde{\boldsymbol{\nabla}}\tilde{\boldsymbol{\nabla}}\tilde{z} \\ -\tilde{\boldsymbol{\nabla}}\tilde{\sigma}\left[\frac{2\hat{C}\hat{B}}{\hat{T}}\tilde{\nabla}^2\tilde{z} - \frac{4\hat{C}^2\hat{B}^2}{\hat{T}}\tilde{\sigma} - \frac{2\hat{C}}{\hat{T}}\log\left(\frac{\tilde{\sigma}}{\tilde{\sigma}_s}\right)\right]. \end{aligned} \tag{A.13}$$

Equations (A.12)–(A.11) constitute a inhomogeneneous Stokes problem with body force $\tilde{\boldsymbol{f}}$. We solve it here with boundary conditions $\tilde{\boldsymbol{u}}_\infty \to \boldsymbol{0}$ and $\tilde{\lambda}_\infty \to 1$ at infinity. In that case, the velocity and pressure are simply obtained using the boundary integral equations [194]

$$\tilde{\boldsymbol{u}}(\tilde{\boldsymbol{x}}) = \int_\Omega \mathcal{G}(\tilde{\boldsymbol{x}} - \tilde{\boldsymbol{x}}_0) \cdot \boldsymbol{f}(\boldsymbol{x}_0)\, \mathrm{d}A(\tilde{\boldsymbol{x}}_0), \tag{A.14}$$

$$\tilde{\lambda}(\tilde{\boldsymbol{x}}) = 1 + \int_\Omega \Pi(\tilde{\boldsymbol{x}} - \tilde{\boldsymbol{x}}_0) \cdot \boldsymbol{f}(\boldsymbol{x}_0)\, \mathrm{d}A(\tilde{\boldsymbol{x}}_0), \tag{A.15}$$

where $\mathcal{G}$ and $\boldsymbol{\Pi}$ are the velocity and pressure Green's functions for two-dimensional Stokes flow and are given by:

$$\begin{aligned} \mathcal{G}(\tilde{\boldsymbol{x}}) &= \frac{1}{4\pi}\left(\frac{\tilde{\boldsymbol{x}}\tilde{\boldsymbol{x}}}{|\tilde{\boldsymbol{x}}|^2} - \boldsymbol{I}\log|\tilde{\boldsymbol{x}}|\right), \\ \boldsymbol{\Pi}(\tilde{\boldsymbol{x}}) &= -\frac{1}{2\pi}\frac{\tilde{\boldsymbol{x}}}{|\tilde{\boldsymbol{x}}|^2}. \end{aligned} \tag{A.16}$$

Figure A.1 compares the membrane tension profile $\tilde{\lambda}$ obtained in figure 4.3(a) for a single patch with the solution obtained using the Stokes-Neumann formalism. We find that the relative error is well below 4% everywhere in the domain (a). The two membrane tension profiles overlap over most of the domain except for a small deviation near the center (b).

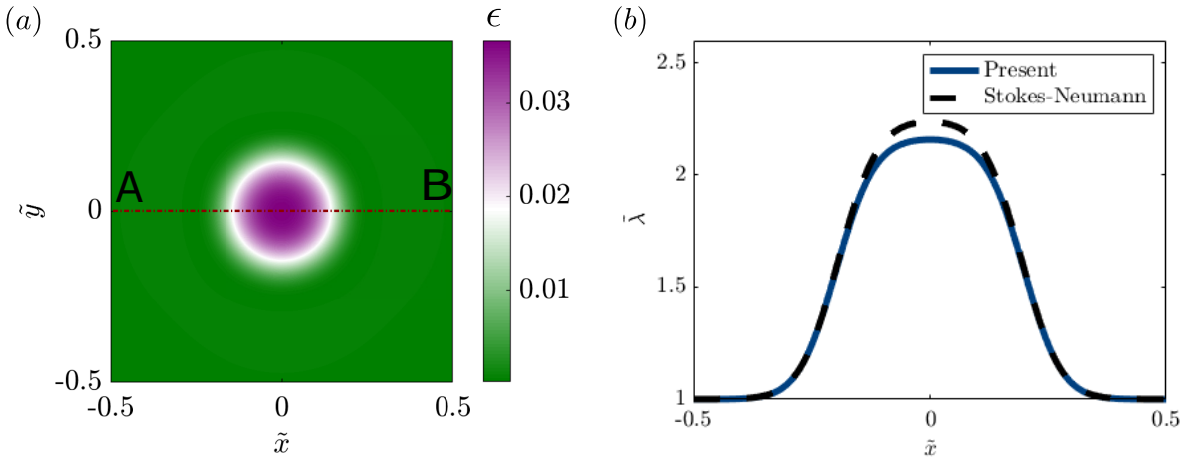

Figure A.1: Comparison between membrane tension calculated using the present model and a Stokes-Neumann formulation [1]. (*a*) Relative error $\varepsilon = (\lambda - \lambda_{SN})/\lambda_{SN}$ in the membrane tension for the case of single patch of protein (figure 4.3(*a*)) at time $\tilde{t} = 5 \times 10^{-3}$, (*b*) Membrane tension distribution along line AB shown in (a) for the present model and Stokes-Neumann solution.

Appendix B

Details of mathematical modeling and numerical simulations of protein aggregation

B.1 Model development

Here we present the governing equation derived from Section 2.3 specific to Chapter 5 that focuses on the transport of curvature-inducing proteins and curvature-driven feedback. Further, we used Gibbs notations to describe the governing equations.

B.1.1 Stress tensor on a surface

The stress tensor $\mathbf{\Sigma}$ represents the state of stress at any location of the membrane and includes both the in-plane normal and shear stresses as well as out-of-plane shear stress due to bending. Each column of the stress tensor $\mathbf{\Sigma}$ constitutes the traction vector on the curve drawn on

the membrane, known as the stress vector, and is represented as

$$\boldsymbol{\Sigma}^{\alpha} = N^{\alpha\beta}\boldsymbol{a}_{\beta} + S^{\alpha}\boldsymbol{n}, \tag{B.1}$$

where $\boldsymbol{N}$ is the surface stress tensor, $\boldsymbol{S}$ represents the shearing force due to bending, and a_{β} (for $\beta = 1,2$) represents the surface tangent vector normal to the curve. The local equilibrium of forces, in the tangential and normal directions, is given by [108]

$$\nabla \cdot \boldsymbol{N} - \boldsymbol{S} \cdot \boldsymbol{b} = 0, \tag{B.2}$$

$$\nabla \cdot \boldsymbol{S} + \boldsymbol{N} : \boldsymbol{b} + p = 0, \tag{B.3}$$

with

$$\boldsymbol{N} = \boldsymbol{\zeta} + \boldsymbol{\pi} + \boldsymbol{b} \cdot \boldsymbol{M} \quad \text{and} \quad \boldsymbol{S} = -\nabla \cdot \boldsymbol{M}. \tag{B.4}$$

Here, $\boldsymbol{\zeta}$ and $\boldsymbol{M}$ are the elastic stress and moment tensors, $\boldsymbol{b}$ is the curvature tensor, and $\boldsymbol{\pi}$ is the viscous stress tensor. The elastic stress and moment tensors can be obtained from the energy density for an incompressible membrane as [108, 88]

$$\begin{aligned} \boldsymbol{\zeta} &= -2\kappa(H - \ell\sigma)\boldsymbol{b} - 2\bar{\kappa}K\boldsymbol{a} - \xi\boldsymbol{a}, \\ \boldsymbol{M} &= \kappa(H - \ell\sigma)\boldsymbol{a} + \bar{\kappa}\left(2H\boldsymbol{a} - \boldsymbol{b}\right), \end{aligned} \tag{B.5}$$

where ξ is the Lagrange multiplier that imposes the incompressibility constraint and $\boldsymbol{a}$ is the metric tensor of the surface. The surface tension λ is related to ξ with the following expression [108]

$$\lambda = -(\xi + W). \tag{B.6}$$

The viscous stresses obey the constitutive relation [109]

$$\boldsymbol{\pi} = 2\nu\left[\boldsymbol{d} - w\boldsymbol{b}\right]. \tag{B.7}$$

Here,

$$\boldsymbol{d} = \left(\nabla\boldsymbol{v} + \nabla\boldsymbol{v}^T\right)/2, \tag{B.8}$$

is the rate-of-strain tensor expressed in terms of the velocity field $\boldsymbol{v}$ (see [109, 112, 88] for details). w is the normal velocity of the surface, given by

$$w = \boldsymbol{n}\cdot\boldsymbol{r}_t, \tag{B.9}$$

where $\boldsymbol{r}$ is the position vector of a material point on the surface.

B.1.2 Dimensionless governing equations

Here we summarize the governing equations for the coupled dynamics of the system in the dimensionaless form. The tangential force balance equation becomes

$$\begin{aligned}\nabla\tilde{\lambda} - 4\tilde{w}\nabla\tilde{H} + 2(\nabla\cdot\tilde{\boldsymbol{d}} - \nabla\tilde{w}\cdot\tilde{\boldsymbol{b}}) \\ = -\nabla\phi\left[\frac{2\hat{B}\hat{S}}{\hat{T}}\log\frac{\phi}{1-\phi} - \frac{4\hat{L}\hat{S}}{\hat{T}}(\tilde{H} - \hat{L}\hat{S}\phi) - \frac{\hat{A}\hat{B}\hat{S}}{\hat{T}}(2\phi-1) - \frac{\hat{A}\hat{B}}{\hat{T}}\Delta\phi\right],\end{aligned} \tag{B.10}$$

along with the surface incompressibility relation,

$$\nabla\cdot\tilde{\boldsymbol{v}} = 2\tilde{w}\tilde{H}. \tag{B.11}$$

The normal force balance relation takes the following form

$$\Delta(\tilde{H}-\hat{L}\hat{S}\phi)+2(\tilde{H}-\ell L\sigma_s\phi)(2\tilde{H}^2-\tilde{K})-2\hat{B}\hat{S}\tilde{H}\Bigg[\{\phi\log\phi+(1-\phi)\log(1-\phi)\}+\frac{\hat{A}}{2}\phi(1-\phi)$$
$$+\frac{\hat{A}}{4\hat{S}}|\nabla\phi|^2\Bigg]-2\tilde{H}\left[(\tilde{H}-\ell\sigma_s L\phi)^2\right]-\hat{T}\left[\tilde{\boldsymbol{b}}:\tilde{\boldsymbol{d}}-w(4\tilde{H}^2-2\tilde{K})\right]=\tilde{p}+\hat{T}\tilde{\lambda}\tilde{H}. \tag{B.12}$$

The mass conservation of proteins is given by

$$\begin{aligned}\phi_t+Pe\,\nabla\cdot(\tilde{\boldsymbol{v}}\phi)=\Delta\phi\left[\frac{1}{1-\phi}+\frac{2\hat{L}^2\hat{S}}{\hat{B}}\phi-\hat{A}\phi\right]-\phi\left[\frac{2\hat{L}}{\hat{B}}\Delta H+\frac{\hat{A}}{2\hat{S}}\Delta^2\phi\right]\\+\nabla\phi\cdot\left[\nabla\phi\left(\frac{1}{(1-\phi)^2}+\frac{2\hat{L}^2\hat{S}}{\hat{B}}-\hat{A}\right)-\frac{2\hat{L}}{\hat{B}}\nabla\tilde{H}-\frac{\hat{A}}{2\hat{S}}\nabla(\Delta\phi)\right].\end{aligned} \tag{B.13}$$

B.1.3 Governing equations in the linear Monge regime

The continuity condition and tangential force balance simplify as

$$\nabla\cdot\boldsymbol{v}=2wH, \tag{B.14}$$

and,

$$\begin{aligned}\nabla\lambda+\nabla^2\boldsymbol{v}+\nabla(\nabla\cdot\boldsymbol{v})-4w\nabla H-2\nabla w:\nabla\nabla z=\\-\nabla\phi\left[\frac{2\hat{B}\hat{S}}{\hat{T}}\log\frac{\phi}{1-\phi}-\frac{4\hat{L}\hat{S}}{\hat{T}}(H-\hat{L}\hat{S}\phi)-\frac{\hat{A}\hat{B}\hat{S}}{\hat{T}}(2\phi-1)-\frac{\hat{A}\hat{B}}{\hat{T}}\nabla^2\phi\right].\end{aligned} \tag{B.15}$$

The normal force balance Equation (C.3) reduces to

$$\nabla^4 z-2\hat{L}\hat{S}\nabla^2\phi-2\hat{B}\hat{S}\nabla^2 z\left[\{\phi\log\phi+(1-\phi)\log(1-\phi)\}+\frac{\hat{A}}{2}\phi(1-\phi)+\frac{\hat{A}}{4\hat{S}}|\nabla\phi|^2+\frac{\hat{L}^2\hat{S}}{\hat{B}}\phi^2\right]$$
$$-\hat{T}(\nabla\boldsymbol{v}+\nabla\boldsymbol{v}^T):\nabla\nabla z=p+\hat{T}\lambda\nabla^2 z. \tag{B.16}$$

Finally, the transport equation for the protein density field Equation (C.4) takes on the following form:

$$\begin{aligned}\phi_t + Pe\ \nabla\cdot(\boldsymbol{v}\phi) = \nabla^2\phi\left[\frac{1}{1-\phi}+\frac{2\hat{L}^2\hat{S}}{\hat{B}}\phi-\hat{A}\phi\right]-\phi\left[\frac{2\hat{L}}{\hat{B}}\nabla^2 H+\frac{\hat{A}}{2\hat{S}}\nabla^4\phi\right]\\ +\nabla\phi\cdot\left[\nabla\phi\left(\frac{1}{(1-\phi)^2}+\frac{2\hat{L}^2\hat{S}}{\hat{B}}-\hat{A}\right)-\frac{2\hat{L}}{\hat{B}}\nabla H-\frac{\hat{A}}{2\hat{S}}\nabla(\nabla^2\phi)\right].\end{aligned} \tag{B.17}$$

B.1.4 Linear stability analysis in the linear Monge regime

We substitute the follwoing normal modes into Equation (5.20) and Equation (5.21),

$$\phi' = \Phi e^{\alpha t} e^{i2\pi\boldsymbol{k}\cdot\boldsymbol{x}} \quad \text{and} \quad z' = Z e^{\alpha t} e^{i2\pi\boldsymbol{k}\cdot\boldsymbol{x}}, \tag{B.18}$$

yielding the relations

$$\begin{aligned}Z\Bigg[16\pi^4k^4+8\pi^2k^2\hat{B}\hat{S}\Bigg(\{\phi_0\log\phi_0+(1-\phi_0)\log(1-\phi_0)\}\\ +\frac{\hat{A}}{2}\phi_0(1-\phi_0)+\frac{\hat{L}^2\hat{S}}{\hat{B}}\phi_0^2\Bigg)+4\pi^2k^2\hat{T}\Bigg]=-8\pi^2k^2\hat{L}\hat{S}\Phi,\end{aligned} \tag{B.19}$$

and

$$\alpha\Phi = -4\pi^2k^2\Phi\left[\frac{1}{1-\phi_0}+\frac{2\hat{L}^2\hat{S}}{\hat{B}}\phi_0-\hat{A}\phi_0\right]-16\pi^4k^4\phi_0\left[\frac{\hat{L}}{\hat{B}}Z+\frac{\hat{A}}{2\hat{S}}\Phi\right]. \tag{B.20}$$

Eliminating variables Z and Φ, we obtain the dispersion relation given in Equation (5.22).

B.1.5 Numerical methods

We solved the dimensionless governing equations in the linear Monge regime (Equation (B.14) to Equation (B.17)) numerically inside a square domain with periodic boundary conditions. Numerical simulations were performed on a spatial uniform grid of size 64×64

for the lower value of $\hat{S}$ (200). However, we considered a finer uniform grid of size 128×128 for the higher values of $\hat{S}$ (500, 1000, and 2000), where we observed smaller sizes of protein aggregates. We used a finite difference scheme to solve the transport equation for the protein density (Equation (B.17)), whereas the velocity (Equation (B.14) and Equation (B.15)) and the shape (Equation (B.16)) were solved using a Fourier spectral method [113, 114]. A semi-implicit scheme was used for the time marching for the protein density ϕ with a time step $\Delta t = 3 \times 10^{-4}$, where the nonlinear terms involving velocity and curvature were treated explicitly. In contrast, the nonlinear aggregation-diffusion terms were treated with linear implicit terms. The resulting transport equation is shown below

$$\frac{\phi^{n+1}-\phi^{n}}{\Delta t} + Pe\ \nabla\cdot(\boldsymbol{v}^{\overline{n+1}}\phi^{n+1}) = \nabla^2\phi^{n+1}\left[\frac{1}{1-\phi}+\frac{2\hat{L}^2\hat{S}}{\hat{B}}\phi-\hat{A}\phi\right]^{\overline{n+1}} - \phi^{n+1}\left[\frac{2\hat{L}}{\hat{B}}\nabla^2 H^{\overline{n+1}}\right] + \phi^{\overline{n+1}}\left[\frac{\hat{A}}{2\hat{S}}\nabla^4\phi^{n+1}\right] + \nabla\phi^{n+1}\cdot\left[\nabla\phi\left(\frac{1}{(1-\phi)^2}+\frac{2\hat{L}^2\hat{S}}{\hat{B}}-\hat{A}\right)-\frac{2\hat{L}}{\hat{B}}\nabla H-\frac{\hat{A}}{2\hat{S}}\nabla(\nabla^2\phi)\right]^{\overline{n+1}}, \tag{B.21}$$

where the superscript $\overline{n+1}$ indicates the explicit terms for time step $n+1$, for which the currently available values were considered. The explicit terms were further updated using an iterative scheme, and within each iteration, velocity and shape were recalculated for the updated values of protein density. The iterations were performed within a time step until convergence was achieved. For the convergence within a time step, we used a tolerance of 5×10^{-7}. When the differences between values of variables from successive iterations fell below the tolerance, we considered the values of the variables to be converged in that time step.

B.2 Phase diagram of membrane deformation and membrane tension

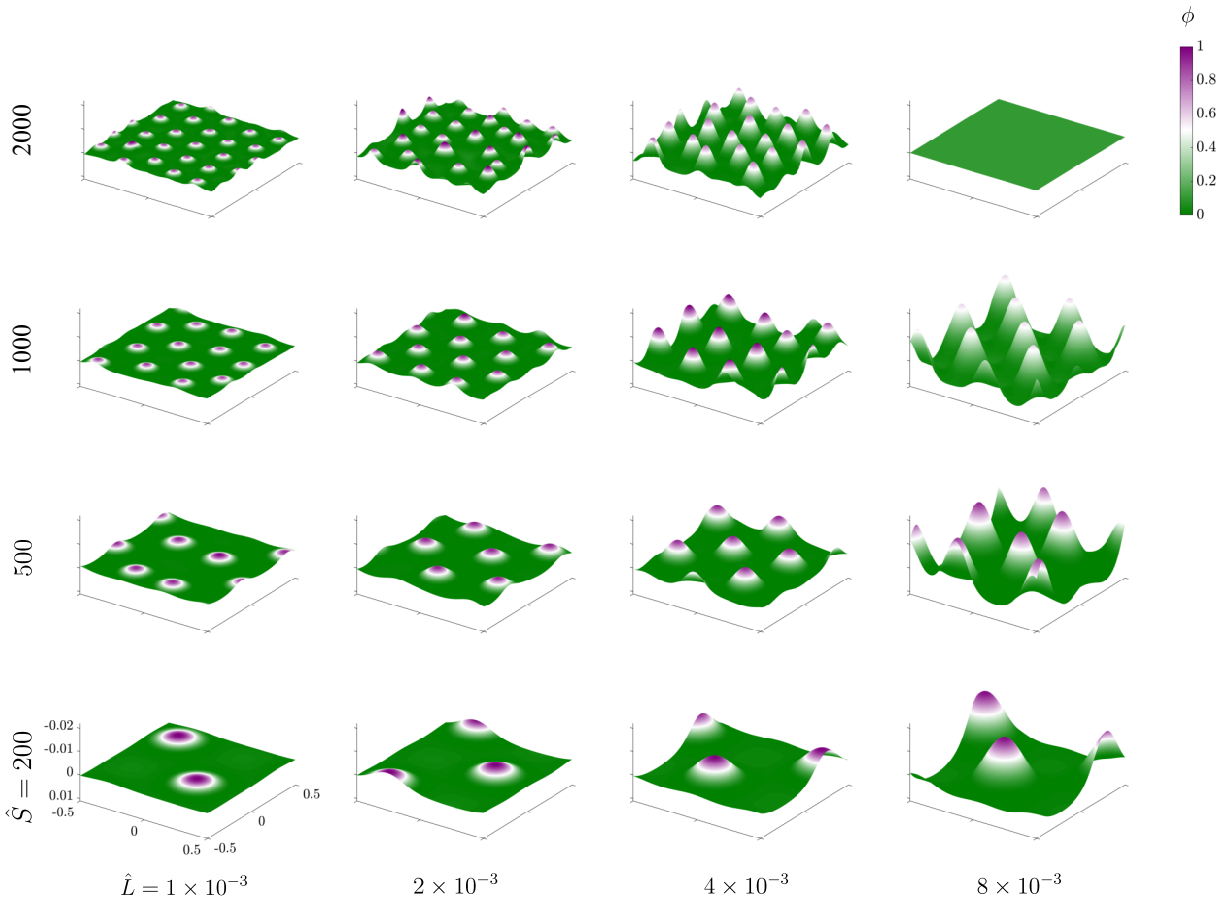

Figure B.1: Protein distribution on the deformed membrane at a long time mimicking the steady state in the plane of $\hat{L}$ and $\hat{S}$, with $\hat{A} = 25$.

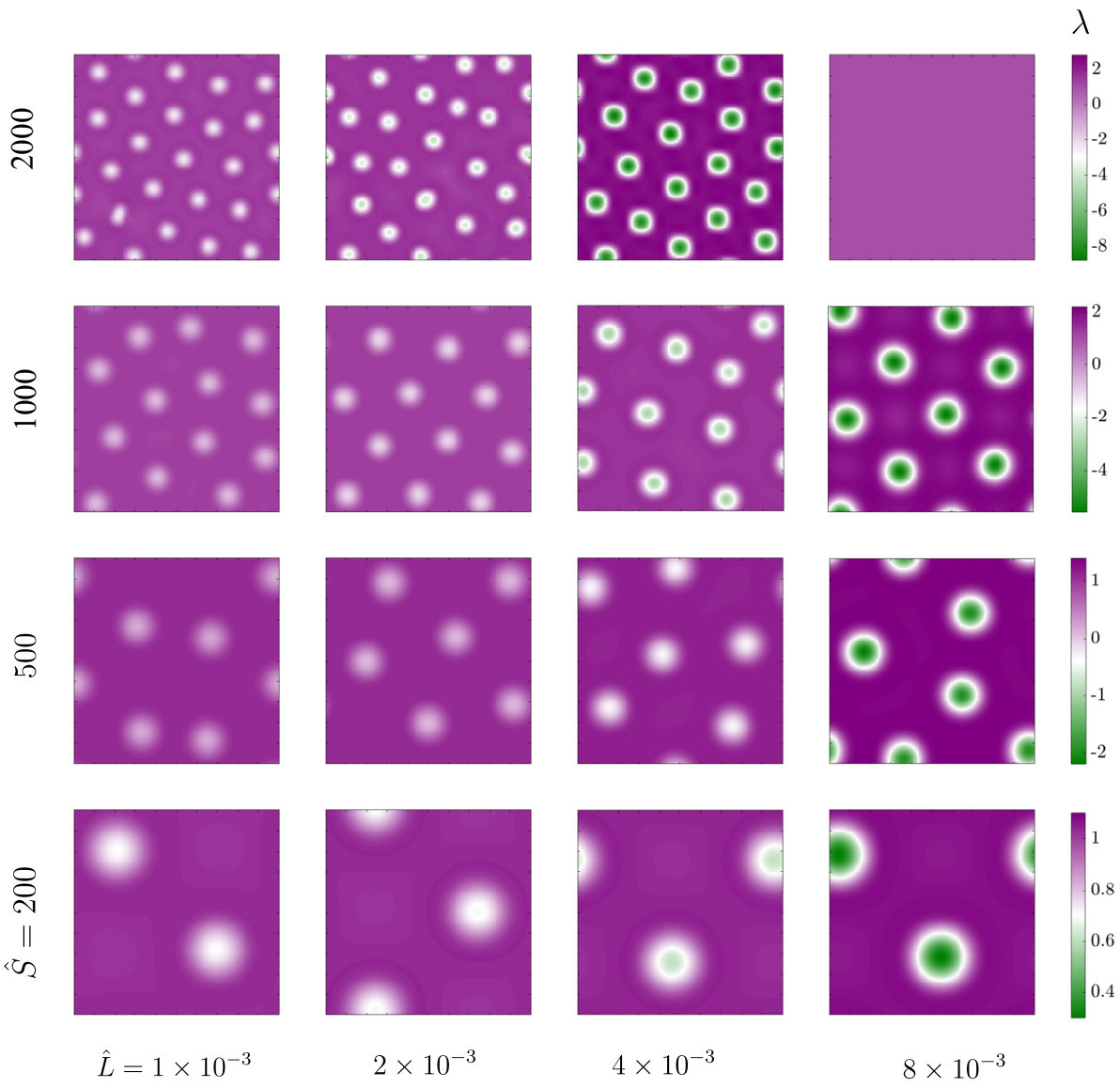

Figure B.2: Membrane tension on the projected membrane surface at a long time mimicking the steady state in the plane of $\hat{L}$ and $\hat{S}$, with $\hat{A} = 25$.

Appendix C

Dimensionless governing equation for protein binding

The tangential force balance relation (Equation 6.7) and continuity (Equation 6.8) reduce to

$$\begin{aligned}\nabla\tilde{\lambda} - 4\tilde{w}\nabla\tilde{H} + 2(\nabla\cdot\tilde{\boldsymbol{d}} - \nabla\tilde{w}\cdot\tilde{\boldsymbol{b}}) \\ = -\nabla\phi\left[\frac{2\hat{B}\hat{S}}{\hat{T}}\log\frac{\phi}{1-\phi} - \frac{4\hat{L}\hat{S}}{\hat{T}}(\tilde{H} - \hat{L}\hat{S}\phi) - \frac{\hat{A}\hat{B}\hat{S}}{\hat{T}}(2\phi-1) - \frac{\hat{A}\hat{B}}{\hat{T}}\Delta\phi - \frac{2\hat{M}\hat{B}\hat{S}}{\hat{T}}\right],\end{aligned} \tag{C.1}$$

along with the surface incompressibility relation,

$$\nabla\cdot\tilde{\boldsymbol{v}} = 2\tilde{w}\tilde{H}. \tag{C.2}$$

The normal force balance equation (Equation 6.9) becomes

$$\Delta(\tilde{H}-\hat{L}\hat{S}\phi)+2(\tilde{H}-\ell L\sigma_s\phi)(2\tilde{H}^2-\tilde{K})-2\hat{B}\hat{S}\tilde{H}\left[\phi\log\phi+(1-\phi)\log(1-\phi)+\frac{\hat{A}}{2}\phi(1-\phi)\right.$$
$$\left.+\frac{\hat{A}}{4\hat{S}}|\nabla\phi|^2-\hat{M}\phi\right]-2\tilde{H}\left[(\tilde{H}-\ell\sigma_s L\phi)^2\right]-\hat{T}\left[\tilde{\boldsymbol{b}}:\tilde{\boldsymbol{d}}-w(4\tilde{H}^2-2\tilde{K})\right]=\tilde{p}+\hat{T}\tilde{\lambda}\tilde{H}. \tag{C.3}$$

The transport equation of protein in the membrane (Equation 6.10) is given by

$$\begin{aligned}\phi_{,t}+Pe\,\nabla\cdot(\tilde{\boldsymbol{v}}\phi)=\Delta\phi\left[\frac{1}{1-\phi}+\frac{2\hat{L}^2\hat{S}}{\hat{B}}\phi-\hat{A}\phi\right]-\phi\left[\frac{2\hat{L}}{\hat{B}}\Delta H+\frac{\hat{A}}{2\hat{S}}\Delta^2\phi\right]\\ +\nabla\phi\cdot\left[\nabla\phi\left(\frac{1}{(1-\phi)^2}+\frac{2\hat{L}^2\hat{S}}{\hat{B}}-\hat{A}\right)-\frac{2\hat{L}}{\hat{B}}\nabla\tilde{H}-\frac{\hat{A}}{2\hat{S}}\nabla(\Delta\phi)\right]+Q(\Phi,\phi).\end{aligned} \tag{C.4}$$

The conservation equation of protein in the bulk domain (Equation 6.11) reduces to

$$\frac{\partial\Phi}{\partial t}=-\int_A Q(\Phi,\phi)dA. \tag{C.5}$$

The above system of equations involves several dimensionless groups as given in Table 6.1.

Appendix D

Derivation of shape equation for protein-induced tube formation

D.1 Model Development

D.1.1 Surface representation

In a polar coordinate the membrane can be parameterized by the arclength s and the rotation angle θ as

$$\boldsymbol{r}(r,z,\theta) = \boldsymbol{r}(s,\theta). \tag{D.1}$$

The surface tangents are given by $\boldsymbol{e}_s = \boldsymbol{r}_{,s}$ and $\boldsymbol{r}_{,\theta}$. The surface metric $a_{ij} = \boldsymbol{e}_i \cdot \boldsymbol{e}_j$ becomes

$$a_{ij} = \begin{bmatrix} 1 & 0 \\ 0 & r^2 \end{bmatrix}. \tag{D.2}$$

The curvature tensor $b_{ij} = e_{i,j}.\boldsymbol{n}$ simplifies to

$$b_{ij} = \begin{bmatrix} \psi_s & 0 \\ 0 & r\sin\psi \end{bmatrix}. \tag{D.3}$$

The mean curvatures is given by

$$H = \frac{1}{2} a^{\alpha\beta} b_{\alpha\beta},$$

where, $a^{\alpha\beta}$ is the inverse of the metric tension. The principal curvature can be extracted from the curvature tensor as

$$c_\zeta = b_{\alpha\beta}\xi^\alpha\xi^\beta,$$

and

$$c_\mu = b_{\alpha\beta}\nu^\alpha\nu^\beta.$$

where, ***xi*** and $\boldsymbol{\nu}$ are surface tangents in two principal directions, The deviatoric curvature becomes

$$D = \frac{1}{2}(c_\xi - c_\nu).$$

D.1.2 Protein Orientation

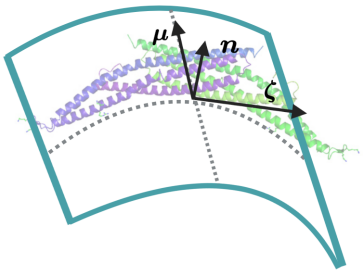

Figure D.1: Orientation vectors of BAR-domain proteins

The orientation of a protein on the surface can be represented by orientation unit vector

$\boldsymbol{\zeta}$ which essentially indicates tangent to the curve on which protein orients [190]. Thus we can constitute another unit vector $\boldsymbol{\mu}$, such that: $\boldsymbol{\mu} = \boldsymbol{n} \times \boldsymbol{\zeta}$.

D.1.3 Balance relations

The force balance equation is dictated by

$$\boldsymbol{T}^{\alpha}_{;\alpha} + p\boldsymbol{n} = \boldsymbol{0}, \tag{D.4}$$

where, p is normal pressure on the membrane and $\boldsymbol{T}$ is traction on the membrane and given by,

$$\boldsymbol{T}^{\alpha} = N^{\beta\alpha}\boldsymbol{a}_{\beta} + S^{\alpha}\boldsymbol{n}. \tag{D.5}$$

Here, $\boldsymbol{N}$ in-plane components of the stress and is given by We further have,

$$N^{\beta\alpha} = \zeta^{\beta\alpha} + b^{\beta}_{\mu} M^{\mu\alpha} \qquad \text{and} \qquad S^{\alpha} = -M^{\alpha\beta}_{;\beta}, \tag{D.6}$$

where, $\sigma^{\beta\alpha}$ and $M^{\beta\alpha}$ are obtained from the following constitutive relations [55]

$$\sigma^{\beta\alpha} = \rho\left(\frac{\partial F}{\partial a_{\alpha\beta}} + \frac{\partial F}{\partial a_{\beta\alpha}}\right) \quad \text{and} \quad \boldsymbol{M}^{\beta\alpha} = \frac{\rho}{2}\left(\frac{\partial F}{\partial b_{\alpha\beta}} + \frac{\partial F}{\partial b_{\beta\alpha}}\right), \tag{D.7}$$

with $F = W/\rho$ is the energy mass density of the membrane. Combining these we get the balance equations in tangent and normal direction

$$N^{\beta\alpha}_{;\alpha} - S^{\alpha} b^{\beta}_{\alpha} = 0, \quad S^{\alpha}_{;\alpha} + N^{\beta\alpha} b_{\beta\alpha} + p = 0 \tag{D.8}$$

The normal force balance relation in Equation D.8$_{ii}$ becomes [190]

$$\underbrace{\frac{1}{2}[W_D(\zeta^\alpha\zeta^\beta-\mu^\alpha\mu^\beta)]_{;\beta\alpha}}_{\text{I}}+\underbrace{\frac{1}{2}W_D(\zeta^\alpha\zeta^\beta-\mu^\alpha\mu^\beta)b_{\alpha\gamma}b^\gamma_\beta}_{\text{II}}+$$
$$\Delta(\frac{1}{2}W_H)+(W_K)_{;\beta\alpha}\tilde{b}^{\beta\alpha}+W_H(2H^2-K)+2H(KW_K-W)-2H\lambda=p, \tag{D.9}$$

where the marked terms are simplified in the next section for an axisymmetric geometry. To construct a force boundary condition we use the expression of the normal traction force as given by

$$\begin{aligned}F_n=&(\tau W_K)'-\frac{1}{2}(W_H)_{,\nu}-(W_K)_{,\beta}\tilde{b}^{\alpha\beta}v_\alpha\\&+\frac{1}{2}(W_D)_{,\nu}-\left(W_D\lambda^\alpha\lambda^\beta\right)_{;\beta}v_\alpha-\left(W_D\lambda^\alpha\lambda^\beta v_\beta\tau_\alpha\right)'.\end{aligned} \tag{D.10}$$

D.2 Simplification in axisymmetry

D.2.1 Governing equations

We have orthogonal surface tangent vectors as given by

$$\boldsymbol{a}_1=\boldsymbol{e}_s\quad \boldsymbol{a}_2=r\boldsymbol{e}_\theta. \tag{D.11}$$

We get the expression of orientation unit vector in terms of orthogonal basis vectors as given below

$$\boldsymbol{\zeta}=-\boldsymbol{e}_\theta=-\frac{1}{r}\boldsymbol{a}_2\quad \boldsymbol{\mu}=\boldsymbol{a}_1. \tag{D.12}$$

We first find the expressions of the direct products of orientation vectors used in Equation (D.9) below

$$\zeta^\alpha\zeta^\beta=\begin{pmatrix}0&0\\0&1/r^2\end{pmatrix}, \tag{D.13}$$

and

$$\mu^{\alpha}\mu^{\beta} = \begin{pmatrix} 1 & 0 \\ 0 & 0 \end{pmatrix}. \tag{D.14}$$

In the limit of axisymmetry, the components of Christoffel symbols denoted by $\Gamma^{a}_{bc} = \frac{1}{2}a^{ad}\left[\partial_a a_{bd} + \partial_b a_{dc} - \partial_d a_{bc}\right]$ simplifies to

$$\begin{aligned} &\Gamma^{1}_{11} = 0, \quad \Gamma^{2}_{22} = 0, \quad \Gamma^{1}_{22} = -r\cos\theta, \\ &\Gamma^{2}_{12} = \Gamma^{2}_{21} = \tfrac{\cos\psi}{r}, \quad \Gamma^{1}_{21} = 0, \text{and} \quad \Gamma^{2}_{11} = 0. \end{aligned} \tag{D.15}$$

We first simplify the term I in equation Equation (D.9) below

$$\begin{aligned} \mathrm{I} &= \frac{1}{2}\left[W_D\left(\lambda^{\alpha}\lambda^{\beta} - \mu^{\alpha}\mu^{\beta}\right)\right]_{;\beta\alpha} \\ &= (W_D\lambda^{\alpha}\lambda^{\beta})_{;\beta\alpha} - \frac{1}{2}\left[W_D\left(\lambda^{\alpha}\lambda^{\beta} + \mu^{\alpha}\mu^{\beta}\right)\right]_{;\beta\alpha} \\ &= (W_D\lambda^{\alpha}\lambda^{\beta})_{;\beta\alpha} - \frac{1}{2}(W_D a^{\alpha\beta})_{;\beta\alpha}. \end{aligned} \tag{D.16}$$

Note that we recover the surface metric from the addition of the direct products of the orientation vectors as given below

$$\left(\lambda^{\alpha}\lambda^{\beta} + \mu^{\alpha}\mu^{\beta}\right) = \begin{bmatrix} 1 & 0 \\ 0 & 1/r^2 \end{bmatrix} = a^{\alpha\beta}. \tag{D.17}$$

From Equation D.16 we can further write term I as

$$\begin{aligned} \mathrm{I} &= (W_D\lambda^{\alpha}\lambda^{\beta})_{;\beta\alpha} - \frac{1}{2}\Delta(W_D) \\ &= \eta^{\beta}_{;\beta} - \frac{1}{2}\Delta(W_D), \end{aligned} \tag{D.18}$$

where

$$\begin{aligned} \eta^{\beta} &= \left(W_D\lambda^{\alpha}\lambda^{\beta}\right)_{;\alpha} \\ &= \left(W_D\lambda^{\alpha}\lambda^{\beta}\right)_{,\alpha} + W_D\Gamma^{\alpha}_{\alpha\gamma}\lambda^{\gamma}\lambda^{\beta} + W_D\Gamma^{\beta}_{\alpha\gamma}\lambda^{\alpha}\lambda^{\gamma}. \end{aligned} \tag{D.19}$$

The components of η^{β} are estimated below in two principal directions

$$\eta^1 = 0 + 0 + W_D \Gamma^1_{22} \lambda^2 \lambda^2 = -\frac{\cos\psi}{r} W_D, \tag{D.20}$$

and

$$\eta^2 = 0 + 0 + 0 = 0. \tag{D.21}$$

The divergent $\eta^{\beta}_{;\beta}$ reduces to

$$\begin{aligned} \eta^{\beta}_{;\beta} &= \frac{1}{\sqrt{a}} (\sqrt{a}\eta^{\beta})_{,\beta} \\ &= \frac{1}{r} (r\eta^1)_{,1} \\ &= -\frac{(\cos\psi W_D)'}{r}. \end{aligned} \tag{D.22}$$

Substituting the expression of $\eta^{\beta}_{;\beta}$ in Equation D.16 we get term I simplified as

$$\mathrm{I} = -\frac{1}{2}\Delta(W_D) - \frac{(\cos\psi W_D)'}{r}. \tag{D.23}$$

Next, we simplify term II below

$$\begin{aligned} \mathrm{II} &= \frac{1}{2} W_D \left(\zeta^{\alpha}\zeta^{\beta} - \mu^{\alpha}\mu^{\beta} \right) b_{\alpha\gamma} b^{\gamma}_{\beta} \\ &= \frac{1}{2} W_D \left\{ \zeta^2 \zeta^2 b_{22} b^2_2 - \mu^1 \mu^1 b_{11} b^1_1 \right\} \\ &= \frac{1}{2} W_D \left\{ \frac{\sin^2\psi}{r^2} - \psi'^2 \right\} \\ &= \frac{1}{2} W_D \left(\frac{\sin\psi}{r} + \psi' \right) \left(\frac{\sin\psi}{r} - \psi' \right) \\ &= \frac{1}{2} W_D \; 2H \; 2D \\ &= 2HDW_D. \end{aligned} \tag{D.24}$$

Finally, using the simplifications of term I (Equation (D.23)) and term II (Equation (D.24)), the shape equation becomes

$$p = \frac{L'}{r} + W_H \left(2H^2 - K\right) - 2H\left(W + \lambda - W_D D\right), \tag{D.25}$$

where L relates to the expression of the traction as shown in Equation (D.10), given by

$$L/r = \frac{1}{2}\left[(W_H)' - (W_D)'\right] - \frac{\cos\psi}{r} W_D = -F_n. \tag{D.26}$$

The above relation gives a natural boundary condition for L at the both the boundary. At the center it directly correlates with the value of pulling force as

$$p_f = \lim_{r \to 0} 2\pi r F_n = -2\pi L(0). \tag{D.27}$$

Note than the derivation of shape equation was presented in [190] where the last term was missing in the definition of L/r in Equation (D.26) and which led to an incorrect residual term $\frac{(W_D)'\cos\psi}{r}$ in the shape equation. Please note that an artificial pulling force is introduced if boundary condition of $L = 0$ is used at the center of the membrane.

D.2.2 Area parameterization

The governing equation is solved in a patch of membrane with fixed surface area, where the coat area of protein is prescribed. The arclength parametrization poses some difficulty since total arclength varies depending on the equilibrium shape of the membrane. Therefore, we did a coordinate transformation of arclength to a local area a as given by

$$\frac{\partial}{\partial s} = 2\pi r \frac{\partial}{\partial a}. \tag{D.28}$$

Note that in the differential form local area relates as

$$da = 2\pi\tilde{r}d\tilde{s} \tag{D.29}$$

The tangential force balance relation in Equation 7 transforms to

$$\frac{\partial\lambda}{\partial a} = 2\kappa(H - C_0)\frac{\partial C_0}{\partial a} + 2\kappa_d(D - D_0)\frac{\partial D_0}{\partial a}. \tag{D.30}$$

The normal force balance relation in Equation 8 becomes

$$p = 2\pi\frac{\partial L}{\partial a} + 2\kappa(H - C_0)\left(2H^2 - K\right) - 2H\left(W + \lambda - 2\kappa_d D(D - D_0)\right) \tag{D.31}$$

where,

$$L/r = \pi r\frac{\partial}{\partial a}\left\{\kappa(H - C_0) - \kappa_d(D - D_0)\right\} - 2\kappa_D(D - D_0)\frac{\cos\psi}{r}. \tag{D.32}$$

D.3 Non-dimensionalization

In this section we use $\tilde{(\cdot)}$ to represent the dimensionless quantities. We used a scale of curvature $1/R_0$, where R_0 is the equivalent length scale in the domain. The dimensionless mean, deviatoric and Gaussian curvature becomes $\tilde{H} = R_0 H$, $\tilde{D} = R_0 D$, and $\tilde{K} = R_0^2 K$. The same scale for curvature is used to nondimensionalize spontaneous mean and deviatoric curvature and they become $\tilde{C}_0 = R_0 C_0$ and $\tilde{D}_0 = R_0 D_0$. The area is dimensionalized with scale $A_0 = 2\pi R_0^2$. The scale for membrane tension is taken as κ/R_0^2, therefore $\tilde{\lambda} = R_0^2\lambda/\kappa$. The dimensionless form of L becomes $\tilde{L} = R_0 L/\kappa$.

The tangential force balance relation in Equation (D.30) reads as

$$\frac{\partial\tilde{\lambda}}{\partial\tilde{a}} = 2(\tilde{H} - \tilde{C}_0)\frac{\partial\tilde{C}_0}{\partial\tilde{a}} + 2\tilde{\kappa}_d(\tilde{D} - \tilde{D}_0)\frac{\partial\tilde{D}_0}{\partial\tilde{a}}, \tag{D.33}$$

where $\tilde{\kappa}_d = \frac{\kappa_d}{\kappa}$ represents the dimensionless deviatoric curvature. The normal force balance relation in Equation (D.31) simplifies to

$$\tilde{p} = \frac{\partial \tilde{L}}{\partial \tilde{a}} + 2(\tilde{H} - \tilde{C}_0)\left(2\tilde{H}^2 - \tilde{K}\right) - 2\tilde{H}\Big\{(\tilde{H} - \tilde{C}_0)^2 + \tilde{\kappa}_d(\tilde{D} - \tilde{D}_0)^2 + \tilde{\lambda} - 2\tilde{\kappa}_d\tilde{D}(\tilde{D} - \tilde{D}_0)\Big\}, \tag{D.34}$$

with

$$\tilde{L}/\tilde{r} = \tilde{r}^2 \frac{\partial}{\partial \tilde{a}}\Big\{(H - C_0) - \tilde{\kappa}_d(D - D_0)\Big\} - 2\tilde{\kappa}_d(D - D_0)\frac{\cos\psi}{r}. \tag{D.35}$$

D.4 Scale analysis

In this section we will estimate a scale of tube radius for a protein-induced tube formation. Free energy of the membrane across the membrane area for a tubular geometry simplifies to

$$E = 2\pi RL\left\{\kappa\left(\frac{1}{2R} - D_0\right)^2 + \kappa\left(\frac{1}{2R} - D_0\right)^2\right\} + \lambda_0 2\pi RL. \tag{D.36}$$

The energy minimization gives the size of the tubes. The variation of energy with the tube radius reads as

$$\begin{aligned}\frac{\partial E}{\partial R} &= 2\pi L\left\{2\kappa\left(\frac{1}{2R} - D_0\right)^2\right\} + 2\pi RL\left\{4\kappa\left(\frac{1}{2R} - D_0\right)\left(-\frac{1}{2R^2}\right)\right\} + \lambda_0 2\pi L \\ &= 4\pi\kappa L\left(\frac{1}{2R} - D_0\right)\left(\frac{1}{2R} - D_0 - \frac{1}{R}\right) + \lambda_0 2\pi L \\ &= -4\pi\kappa L\left(\frac{1}{4R^2} - D_0^2\right) + \lambda_0 2\pi L\end{aligned} \quad . \tag{D.37}$$

We obtain estimation of the tube radius by equating the variation of energy to zero, as given by:

$$\begin{aligned} \frac{\partial E}{\partial r} &= 0 = -4\pi\kappa L\left(\frac{1}{4R^2} - D_0^2\right) + \lambda_0 2\pi L \\ \text{or,} \quad R &= \frac{1}{\sqrt{\frac{2\lambda_0}{\kappa} + 4D_0^2}}. \end{aligned} \tag{D.38}$$

Bibliography

[1] R. Glowinski, T.-W. Pan, V. L. H. Juarez, and E. Dean, "Numerical methods for the simulation of incompressible viscous flow: An introduction," in *Multidisciplinary Methods for Analysis Optimization and Control of Complex Systems*, pp. 49–175, Springer, 2005.

[2] B. Alberts, A. Johnson, J. Lewis, M. Raff, K. Roberts, and P. Walter, *Molecular Biology of the Cell*. Garland Science, 1985.

[3] T. Harayama and H. Riezman, "Understanding the diversity of membrane lipid composition," *Nat. Rev. Mol. Cell Biol. Cell Biol.*, vol. 19, pp. 281–296, 2018.

[4] P. Bassereau, R. Jin, T. Baumgart, M. Deserno, R. Dimova, V. A. Frolov, P. V. Bashkirov, H. Grubmüller, R. Jahn, H. J. Risselada, L. Johannes, M. M. Kozlov, R. Lipowsky, T. J. Pucadyil, W. F. Zeno, J. C. Stachowiak, D. Stamou, A. Breuer, L. Lauritsen, C. Simon, C. Sykes, G. A. Voth, and T. R. Weikl, "The 2018 biomembrane curvature and remodeling roadmap," *Journal of physics D: Applied physics*, vol. 51, no. 34, p. 343001, 2018.

[5] S. Singer, "The molecular organization of membranes," *Annu. Rev. Biochem.*, vol. 43, pp. 805–833, 1974.

[6] K. S. Kim, J. Neu, and J. Oster, "Curvature-mediated interactions between membrane proteins," *Biophys. J.*, vol. 75, pp. 2274–2291, 1998.

[7] E. Sackmann, H. P. Duwe, and H. Engelhardt, "Membrane bending elasticity and its role for shape fluctuations and shape transformations of cells and vesicles," *Faraday Discuss. Chem. Soc.*, vol. 81, pp. 281–290, 1986.

[8] R. Lipowsky, "The conformation of membranes," *Nature*, vol. 349, pp. 475–481, 1991.

[9] F. Jülicher and R. Lipowsky, "Domain-induced budding of vesicles," *Phys. Rev. Lett.*, vol. 70, pp. 2964–2967, 1993.

[10] J. Zimmerberg and M. M. Kozlov, "How proteins produce cellular membrane curvature," *Nat. Rev. Mol. Cell Biol.*, vol. 7, pp. 9–19, 2006.

[11] J. E. Hassinger, G. Oster, D. G. Drubin, and P. Rangamani, "Design principles for robust vesiculation in clathrin-mediated endocytosis," *Proc. Natl. Acad. Sci.*, vol. 114, pp. 1118–1127, 2017.

[12] H. T. McMahon and J. L. Gallop, "Membrane curvature and mechanisms of dynamic cell membrane remodeling," *Nature*, vol. 438, pp. 590–596, 2005.

[13] J. C. Stachowiak, C. C. Hayden, and D. Y. Saski, "Steric confinement of proteins on lipid membranes can drive curvature and tubulation," *Proc. Natl. Acad. Sci.*, vol. 107, pp. 7781–7786, 2010.

[14] F. Yuan, H. Alimohamadi, B. Bakka, A. N. Trementozzi, N. L. Fawzi, P. Rangamani, and J. C. Stachowiak, "Membrane bending by protein phase separation," 2020.

[15] B. J. Reynwar, G. Illya, V. A. Harmandaris, M. M. Müller, K. Kremer, and M. Deserno, "Aggregation and vesiculation of membrane proteins by curvature-mediated interactions," *Nature*, vol. 447, pp. 461–464, 2007.

[16] S. Mujherjee and E. R. Maxfield, "Role of membrane organization and membrane domains in endocytic lipid trafficking," *Traffic.*, vol. 1, pp. 203–211, 2000.

[17] J. Gruenberg, "The endocytic pathway: A mosaic of domains," *Nat. Rev. Mol. Cell Biol.*, vol. 2, pp. 721–730, 2001.

[18] B. Antonny, "Mechanisms of membrane curvature sensing," *Annu. Rev. Biochem.*, vol. 80, pp. 101–123, 2011.

[19] S. Leibler and D. Andelman, "Ordered and curved meso-structures in membranes and amphiphilic films," *J. Phys. France.*, vol. 48, p. 2013, 1987.

[20] U. Seifert, "Curvature-induced lateral phase segregation in two-component vesicles," *Phys. Rev. Lett.*, vol. 70, p. 1335, 1993.

[21] N. Kahya, D. Scherfeld, K. Bacia, and P. Schwille, "Lipid domain formation and dynamics in giant unilamellar vesicles explored by fluorescence correlation spectroscopy," *J. Struct. Biol.*, vol. 147, pp. 77–89, 2004.

[22] R. Tran-Son-Tay, S. P. Sutera, and P. R. Rao, "Determination of red blood cell membrane viscosity from rheoscopic observations of tank-treading motion," *Biophys. J.*, vol. 46, pp. 1335–1338, 1984.

[23] H. Noguchi and G. Gompper, "Fluid vesicles with viscous membranes in shear flow," *Phys. Rev. Lett.*, vol. 93, p. 258102, 2004.

[24] P. M. Douglas and D. M. Cyr, "Interplay between protein homeostasis networks in protein aggregation and proteotoxicity," *Biopolymers: Orig. Res. Biomol.*, vol. 93, no. 3, pp. 229–236, 2010.

[25] B. J. Reynwar, G. Illya, V. A. Harmandaris, M. M. Müller, K. Kremer, and M. Deserno, "Aggregation and vesiculation of membrane proteins by curvature-mediated interactions," *Nature*, vol. 447, no. 7143, pp. 461–464, 2007.

[26] C. Weber, T. Michaels, and L. Mahadevan, "Spatial control of irreversible protein aggregation," *Elife*, vol. 8, p. e42315, 2019.

[27] T. Baumgart, S. T. Hess, and W. W. Webb, "Imaging coexisting fluid domains in biomembrane models coupling curvature and line tension," *Nature*, vol. 425, pp. 821–824, 2003.

[28] A. Horner, Y. N. Antonenko, and P. Pohl, "Coupled diffusion of peripherally bound peptides along the outer and inner membrane leaflets," *Biophys. J.*, vol. 96, pp. 2689–2695, 2009.

[29] W. T. Snead, C. C. Hayden, A. K. Gadok, E. M. L. C. Zhao, P. Rangamani, and J. C. Stachowiak, "Membrane fission by protein crowding," *Proc. Natl. Acad. Sci.*, vol. 114, pp. 3258–3267, 2017.

[30] Y. Zhang, X. Chen, C. Gueydan, and J. Han, "Plasma membrane changes during programmed cell deaths," *Cell Res*, vol. 28, pp. 9–21, 2018.

[31] J. S. Lowengrub, A. Ratz, and A. Voigt, "Phase-field modeling of the dynamics of multicomponent vesicles: Spinodal decomposition, coarsening, budding, and fission," *Phys. Rev. E*, vol. 79, p. 031926, 2009.

[32] C. M. Elliott and B. Stinner, "Computation of two-phase biomembranes with phase dependent material parameters using surface finite elements," *Commun. Comput. Phys.*, vol. 13, pp. 325–360, 2013.

[33] C. M. Elliott, C. Graser, G. Hobbs, R. Kornhuber, and M. A. Wolf, "A variational approach to particles in lipid membranes," *Arch. Rational Mech. Anal.*, vol. 222, pp. 1011–1075, 2016.

[34] U. Seifert and S. A. Langer, "Viscous modes of fluid bilayer membranes," *Europhys. Lett.*, vol. 23, pp. 65–72, 1993.

[35] A. Sahu, R. A. Sauer, and K. K. Mandadapu, "Irreversible thermodynamics of curved lipid membranes," *Phys. Rev. E*, vol. 96, p. 042409, 2017.

[36] W. Helfrich, "Elastic properties of lipid bilayers: theory and possible experiments," *Z NATURFORSCH C*, vol. 28, no. 11-12, pp. 693–703, 1973.

[37] W. E. Louch, O. M. Sejersted, and F. Swift, "There goes the neighborhood: Pathological alterations in t-tubule morphology and consequences for cardiomyocyte ca++," *BioMed Research International*, vol. 2010, 2010.

[38] P. Paumard, J. Vaillier, B. Coulary, J. Schaeffer, V. Soubannier, D. M. Mueller, D. Brèthes, J.-P. di Rago, and J. Velours, "The atp synthase is involved in generating mitochondrial cristae morphology," *EMBO J.*, vol. 21, no. 3, pp. 221–230, 2002.

[39] M. Gomez, D. E. Moulton, and D. Vella, "Critical slowing down in purely elastic 'snap-through'instabilities," *Nat. Phys.*, vol. 13, no. 2, pp. 142–145, 2017.

[40] M. Gomez, D. E. Moulton, and D. Vella, "Dynamics of viscoelastic snap-through," *J. Mech. and Phys. Solids*, vol. 124, pp. 781–813, 2019.

[41] A. Iglič, B. Babnik, U. Gimsa, and V. Kralj-Iglič, "On the role of membrane anisotropy in the beading transition of undulated tubular membrane structures," *Journal of Physics A: Mathematical and General*, vol. 38, no. 40, p. 8527, 2005.

[42] N. Bobrovska, W. Gozdz, V. Kralj-Iglic, and A. Iglic, "On the role of anisotropy of membrane components in formation and stabilization of tubular structures in multicomponent membranes," *PLOS ONE*, vol. 8, no. 9, p. e73941, 2013.

[43] F. Campelo and A. Hernández-Machado, "Polymer-induced tubulation in lipid vesicles," *Phys. Rev. Lett.*, vol. 100, no. 15, p. 158103, 2008.

[44] B. J. Peter, H. M. Kent, I. G. Mills, Y. Vallis, P. J. G. Butler, P. R. Evans, and H. T. McMahon, "Bar domains as sensors of membrane curvature: the amphiphysin bar structure," *Science*, vol. 303, no. 5657, pp. 495–499, 2004.

[45] H. Alimohamadi and P. Rangamani, "Modeling membrane curvature generation due to membrane–protein interactions," *Biomolecules*, vol. 8, no. 4, p. 120, 2018.

[46] F. Yuan, H. Alimohamadi, B. Bakka, A. N. Trementozzi, N. L. Fawzi, P. Rangamani, and J. C. Stachowiak, "Membrane bending by protein phase separation," *bioRxiv*, 2020.

[47] M. C. Heinrich, B. R. Capraro, A. Tian, J. M. Isas, R. Langen, and T. Baumgart, "Quantifying membrane curvature generation of drosophila amphiphysin n-bar domains," *J. Phys. Chem. letters*, vol. 1, no. 23, pp. 3401–3406, 2010.

[48] M. G. Ford, I. G. Mills, B. J. Peter, Y. Vallis, G. J. Praefcke, P. R. Evans, and H. T. McMahon, "Curvature of clathrin-coated pits driven by epsin," *Nature*, vol. 419, no. 6905, pp. 361–366, 2002.

[49] O. Campas, C. Leduc, P. Bassereau, J.-F. Joanny, and J. Prost, "Collective oscillations of processive molecular motors," *Biophysical Reviews and Letters*, vol. 4, no. 01n02, pp. 163–178, 2009.

[50] C. Leduc, O. Campàs, K. B. Zeldovich, A. Roux, P. Jolimaitre, L. Bourel-Bonnet, B. Goud, J.-F. Joanny, P. Bassereau, and J. Prost, "Cooperative extraction of membrane nanotubes by molecular motors," *Proc. Natl. Acad. Sci. U.S.A.*, vol. 101, no. 49, pp. 17096–17101, 2004.

[51] P. M. Naghdi, "Theory of shells and plates," in *Handbunch der Physik*, vol. C of *VIa/2*, pp. 425–640, In: Truesdell, 1972.

[52] P. B. Canham, "The minimum energy of bending as a possible explanation of the biconcave shape of the human red blood cell," *J. Theoret. Biol.*, vol. 26, pp. 61–81, 1970.

[53] W. Helfrich, "Elastic properties of lipid bilayers: Theory and possible experiments," *Z. Naturforsch. C*, vol. 5, pp. 693–703, 1973.

[54] J. T. Jenkins, "The equation of mechanical equilibrium of a model membrane," *SIAM J. Appl. Math.*, vol. 4, pp. 693–703, 1977.

[55] D. J. Steigmann, "Fluid films with curvature elasticity," *Arch. Rat. Mech.*, vol. 150, pp. 257–272, 1999.

[56] N. Kahya, D. Scherfeld, K. Bacia, and P. Schwille, "Lipid domain formation and dynamics in giant unilamellar vesicles explored by fluorescence correlation spectroscopy," *J. Struct. Biol.*, vol. 147, no. 1, pp. 77–89, 2004.

[57] H. T. McMahon and J. L. Gallop, "Membrane curvature and mechanisms of dynamic cell membrane remodelling," *Nature*, vol. 438, no. 7068, pp. 590–596, 2005.

[58] I. Nitschke, A. Voigt, and J. Wensch, "A finite element approach to incompressible two-phase flow on manifolds," *J. Fluid Mech.*, vol. 708, p. 418, 2012.

[59] C. J. S. Klaus, K. Raghunathan, E. DiBenedetto, and A. K. Kenworthy, "Analysis of diffusion in curved surfaces and its application to tubular membranes," *Mol. Biol. Cell*, vol. 27, no. 24, pp. 3937–3946, 2016.

[60] P. Gera and D. Salac, "Cahn–Hilliard on surfaces: A numerical study," *Appl. Math. Lett.*, vol. 73, pp. 56–61, 2017.

[61] H. Noguchi and G. Gompper, "Fluid vesicles with viscous membranes in shear flow," *Phys. Rev. Lett.*, vol. 93, no. 25, p. 258102, 2004.

[62] M. Arroyo and A. DeSimone, "Relaxation dynamics of fluid membranes," *Phys. Rev. E*, vol. 79, p. 031915, 2009.

[63] M. Rahimi and M. Arroyo, "Shape dynamics, lipid hydrodynamics, and complex viscoelasdticity of bilayer membranes," *Phys. Rev. E*, vol. 86, p. 011932, 2012.

[64] P. Rangamani, A. Agrawal, K. Mandadapu, G. Oster, and D. Steigmann, "Interaction between surface shape and intra-surface viscous flow on lipid membranes," *Biomech. Model. Mechanobiol.*, vol. 12, pp. 833–845, 2013.

[65] C. Tozzi, N. Walani, and M. Arroyo, "Out-of-equilibrium mechanochemistry and self-organization of fluid membranes interacting with curved proteins," *New J. Phys.*, vol. 21, p. 093004, 2019.

[66] L. E. Scriven, "Dynamics of a fluid surface," *Chem. Eng. Sci.*, vol. 12, pp. 98–108, 1960.

[67] P. Rangamani, K. Mandadapu, and G. Oster, "Protein induced membrane curvature alters local membrane tension," *Biophys. J.*, vol. 107, pp. 751–762, 2014.

[68] F. Bahmani, J. Christenson, and P. Rangamani, "Analysis of lipid flow on minimal surfaces," *Continuum Mech. Thermodyn.*, vol. 28, pp. 503–513, 2016.

[69] A. Iglič, B. Babnik, U. Gimsa, and V. Kralj-Iglič, "On the role of membrane anisotropy in the beading transition of undulated tubular membrane structures," *J. Phys. A*, vol. 40, pp. 8527–8536, 2005.

[70] V. Kralj-Iglič, H. Hagerstand, P. Veranic, K. Jezernik, B. Babnik, D. R. Gauger, and A. Iglič, "Amphiphile-induced tubular budding of the bilayer membrane," *Eur. Biophys. J.*, vol. 34, pp. 1066–1070, 2005.

[71] A. Veksler and N. S. Gov, "Phase transitions of the coupled membrane-cytoskeleton modify cellular shape," *Biophys. J.*, vol. 93, pp. 3798–3810, 2007.

[72] S. Ramaswamy, J. Toner, and J. Prost, "Nonequilibrium fluctuations, travelling waves, and instabilities in active membranes," *Phys. Rev. Lett.*, vol. 84, pp. 3494–3497, 2005.

[73] W. T. Gozdz, "Shape transformation of lipid vesicle induced by diffusing macromolecules," *J. Chem. Phys.*, vol. 134, pp. 371–379, 2011.

[74] D. Steigmann and A. Agrawal, "A model for surface diffusion of trans-membrane protein on lipid bilayers," *Z. Angew. Math. Phys.*, vol. 62, pp. 449–563, 2011.

[75] M. Arroyo, N. Walani, A. Torres-Sanchez, and D. Kaurin, "Onsager's variational principle in soft matter: Introduction and application to the dynamics of adsorption of proteins onto fluid membranes," in *The Role of Mechanics in the Study of Lipid Bilayers* (D. J. Steigmann, ed.), pp. 1–53, Springer, Cham, Switzerland, 2018.

[76] A. Torres-Sanchez, D. Millan, and M. Arroyo, "Modelling fluid deformable surfaces with an emphasis on biological interfaces," *J. Fluid Mech.*, vol. 872, pp. 218–271, 2019.

[77] L. Johannes, R. G. Parton, P. Bassereau, and S. Mayor, "Building endocytic pits without clathrin," *Nat. Rev. Mol. Cell Biol.*, vol. 16, no. 5, pp. 311–321, 2015.

[78] H. T. McMahon and E. Boucrot, "Molecular mechanism and physiological functions of clathrin-mediated endocytosis," *Nat. Rev. Mol. Cell Biol.*, vol. 12, no. 8, pp. 517–533, 2011.

[79] S. Suetsugu, S. Kurisu, and T. Takenawa, "Dynamic shaping of cellular membranes by phospholipids and membrane-deforming proteins," *Physiol. Rev.*, vol. 94, no. 4, pp. 1219–1248, 2014.

[80] T. Baumgart, B. R. Capraro, C. Zhu, and S. L. Das, "Thermodynamics and mechanics of membrane curvature generation and sensing by proteins and lipids," *Annu. Rev. Phys. Chem.*, vol. 62, pp. 483–506, 2011.

[81] S. B. Zimmerman and A. P. Minton, "Macromolecular crowding: biochemical, biophysical, and physiological consequences," *Ann. Rev. Biophys. Biomol. Struc.*, vol. 22, no. 1, pp. 27–65, 1993.

[82] H. Noguchi, "Vesicle budding induced by binding of curvature-inducing proteins," *Phys. Rev. E*, vol. 104, no. 1, p. 014410, 2021.

[83] Q. Goutaland, F. van Wijland, J. Fournier, and H. Noguchi, "Binding of thermalized and active membrane curvature-inducing proteins," *Soft Matter*, vol. 17, no. 22, pp. 5560–5573, 2021.

[84] F. Brauns, J. Halatek, and E. Frey, "Phase-space geometry of mass-conserving reaction-diffusion dynamics," *Physical Rev. X*, vol. 10, no. 4, p. 041036, 2020.

[85] K. Mizuuchi and A. G. Vecchiarelli, "Mechanistic insights of the min oscillator via cell-free reconstitution and imaging," *Phys. Biol.*, vol. 15, no. 3, p. 031001, 2018.

[86] E. R. Middleton and E. Rhoades, "Effects of curvature and composition on α-synuclein binding to lipid vesicles," *Biophys. J.*, vol. 99, no. 7, pp. 2279–2288, 2010.

[87] A. Agrawal and D. J. Steigmann, "A model for surface diffusion of trans-membrane proteins on lipid bilayers," *Zamm-Z Angew. Math. Me.*, vol. 62, no. 3, pp. 549–563, 2011.

[88] A. Mahapatra, D. Saintillan, and P. Rangamani, "Transport phenomena in fluid films with curvature elasticity," *J. Fluid Mech.*, vol. 905, no. A8, pp. 1–31, 2020.

[89] C. Canuto, M. Y. Hussaini, A. Quarteroni, and T. A. Zang, *Spectral Methods*. Springer, 2006.

[90] N. M. Laurendeau, *Statistical thermodynamics: fundamentals and applications*. Cambridge University Press, 2005.

[91] E. Guazzelli and J. F. Morris, *A physical introduction to suspension dynamics*, vol. 45. Cambridge University Press, 2011.

[92] P. Saffman and M. Delbrück, "Brownian motion in biological membranes," *Proc. Nat. Acad. of Sci.*, vol. 72, no. 8, pp. 3111–3113, 1975.

[93] A. Veksler and N. S. Gov, "Phase transitions of the coupled membrane-cytoskeleton modify cellular shape," *Biophys. J.*, vol. 93, no. 11, pp. 3798–3810, 2007.

[94] S. Givli, H. Giang, and K. Bhattacharya, "Stability of multicomponent biological membranes," *SIAM J. Appl. Math.*, vol. 72, no. 2, pp. 489–511, 2012.

[95] T. S. Krishnan, S. L. Das, and P. S. Kumar, "Transition from curvature sensing to generation in a vesicle driven by protein binding strength and membrane tension," *Soft Matter*, vol. 15, no. 9, pp. 2071–2080, 2019.

[96] A. P. Minton, "Effects of excluded surface area and adsorbate clustering on surface adsorption of proteins: I. equilibrium models," *Biophysical chemistry*, vol. 86, no. 2-3, pp. 239–247, 2000.

[97] P. Girard, J. Prost, and P. Bassereau, "Passive or active fluctuations in membranes containing proteins," *Phys. Rev. Lett.*, vol. 94, no. 8, p. 088102, 2005.

[98] K. Fricke and E. Sackmann, "Variation of frequency spectrum of the erythrocyte flickering caused by aging, osmolarity, temperature and pathological changes," *Biochim. Biophys. Acta, Mol. Cell. Res.*, vol. 803, no. 3, pp. 145–152, 1984.

[99] F. Brochard and J. Lennon, "Frequency spectrum of the flicker phenomenon in erythrocytes," *J. Phys.*, vol. 36, no. 11, pp. 1035–1047, 1975.

[100] K. Fricke, K. Wirthensohn, R. Laxhuber, and E. Sackmann, "Flicker spectroscopy of erythrocytes," *Eur. Biophys. J.*, vol. 14, no. 2, pp. 67–81, 1986.

[101] Z. Shi and T. Baumgart, "Dynamics and instabilities of lipid bilayer membrane shapes," *Adv. Colloid Interface Sci.*, vol. 208, pp. 76–88, 2014.

[102] W. Helfrich, "Effect of thermal undulations on the rigidity of fluid membranes and interfaces," *J. Phys.*, vol. 46, no. 7, pp. 1263–1268, 1985.

[103] D. Föster, "On the scale dependence, due to thermal fluctuations, of the elastic properties of membranes," *Phys. Lett. A*, vol. 114, no. 3, pp. 115–120, 1986.

[104] L. Peliti and S. Leibler, "Effects of thermal fluctuations on systems with small surface tension," *Phys. Rev. Lett.*, vol. 54, no. 15, p. 1690, 1985.

[105] G. Gompper and D. Kroll, "Random surface discretizations and the renormalization of the bending rigidity," *J. Phys. I*, vol. 6, no. 10, pp. 1305–1320, 1996.

[106] M. Deserno, "The influence of thermal fluctuations on the bending rigidity of fluid membranes."

[107] P. De Gennes and C. Taupin, "Microemulsions and the flexibility of oil/water interfaces," *J. Phys. Chem.*, vol. 86, no. 13, pp. 2294–2304, 1982.

[108] D. J. Steigmann, "Fluid films with curvature elasticity," *Arch. Ration. Mech. Anal.*, vol. 150, pp. 127–152, Dec. 1999.

[109] P. Rangamani, A. Agrawal, K. K. Mandadapu, G. Oster, and D. J. Steigmann, "Interaction between surface shape and intra-surface viscous flow on lipid membranes," *Biomech. Model. Mechan.*, vol. 12, no. 4, pp. 833–845, 2013.

[110] P. G. Ciarlet, "An introduction to differential geometry with applications to elasticity," *J. Elasticity*, vol. 78, no. 1, pp. 1–215, 2005.

[111] D. Steigmann, E. Baesu, R. E. Rudd, J. Belak, and M. McEleresh, "On the variational theory of cell-membrane equilibria," *Interfaces Free Bound.*, vol. 5, pp. 357–366, 2003.

[112] P. Rangamani, K. K. Mandadap, and G. Oster, "Protein-induced membrane curvature alters local membrane tension," *Biophys. J.*, vol. 107, no. 3, pp. 751–762, 2014.

[113] H. Hasimoto, "On the periodic fundamental solutions of the stokes equations and their application to viscous flow past a cubic array of spheres," *J Fluid Mech.*, vol. 5, no. 2, pp. 317–328, 1959.

[114] S. Safran, *Statistical thermodynamics of surfaces, interfaces, and membranes*. CRC Press, 2018.

[115] D. J. Steigmann, "Mechanics and physics of lipid bilayers," in *The Role of Mechanics in the Study of Lipid Bilayers* (D. J. Steigmann, ed.), pp. 1–61, Springer, Cham, Switzerland, 2018.

[116] I. S. Sokolnikoff, *Tensor Analysis: Theory and Applications*. Wiley, 1951.

[117] E. Kreyszig, *Advanced Engineering Mathematics*. Wiley, 1968.

[118] R. Aris, *Vectors, Tensors and Basic Equation of Fluid Mechanics*. Dover, New York, 1989.

[119] H. Alimohamadi and P. Rangamani, "Modeling membrane curvature generation due to membrane– protein interactions," *Biomolecules*, vol. 8, pp. 120–147, 2018.

[120] N. S. Gov, "Guided by curvature: shaping cells by coupling curved membrane proteins and cytoskeletal forces," *Philos. Trans. R. Soc. Lond. B Biol. Sci.*, vol. 373, p. 20170115, May 2018.

[121] C. Do, *Differential Geometry of Curves and Surfaces*. Prentice Hall, 1976.

[122] M. Chabanon and P. Rangamani, "Gaussian curvature directs the distribution of spontaneous curvature on bilayer membrane necks," *Soft Matter*, vol. 12, pp. 2281–2294, 2018.

[123] M. Chabanon and P. Rangamani, "Geometric coupling of helicoidal ramps and curvature-inducing proteins in organelle membranes," *J. R. Soc. Interface.*, vol. 16, p. 20190354, 2019.

[124] W. T. Góźdź and G. Gompper, "Composition-driven shape transformations of membranes of complex topology," *Phys. Rev. Lett.*, vol. 80, p. 4213, 1998.

[125] F. Campelo and A. Hernández-Machado, "Model for curvature-driven pearling instability in membranes," *Phys. Rev. Lett.*, vol. 99, p. 088101, 2007.

[126] O.-Y. Zhong-Can and W. Helfrich, "Bending energy of vesicle membranes: General expressions for the first, second, and third variation of the shape energy and applications to spheres and cylinders," *Phys. Rev. A*, vol. 39, p. 5280, 1989.

[127] V. Haucke and M. M. Kozlov, "Membrane remodeling in clathrin-mediated endocytosis," *J. Cell Sci.*, vol. 131, p. jcs216812, 2018.

[128] P. N. Dannhauser and E. J. Ungewickell, "Reconstitution of clathrin-coated bud and vesicle formation with minimal components," *Nature Cell Biol.*, vol. 14, pp. 634–639, 2012.

[129] P. Rangamani, A. Behzadan, and M. Holst, "Local sensitivity analysis of the 'membrane shape equation' derived from Helfrich energy," *arxiv*, vol. 2005, p. 12550, 2020.

[130] Y. Kozlovsky and M. M. Kozlov, "Membrane fission: model for intermediate structures," *Biophys. J.*, vol. 85, pp. 85–96, 2003.

[131] R. Jahn, T. Lang, and T. C. Südhof, "Membrane fusion," *Cell*, vol. 112, pp. 519–533, 2003.

[132] J. H. Hurley, E. Boura, L.-A. Carlson, and B. Różycki, "Membrane budding," *Cell*, vol. 143, pp. 875–887, 2010.

[133] A. D. Blazek, B. J. Paleo, and N. Weisleder, "Plasma membrane repair: a central process for maintaining cellular homeostasis," *Physiology*, vol. 30, pp. 438–448, 2015.

[134] R. Vasan, S. Rudraraju, M. Akamatsu, K. Garikipati, and P. Rangamani, "A mechanical model reveals that non-axisymmetric buckling lowers the energy barrier associated with membrane neck constriction," *Soft Matter*, vol. 16, pp. 784–797, 2020.

[135] R. A. Sauer, T. X. Duong, K. K. Mandadapu, and D. J. Steigmann, "A stabilized finite element formulation for liquid shells and its application to lipid bilayers," *J. Comput. Phys.*, vol. 330, pp. 436–466, 2017.

[136] A. Sahu, Y. A. D. Omar, R. A. Sauer, and K. K. Mandadapu, "Arbitrary Lagrangian–Eulerian finite element method for curved and deforming surfaces: I. General theory and application to fluid interfaces," *J. Comput. Phys.*, vol. 407, p. 109253, 2020.

[137] P. B. S. Kumar, G. Gompper, and R. Lipowsky, "Budding dynamics of multicomponent membranes," *Phys. Rev. Lett.*, vol. 86, p. 3911, 2001.

[138] R. Lipowsky, "Spontaneous tubulation of membranes and vesicles reveals membrane tension generated by spontaneous curvature," *Faraday Discuss.*, vol. 161, pp. 305–331, 2013.

[139] K. Glasmaster, C. Larsson, F. Hook, and B. Kasemo, "Protein adsorption on supported phospholipid bilayer," *J. Colloid Interface Sci.*, vol. 246, pp. 40–47, 2002.

[140] V. P. Zhdanov and B. Kasemo, "Adsorption of proteins on a lipid bilayer," *Euro. Biophys. J.*, vol. 39, pp. 1477–1482, 2010.

[141] I. B. Liu, N. Sharifi-Mood, and K. J. Stebe, "Capillary assembly of colloids: Interactions on planar and curved interfaces," *Annu. Rev. Condens. Matter Phys.*, vol. 9, pp. 283–305, Mar. 2018.

[142] T. G. Anjali and M. G. Basavaraj, "Shape-anisotropic colloids at interfaces," *Langmuir*, vol. 35, pp. 3–20, 2019.

[143] P. J. Flory, "Thermodynamics of high polymer solutions," *J. Chem. Phys.*, vol. 10, no. 1, pp. 51–61, 1942.

[144] M. L. Huggins, "Some properties of solutions of long-chain compounds.," *J. of Phys. Chem.*, vol. 46, no. 1, pp. 151–158, 1942.

[145] J. W. Cahn, "On spinodal decomposition," *Acta Metall.*, vol. 9, no. 9, pp. 795–801, 1961.

[146] A. Mahapatra and P. Ghoshdastidar, "A computational study of mixed convection heat transfer from a continuously moving isothermal vertical plate to alumina–water nanofluid as in hot extrusion," *J. Manuf. Sci. Eng.*, vol. 139, no. 11, 2017.

[147] J. Buongiorno, "Convective Transport in Nanofluids," *J. of Heat Transfer*, vol. 128, pp. 240–250, 08 2005.

[148] A. Onuki, "Long-range interactions through elastic fields in phase-separating solids," *J. Phys. Soc. JPN.*, vol. 58, no. 9, pp. 3069–3072, 1989.

[149] A. Onuki and A. Furukawa, "Phase transitions of binary alloys with elastic inhomogeneity," *Phys. Rev. lett.*, vol. 86, no. 3, p. 452, 2001.

[150] J. W. Cahn, "On spinodal decomposition in cubic crystals," *Acta Metall.*, vol. 10, no. 3, pp. 179–183, 1962.

[151] L. M. Stolerman, M. Getz, S. G. L. Smith, M. Holst, and P. Rangamani, "Stability analysis of a Bulk-Surface reaction model for membrane protein clustering," *Bull. Math. Biol.*, vol. 82, p. 30, Feb. 2020.

[152] P. Gera and D. Salac, "Three-dimensional multicomponent vesicles: dynamics and influence of material properties," *Soft Matter*, vol. 14, no. 37, pp. 7690–7705, 2018.

[153] T. Baumgart, A. T. Hammond, P. Sengupta, S. T. Hess, D. A. Holowka, B. A. Baird, and W. W. Webb, "Large-scale fluid/fluid phase separation of proteins and lipids in giant plasma membrane vesicles," *Proc. Nat. Acad. Sci. USA*, vol. 104, no. 9, pp. 3165–3170, 2007.

[154] D. Saeki, T. Hamada, and K. Yoshikawa, "Domain-growth kinetics in a cell-sized liposome," *J. Phys. Soc. JPN.*, vol. 75, no. 1, pp. 013602–013602, 2006.

[155] T. Baumgart, S. T. Hess, and W. W. Webb, "Imaging coexisting fluid domains in biomembrane models coupling curvature and line tension," *Nature*, vol. 425, no. 6960, pp. 821–824, 2003.

[156] H. T. McMahon and E. Boucrot, "Membrane curvature at a glance," *J. Cell Sci.*, vol. 128, pp. 1065–1070, Mar. 2015.

[157] H. T. McMahon and J. L. Gallop, "Membrane curvature and mechanisms of dynamic cell membrane remodelling," *Nature*, vol. 438, pp. 590–596, Dec. 2005.

[158] M. M. Kozlov, F. Campelo, N. Liska, L. V. Chernomordik, S. J. Marrink, and H. T. McMahon, "Mechanisms shaping cell membranes," *Curr. Opin. Cell Biol.*, vol. 29, pp. 53–60, 2014.

[159] A. Agrawal and D. J. Steigmann, "Modeling protein-mediated morphology in biomembranes," *Biomech. Model. Mechanobiol.*, vol. 8, pp. 371–379, Nov. 2008.

[160] A. Agrawal and D. J. Steigmann, "Coexistent Fluid-Phase equilibria in biomembranes with bending elasticity," *J. Elast.*, vol. 93, pp. 63–80, May 2008.

[161] A. Callan-Jones and P. Bassereau, "Curvature-driven membrane lipid and protein distribution," *Curr. Opin. Solid State Mater. Sci.*, vol. 17, no. 4, pp. 143–150, 2013.

[162] A. Beber, C. Taveneau, M. Nania, F.-C. Tsai, A. Di Cicco, P. Bassereau, D. Lévy, J. T. Cabral, H. Isambert, S. Mangenot, and A. Bertin, "Membrane reshaping by micrometric curvature sensitive septin filaments," *Nat. Commun.*, vol. 10, p. 420, Jan. 2019.

[163] S. Aimon, A. Callan-Jones, A. Berthaud, M. Pinot, G. E. S. Toombes, and P. Bassereau, "Membrane shape modulates transmembrane protein distribution," *Dev. Cell*, vol. 28, pp. 212–218, Jan. 2014.

[164] J. C. Stachowiak, E. M. Schmid, C. J. Ryan, H. S. Ann, D. Y. Sasaki, M. B. Sherman, P. L. Geissler, D. A. Fletcher, and C. C. Hayden, "Membrane bending by protein-protein crowding," *Nat. Cell Biol.*, vol. 14, pp. 944–949, Sept. 2012.

[165] J. C. Stachowiak, C. C. Hayden, and D. Y. Sasaki, "Steric confinement of proteins on lipid membranes can drive curvature and tubulation," *Proc. Natl. Acad. Sci. USA*, vol. 107, pp. 7781–7786, Apr. 2010.

[166] Z. Shi, Z. T. Graber, T. Baumgart, H. A. Stone, and A. E. Cohen, "Cell membranes resist flow," *Cell*, vol. 175, pp. 1769–1779.e13, Dec. 2018.

[167] M. Simunovic, A. Srivastava, and G. A. Voth, "Linear aggregation of proteins on the membrane as a prelude to membrane remodeling," *Proc. Nat. Acad. Sci. USA*, vol. 110, no. 51, pp. 20396–20401, 2013.

[168] P. Sens, L. Johannes, and P. Bassereau, "Biophysical approaches to protein-induced membrane deformations in trafficking," *Curr. Opin. Cell Biol.*, vol. 20, no. 4, pp. 476–482, 2008.

[169] M. Simunovic, E. Evergren, I. Golushko, C. Prévost, H. Renard, L. Johannes, H. T. McMahon, V. Lorman, G. A. Voth, and P. Bassereau, "How curvature-generating proteins build scaffolds on membrane nanotubes," *Proc. Nat. Acad. Sci.*, vol. 113, no. 40, pp. 11226–11231, 2016.

[170] J. L. Gallop, C. C. Jao, H. M. Kent, P. J. G. Butler, P. R. Evans, R. Langen, and H. T. McMahon, "Mechanism of endophilin n-bar domain-mediated membrane curvature," *EMBO J*, vol. 25, no. 12, pp. 2898–2910, 2006.

[171] K. A. Burke, E. A. Yates, and J. Legleiter, "Biophysical insights into how surfaces, including lipid membranes, modulate protein aggregation related to neurodegeneration," *Front. Neurol.*, vol. 4, p. 17, 2013.

[172] M. Yanagisawa, M. Imai, T. Masui, S. Komura, and T. Ohta, "Growth dynamics of domains in ternary fluid vesicles," *Biophys. J.*, vol. 92, no. 1, pp. 115–125, 2007.

[173] J. E. Hassinger, G. Oster, D. G. Drubin, and P. Rangamani, "Design principles for robust vesiculation in clathrin-mediated endocytosis," *Proc. Natl. Acad. Sci. USA*, vol. 114, pp. E1118–E1127, Feb. 2017.

[174] J. Liu, M. Kaksonen, D. G. Drubin, and G. Oster, "Endocytic vesicle scission by lipid phase boundary forces," *Proc. Natl. Acad. Sci. USA*, vol. 103, pp. 10277–10282, July 2006.

[175] J. Liu, Y. Sun, D. G. Drubin, and G. F. Oster, "The mechanochemistry of endocytosis," *PLoS Biol.*, vol. 7, p. e1000204, Sept. 2009.

[176] H. Alimohamadi, R. Vasan, J. E. Hassinger, J. C. Stachowiak, and P. Rangamani, "The role of traction in membrane curvature generation," *Mol. Biol. Cell*, vol. 114, pp. 2024–2035, Aug. 2018.

[177] R. Ma and J. Berro, "Endocytosis against high turgor pressure is made easier by partial protein coating and a freely rotating base," *Biophys. J.*, 2021.

[178] P. Rangamani, A. Behzadan, and M. Holst, "Local sensitivity analysis of the "membrane shape equation" derived from the helfrich energy," *Math. Mech. Solids*, vol. 26, pp. 356–385, Mar. 2021.

[179] F. Yuan, H. Alimohamadi, B. Bakka, A. N. Trementozzi, K. J. Day, N. L. Fawzi, P. Rangamani, and J. C. Stachowiak, "Membrane bending by protein phase separation," *Proc. Natl. Acad. Sci. USA*, vol. 118, Mar. 2021.

[180] A. Mahapatra, D. Saintillan, and P. Rangamani, "Curvature-driven feedback on aggregation-diffusion of proteins in lipid bilayers," *Soft Matter*, 2021.

[181] M. Bonny, E. Fischer-Friedrich, M. Loose, P. Schwille, and K. Kruse, "Membrane binding of mine allows for a comprehensive description of min-protein pattern formation," *PLoS Comp. Biol.*, vol. 9, no. 12, p. e1003347, 2013.

[182] S. Kohyama, N. Yoshinaga, M. Yanagisawa, K. Fujiwara, and N. Doi, "Cell-sized confinement controls generation and stability of a protein wave for spatiotemporal regulation in cells," *Elife*, vol. 8, p. e44591, 2019.

[183] M. Arroyo, N. Walani, A. Torres-Sánchez, and D. Kaurin, "Onsager's variational principle in soft matter: introduction and application to the dynamics of adsorption of proteins onto fluid membranes," in *The Role of Mechanics in the Study of Lipid Bilayers*, pp. 287–332, Springer, 2018.

[184] Q. Goutaland, F. van Wijland, J.-B. Fournier, and H. Noguchi, "Binding of thermalized and active membrane curvature-inducing proteins," *arXiv preprint arXiv:2012.10312*, 2020.

[185] J. Halatek and E. Frey, "Rethinking pattern formation in reaction–diffusion systems," *Nat. Phys.*, vol. 14, no. 5, pp. 507–514, 2018.

[186] A. Mahapatra, C. Uysalel, and P. Rangamani, "The mechanics and thermodynamics of tubule formation in biological membranes," *J. Memb. Biol.*, vol. 254, no. 3, pp. 273–291, 2021.

[187] I. Derényi, F. Jülicher, and J. Prost, "Formation and interaction of membrane tubes," *Phys. Rev. Lett.*, vol. 88, no. 23, p. 238101, 2002.

[188] A. Roux, G. Cappello, J. Cartaud, J. Prost, B. Goud, and P. Bassereau, "A minimal system allowing tubulation with molecular motors pulling on giant liposomes," *Proc. Natl. Acad. Sci. U.S.A.*, vol. 99, no. 8, pp. 5394–5399, 2002.

[189] A. Frost, R. Perera, A. Roux, K. Spasov, O. Destaing, E. H. Egelman, P. De Camilli, and V. M. Unger, "Structural basis of membrane invagination by f-bar domains," *Cell*, vol. 132, no. 5, pp. 807–817, 2008.

[190] N. Walani, J. Torres, and A. Agrawal, "Anisotropic spontaneous curvatures in lipid membranes," *Phys. Rev. E*, vol. 89, no. 6, p. 062715, 2014.

[191] D. Kabaso, E. Gongadze, P. Elter, U. Van Rienen, J. Gimsa, V. Kralj-Iglic, and A. Iglic, "Attachment of rod-like (bar) proteins and membrane shape," *Mini Rev. Med. Chem.*, vol. 11, no. 4, pp. 272–282, 2011.

[192] N. Walani, J. Torres, and A. Agrawal, "Endocytic proteins drive vesicle growth via instability in high membrane tension environment," *Proceedings of the national academy of sciences*, vol. 112, no. 12, pp. E1423–E1432, 2015.

[193] S. Perutkova, V. Kralji-Iglic, M. Frank, and A. Iglic, "Mechanical stability of membrane nanotubular protrusion influenced by attachment of flexible rod-like protein," *J. Biomech.*, vol. 43, pp. 1612–1617, 2010.

[194] C. Pozrikidis, *Boundary Integral and Singularity Methods for Linearized Viscous Flow*. Cambridge University Press, 1992.